

NORTHWESTERN UNIVERSITY

Scaling Laws for Charge Transfer in Donor/Bridge/Acceptor Molecules

A DISSERTATION

SUBMITTED TO THE GRADUATE SCHOOL
IN PARTIAL FULFILLMENT OF THE REQUIREMENTS

for the degree

DOCTOR OF PHILOSOPHY

Field of Chemistry

By

Randall Howard Goldsmith

EVANSTON, IL

December 2007

ABSTRACT

Scaling Laws for Charge Transfer in Donor/Bridge/Acceptor Molecules

Randall Howard Goldsmith

This thesis attempts a combined theoretical/experimental investigation of two fundamental scaling laws in charge transfer reactions: how the rate of those reactions varies as a function of distance between an electron donor and an electron acceptor and how the rate varies as a function of the number of distinct pathways between that donor and acceptor. At all points, we use photoinduced intramolecular charge transfer as a foundation on which to build our theories and as a test bed in which to evaluate them.

We add to the existing body of work on the study of the distance dependence of charge transfer by advancing a new modular system, fluorene oligomers, that possesses oxidation potentials that remains relatively static as a function of length, and show very simple Arrhenius like temperature dependence, suggesting the lack of complex conformational dynamics. Both of these properties allow the weak distance dependence of charge separation to be very well described by simple kinetic analysis, while charge recombination rates still show some intriguing and (as of yet) unaccounted for complexity.

We then describe a theoretical framework that addresses the issue of coherent summation of electronic paths over multiple distinct pathways in the presence of decoherence processes. Specific predictions are made regarding the contribution of interference phenomena and suggest that caution must be used when evaluating the contribution of interference at finite temperature.

Individual Liouville space pathways are probed to get mechanistic information about which coherences survive. Constructive and destructive interference processes are discussed.

Finally, we attempt to probe experimentally the marginal effect of adding additional spatial pathways. Specifically, we synthesize a novel family of benzo-annulated bicyclo[2.2.2]octane bridge groups designed to compare, in an equivalent geometry, the contribution of additional π -pathways. However, by showing charge transfer rates that are essentially independent of the number of additional fused rings, the system reveals subtle features of how orbital alignment controls the electronic coupling. Natural Bond Orbital analysis is applied and suggests strong destructive interference effects. Unexpected temperature dependences are observed but are well accounted for by molecular dynamics simulations.

ACKNOWLEDGEMENTS

Mike and Mark, I have been spending 5 years asking myself if, I had it all to do over again, would I? Would I come to Northwestern? Would I become a joint student with you two gentlemen? I can now say the answer is yes, and that is the best measure I can give of how much I valued this experience. Mike, we have driven pretty hard over the past few years. You have instilled in me the constant need to ask myself “can I do better?” and that lack of complacency will serve me well. I know it took me a little while to show up consistently at our weekly meetings, but I really enjoyed those problem solving sessions and learned a lot. And thank you for all the great conversations from all the way across the conference room. Mark, you still make me feel like a million bucks when we talk. The decision to wake up at 4AM in Wisconsin and take a long drive full of science and life and fishing was one of the better decisions I have made. You have asked me great questions. Mike and Mark, thank you for showing the confidence in me to put me on a new and exciting and perhaps a little bit crazy project. Thanks for continuing to show confidence in me when it struggled in the beginning.

Thank you so much, Franz and Tamar, my committee members. I have called on both of you a number of times, and you have both made this process much easier and more enjoyable.

Any list of acknowledgements of my peers needs to begin with Eric Greyson. You taught me a ton, you played the most active role in keeping me sane, and we still have some punch to drink. Zach Dance and Brooks Jones were who I went to when I needed a pick-me-up, whether it was a good scientific idea or good laugh. Xiyou Li taught me how to do synthetic chemistry and Mas Iimura taught me how to do advanced synthetic chemistry, and I am very grateful. Josh Vura-Weis was the best office-mate I could have asked for and was a willing collaborator in

much scientific mischief. Thanks to Boiko Cohen for his instruction on femtosecond transient absorption. Orlando DeLeon provided me with a shot of enthusiasm at the end when I needed it most.

I also benefited greatly from my interaction with the older generation of Waz group members, Mike Ahrens, Jovan Giaimo, Louise Sinks, Mike Fuller, Mike Tauber and Emily Weiss. Rick Kelley, Erin Chernick, Qixi Mi and Emilie Giacobbe were always available for good scientific discussion and advice. Thank you, Charusheela Ramanan and Daniel Finkelstein-Shapiro for help at the end. Thank you Amy Vega, Thea Wilson, Joseph Bullock, Annie Ricks, Sara Mickley, Michael Colvin and Vickie Gunderson.

Upstairs, I could always go for some advice, and that advice often came from Yuri Berlin, Gemma Solomon or Chad Risko. Vladimiro Mujica challenged me to be a better theoretician. I have learned so much from Abraham Nitzan and his influence on my thinking is very evident in the introduction.

Thanks to Tyler McQuade, Hercules Neves, and Frank Houlihan for being great former advisers.

It is important to have good friends who encourage you and keep you from taking yourself too seriously, but mostly encourage you. Thank you Alvaro Masias, Eliana Stein, Brett Lee, George Barton, and Alia Black. Thank you Khalid Salaita, Brandon Rodriguez, Julia Chamberlain and Ben Staehlen

Thanks to my parents for being great parents.

Dedication

thanks, Zadie Joe.

Table of Contents

ABSTRACT	3
ACKNOWLEDGEMENTS	5
Dedication	7
Table of Contents	8
List of Figures	12
List of Tables	15
List of Tables	15
Chapter 1 Introduction	16
<i>1.1 Motivation</i>	<i>17</i>
<i>1.2 Approach</i>	<i>18</i>
<i>1.3 Distance Dependence</i>	<i>23</i>
<i>1.4 Multiple Spatial Pathways</i>	<i>27</i>
<i>1.5 Outline</i>	<i>29</i>
Chapter 2 Wire-like Charge Transport at Near Constant Bridge Energy through Fluorene Oligomers	31
<i>2.1 Introduction</i>	<i>32</i>
<i>2.2 Results and Discussion</i>	<i>34</i>
2.2.1 Molecular Geometries and Energy Levels.....	34
2.2.2 Charge Separation and Recombination Dynamics	40
2.2.3 Magnetic Field Effects: Superexchange vs. Hopping.....	47
<i>2.3 Conclusion</i>	<i>50</i>
<i>2.4 Synthesis</i>	<i>51</i>
Chapter 3 Temperature Dependence of Charge Separation Through Fluorene Oligomers: An Ideal System for Studying Charge Transfer Mechanisms	64

	9
<i>3.1 Introduction</i>	65
<i>3.2 Results and Discussion</i>	68
3.2.1 Variable Temperature Transient Absorption	68
3.2.2 Aggregation.....	69
3.2.3 Rate Analysis	72
<i>3.3 Conclusion</i>	74
Chapter 4 Scaling Laws for Charge Transfer in Multiply Bridged Donor/Acceptor Molecules in a Dissipative Environment	76
<i>4.1 Introduction</i>	77
<i>4.2 Method</i>	78
<i>4.3 Results</i>	83
4.3.1 Rate Ratios	83
4.3.2 Initial Value Problem.....	86
<i>4.4 Discussion</i>	87
4.4.1 Participation Ratios	87
4.4.2 Percent Maximal Coherence	88
<i>4.5 Conclusion</i>	91
<i>4.6 Equations of Motion</i>	92
Chapter 5 Electron Transfer in Multiply-Bridged Donor-Acceptor Molecules: Dephasing and Quantum Coherence	104
<i>5.1 Introduction</i>	105
<i>5.2 Results and Discussion</i>	107
5.2.1 System, Dynamics, and Steady State.....	107
5.2.2 Destructive Interference and Dephasing.....	109
5.2.3 Benzene and Davidenne.....	111
<i>5.3 Conclusion</i>	114
<i>5.4 Equations of Motion</i>	114

	10
Chapter 6 Never Underestimate Your σ-System: Charge Transfer Through Benzo-Annulated Bicyclo[2.2.2]octanes and Triptycene.....	118
6.1 Introduction.....	119
6.2 Results.....	121
6.2.1 Molecular Design.....	121
6.2.2 Energy Levels.....	127
6.2.3 Spectroscopy.....	128
6.3 Discussion.....	132
6.3.1 Contribution of the Bridge π -System.....	133
6.3.2 Contribution of the Bridge σ -System.....	135
6.3.3 MTHF data at 300K.....	140
6.3.4 MTHF data at 80 K.....	141
6.4 Conclusion.....	144
6.5 Synthesis.....	145
6.6 Sample Calculations.....	168
6.6.1 Reorganization and Activation Energies.....	168
6.6.2 Overlaps.....	169
Chapter 7 Conclusion.....	172
Chapter 8 Experimental and Computational Methods.....	175
8.1 Purification and Characterization.....	176
8.2 Steady State Absorption Spectroscopy.....	176
8.3 Cyclic Voltammetry.....	177
8.4 Femtosecond Transient Absorption Spectroscopy.....	177
8.5 Nanosecond Transient Absorption Spectroscopy and Magnetic Field Effects.....	179
8.6 Time Resolved Fluorescence.....	180
8.7 Computation.....	181

	11
Appendix A Fast Redox Switchable Diffraction Gratings	200
Curriculum Vitae	208

List of Figures

Figure 1 Structures of D/A derivatives of fluorene oligomers.....	35
Figure 2 HOMO's of FL_n^{+} for 2-4.....	37
Figure 3 Steady-state absorption spectra of PTZ- FL_n -PDI in toluene.....	40
Figure 4 Transient absorption spectra of 2 following a 530 nm, 130 fs laser excitation pulse. ...	41
Figure 5 (A) Plot of $\log k_{CS}$ vs. distance, and (B) plot of k_{CS} vs. $1/\text{distance}$ for photoinduced charge separation in PTZ- FL_n -PDI in toluene.....	44
Figure 6 Plot of rate constant vs. distance for charge recombination of $PTZ^{+\bullet}$ - FL_n - PDI^{\bullet} in toluene.	45
Figure 7 Plots of the relative yield of 3PDI vs. magnetic field strength for the indicated molecules in toluene.	48
Figure 8 Logarithmic plot of the spin-spin exchange interaction, $2J$, vs. r_{DA}	50
Figure 9 Structure of Fluorene D-B-A molecules.....	67
Figure 10 Transient absorption spectra of 1 in toluene with 532 nm excitation at A) 300 K and B) 210 K	68
Figure 11 Semilogarithmic plot of $k_{CT}T^{1/2}$ vs $1/T$ for 1-3 and linear fits	70
Figure 12 Steady-state UV-vis absorption of 2 in toluene over a range of temperatures showing evidence of exciton coupling.....	71
Figure 13 Connectivities of multiple spatial pathway Donor-Bridge-Acceptor systems. The red (bridge) and blue (node) sites are energetically degenerate. The numbers denote the sites.	79
Figure 14 Rate ratios for the 2 (blue line) and 3 (red line) path systems, absolute rate for the 1 path system (black line) calculated with the enforced SS, and comparison with that rate calculated as an IVP (black circle). The above values were calculated for increasing dephasing on the red and blue sights (A), just the blue sites (B), and just the red sites (C).....	84
Figure 15 Participation Ratios with different dephasing schemes.....	88
Figure 16 Plots of the Percent Maximal Coherence (PMC) of each position of the density matrix at increasing dephasing strength for three dephasing schemes: dephasing on the red and	

	13
blue sites (A), the blue sites (B), and the red sites (C). The numbers on the axes denote the different sites (from Figure 13).....	89
Figure 17 (A) Simple D-B-A connectivity, (B) Connectivity of a “Joachim” type molecular interferometer. B_n levels are at an energy ω above the degenerate D and A levels	106
Figure 18 Recovery of transport with increasing pure dephasing rate in a system with connectivity defined by Figure 1(B). $V_1 = 300 \text{ cm}^{-1}$ $\omega = 500 \text{ cm}^{-1}$ $\kappa = 20 \text{ cm}^{-1}$	109
Figure 19 (A) “Benzene” type system connectivity, (B) Coalescence of ortho, meta, and para conductance with increasing pure dephasing rate. $V = 300 \text{ cm}^{-1}$ $\omega = 0 \text{ cm}^{-1}$ $\kappa = 20 \text{ cm}^{-1}$, (C) A davidene molecule.....	112
Figure 20 Structures of Donor-Bridge-Acceptor molecules with benzo-annulated BCO bridges	121
Figure 21 Synthesis of 1 a) KOC_2H_5 , EtOH, 55% b) 1. NaH, DME 2. $\text{C}_2\text{H}_4\text{Br}_2$, 71% c) $\text{HS}(\text{CH}_2)_3\text{SH}$, $\text{BF}_3 \cdot \text{Et}_2\text{O}$, CHCl_3 , 80% d) Raney Ni, EtOH, 98% e) LiAlH_4 , Et_2O , 89% f) oxalyl chloride, DMSO, DCM, quant. g) CBr_4 , PPh_3 , Zn, DCM, hexanes, 53% h) <i>n</i> -BuLi, THF, 76% i) 1. iodophenylpyrrolidine, piperidine, CuI, $\text{Pd}(\text{PPh}_3)_4$ 2. bromocyanoanthracene, TEA, CuI, $\text{Pd}(\text{PPh}_3)_2\text{Cl}_2$, 9%.....	122
Figure 22 Synthesis of 4 a) TIPS acetylene, DEA, CuI, $\text{Pd}(\text{PPh}_3)_2\text{Cl}_2$, 95% b) isoamyl nitrite, anthranilic acid, dioxane, 43% c) TBAF, THF, 73% d) 1. bromocyanoanthracene, TEA, CuI, $\text{Pd}(\text{PPh}_3)_2\text{Cl}_2$ 2. iodophenylpyrrolidine, piperidine, CuI, $\text{Pd}(\text{PPh}_3)_4$, 15%.....	123
Figure 23 Synthesis of 2 a) 1. SOCl_2 , Br_2 , MeOH, hv 2. pyridine, 22% b) DIBALH, THF, 42% c) TBDMSCl, DMF, 66% d) <i>p</i> -benzoquinone, toluene, 83% e) NaBH_4 , $\text{CeCl}_3 \cdot 7\text{H}_2\text{O}$, MeOH, DCM, quant. f) POCl_3 , pyridine, 68% g) H_2 , Pd/C, EtOH, EtOAc, 90% h) TBAF, THF, 95% i) PCC, DCM, 73% j) dimethyl-1-diazo-2-oxopropylphosphonate, K_2CO_3 , MeOH, 87% k) 1. bromocyanoanthracene, TEA, CuI, $\text{Pd}(\text{PPh}_3)_2\text{Cl}_2$ 2. iodophenylpyrrolidine, piperidine, CuI, $\text{Pd}(\text{PPh}_3)_4$, 5%.....	123
Figure 24 Synthesis of 3 a) paraformaldehyde, $\text{HCl}_{(\text{g})}$, dioxane, 50% b) NaOAc, HOAc, 78% c) toluene, C_2H_4 (2400 psi) d) EtOH, KOH, 93% e) PCC, DCM, 56% f) dimethyl-1-diazo-2-oxopropylphosphonate, K_2CO_3 , MeOH, 92% g) 1. bromocyanoanthracene, TEA, CuI, $\text{Pd}(\text{PPh}_3)_2\text{Cl}_2$ 2. iodophenylpyrrolidine, piperidine, CuI, $\text{Pd}(\text{PPh}_3)_4$, 7%.....	124
Figure 25 ^1H NMR spectra of the aromatic regions of 1-4 at 300 K in CDCl_3 . Red circles denote peaks from CA, blue triangles denote peaks from PP, and green squares denote peaks from the bridge. Notice the downshifting circles and squares.	126
Figure 26 Structures of model compounds with CA and PP	127
Figure 27 Steady-state UV-vis spectra of 1-5 and 7 in toluene at 295 K.	129
Figure 28 Transient absorption spectra of 2 at 295 K in toluene.....	130

	14
Figure 29 Transient absorption spectra of 1-4 at 295 K in a) toluene at 1029 ps and b) in MTHF at 239 ps.....	130
Figure 30 Transient absorption kinetics of 1-4 measured in a) toluene at 643 nm at 295 K b) toluene at 655 nm at 295 K c) MTHF at 613 nm at 295 K d) MTHF at 80K at 716 nm at 80 K	131
Figure 31 Relevant orbitals for overlap with the bridge σ and π systems. S refers to spatial overlap and F (mH) refers to the appropriate Fock matrix element	132
Figure 32 Application of Walton and Adcock's orbital overlap model ²⁰⁵	134
Figure 33 Steady-state UV-vis of 1 at a variety of temperatures in MTHF	142
Figure 34 Charge transfer trajectories for a model of 1 at different effective temperatures. a) a molecular dynamics snapshot with only zero point energy (0K) in each of the modes and the corresponding trajectory b) showing charge shift. c) a molecular dynamics snapshot after equilibration at 300K with d) no charge shift in the trajectory	143
Figure 35 a) Optical microscope image of IAIME with deposited thiophene. B) AFM image of the same film.	202
Figure 36 a) Diffraction pattern of the "off" or neutral state. b) Diffraction pattern of the "on" or oxidized state. The spot corresponding to the undiffracted beam was removed.....	204

List of Tables

Table 1	Summary of redox properties of the indicated species in the indicated solvents vs. Fc/Fc ⁺ . †Irreversible faradaic processes are reported as <i>E_p</i> values. The potentials for the oxidation of PTZ ⁷⁶ and the reduction of PDI in dichloromethane ⁷⁷ have been measured previously and are reversible.....	38
Table 2	Summary of free energies of formation of radical ion pairs calculated as described in the text as well as rate constants for charge separation, <i>k_{CS}</i> , and recombination, <i>k_{CR}</i> . Values of free energies are accurate to approximately ±0.1 eV. All values of <i>k_{CS}</i> were measured via femtosecond transient absorption (FS-TA) and time resolved fluorescence (TRF). All values of <i>k_{CR}</i> were measured by nanosecond transient absorption, with 1-3 measured from PDI [•] decay at 720 nm and 4 measured from ^{3*} PDI formation at 455 nm.....	39
Table 3	Relevant electron transfer parameters.....	128
Table 4	Electron transfer time constants in benzo-annulated BCO's.....	131
Table 5	Parameters from NBO analysis. Energies given in mH. ε _i , F _(i,j) V _{eff} (i,j,...) refer to the numbered orbitals below. V _{eff} (i,j,...) are calculated using Equation 6.1.	137

Chapter 1 Introduction

1.1 Motivation

If charge transfer truly is the simplest and most fundamental chemical reaction, as it is frequently described, then why, after decades of research and the cumulative careers of hundreds of scientists, are we still so furiously studying it?

The first part of the answer comes from its applicability. Even if one preemptively removes from the discussion the role of charge transfer in, for example, organic mechanism elucidation (arrow pushing) or interfacial charge transport (electrochemistry), and limits oneself to discussion of photo-induced charge transfer in Electron Donor (D)/Electron Acceptor (A) systems, the subject of this thesis, then one is still faced with abundant motivation for this particular scientific pursuit. Charge transfer comprises one of the basic microscopic processes in the operation of a photovoltaic device.¹ It is the link between the exciton formed when light first interacts with the photoactive material and the harvesting of charge that makes for a practical device. The construction of cheap and mass-producible photovoltaics has been identified as a key research objective.² Organic photovoltaics, by virtue of their optoelectronic tailorability and potential to be conveniently fabricated over the large areas requisite for real application are a prime candidate to satisfy this goal. These materials contain Electron Donors and Electron Acceptors as their core functional groups.

Perhaps only marginally less in social relevance, is the use of these same functional Donors and Acceptors as elements in molecular computing devices.³ Molecules are the smallest scale of matter where a suitable amount of structural and electronic manipulation can be applied and so represent the logical frontier for smaller electronic devices. The same in-depth understanding that would allow one to design an efficient organic photovoltaic (for example,

accelerating a forward charge transfer reaction while retarding the recombination) can be applied to design a molecular transistor or wire. Indeed, the construction of molecular wires will comprise a significant fraction of this thesis.

Finally, the applicability of the study of charge transfer is apparent in any attempt to understand the chemical basis of photosynthesis.⁴ Whether in the shifting of charge from light harvesting complex to the initial quinone electron shuttle in the “light reactions,” or in the interaction between this complex network of electron shuttles and the ultimate recipients of the charge that comprise the “dark reactions,” charge transfer is present at every step. Some of the novel observations made by studying biological electron transfer, such as extremely efficient electron transfer over large distances⁵ or the possible contribution of multiple distinct spatial pathways,⁶ are central motivators of this thesis.

These interesting observations naturally lead to the second reason why people continue to study charge transfer in D/A systems: very simply, we are still discovering new things and trying to understand them.

1.2 Approach

When faced with an object of study that seems in practicality neither “simple” nor “fundamental,” one needs to choose one’s battles carefully. One would like to be able to reduce the problem to a finite number of specific parameters. Then, one would like to modulate one specific parameter and see its effect on some dependent variable of interest, in this case, the charge transfer rate, k_{CT} . In this method, one can see how k_{CT} changes with that specific parameter and so determine the *scaling law* associated with that parameter, the independent variable.

Charge transfer has been parametrized in terms of a number of different variables with several different scaling laws being elucidated. The most famous is the dependence of k_{ET} on the free energy of reaction, ΔG , and the prediction⁷ and later confirmation^{8,9} of the existence of the Marcus inverted region, where increase in the magnitude of ΔG results in a decrease in k_{ET} . Scaling laws have been investigated for many other parameters including solvent polarity,⁸ solvent viscosity,¹⁰ temperature,¹¹ bridge redox potential,¹² and external magnetic field,¹³ among others. Obviously, changing one parameter frequently influences other parameters as well. Part of our challenge is to minimize these collateral changes as much as possible.

As foreshadowed by the previous section, the two scaling laws we will investigate are the dependence of k_{ET} on the distance between the D and A and on the number of distinct spatial pathways between the D and A.

At this point, the delving into charge transfer theory would typically begin with Equation 1.1,

$$k_{\text{CT}} = \frac{2\pi}{\hbar} V_{\text{RP}}^2 (\text{DWFC}) \quad (1.1)$$

where V_{RP} is the matrix element coupling the reactant and product electronic wave functions and DWFC, the density of states weighted Franck-Condon factor, describes the nuclear overlap. Our ability to make this separation into two terms stems from the legitimacy of the Born-Oppenheimer approximation in usual cases. This equation constitutes an excellent starting off point to highlight the DWFC term that is responsible for the Marcus inverted region as well as emphasizing the role of the matrix element coupling the excited and charge transferred states (for charge transfer in the non-adiabatic limit). However, rather than use this equation as a starting

off point, we will use it as an intermediate result, and instead truly begin from a simple two state system. Being able to connect this two site system to Equation 1.1 is important because we will be using these simple site (toy) models throughout this document and need to maintain a link between it and a real system.

The states in our system will be labeled D (Donor) and A (Acceptor). We use these labels with full knowledge of the consequences those names imply. We want our states to reflect the reality of our system and so choose a convenient basis to express them, a site basis that is easily related to our physical system. We also want the D in our two site system to be a near identical copy of the isolated D. This caveat identifies the charge transfer process under study as diabatic (or non-adiabatic) charge transfer because the interaction with the A site is minimal enough to leave the D in the D-A pair relatively unchanged from the isolated D.

D and A are also chosen to be isoenergetic. This degeneracy is implemented to reflect the system as it would appear at the crossing point of the potential energy curves. In this way, we can write a purely electronic Hamiltonian, Equation 1.2, and not have to worry about nuclear overlap because at this part of the curve, adequate nuclear overlap is already achieved.

$$H = \begin{pmatrix} 0 & V \\ V & 0 \end{pmatrix} \quad (1.2)$$

As an initial condition, we can imagine all population on the D site. This can be indicative of a mixing that is only activated after t_0 , or in our case, indicative of a photoexcitation that instantaneously produces population on D at t_0 . When one applies the time-dependent Schrödinger equation, one gets equations of motion, Equations 1.3, that yield solutions with

oscillating populations on the D and A sites. C_i is the time dependent wave function coefficient in the Schrödinger picture.

$$\begin{aligned}\frac{dC_D}{dt} &= -\frac{i}{\hbar}VC_A \\ \frac{dC_A}{dt} &= -\frac{i}{\hbar}VC_D\end{aligned}\tag{1.3}$$

How can this situation adequately describe charge transfer which (with suitable separation of time scales) is irreversible?

Following the approach of Jortner¹⁴ as laid out by Nitzan,¹⁵ to enforce irreversibility, one must replace the discrete level with a quasicontinuum of levels .

$$\begin{aligned}\frac{dC_D}{dt} &= -\frac{i}{\hbar}\sum_l^N V_l C_{A,l} \\ \frac{dC_{A,l}}{dt} &= -\frac{i}{\hbar}V_l C_D\end{aligned}\tag{1.4}$$

This summation reflects that the A electronic wavefunction is broadened by an array of closely spaced vibronic states. In this case, the origin of these vibronic states is low frequency vibrational modes from solvent motions or intramolecular modes. The result is a transition from a simple two state system to an N+1 site system, where N of those levels form a continuum centered around the A site. That continuum can be described by a density of states, $\rho_{\text{DOS}}(E)$ and couples to the D site with matrix element $V(E)$, where E is the site energy.

Solving Equation 1.4 in the limit where $\rho_{\text{DOS}}(E)$ is dense, extends from $-\infty$ to $+\infty$ and $V(E)$ and $\rho_{\text{DOS}}(E)$ are independent of E, we get a very different solution to that from Equation 1.3,

$$|C_D(t)|^2 = e^{-\kappa t/\hbar} = e^{-k_{CT}t} \quad (1.5)$$

where $\kappa = 2\pi V^2 \rho_{DOS}$

We have gone from a completely oscillatory solution to one where we get irreversible transfer away from the D site! This transfer has a rate constant,

$$k_{CT} = \frac{2\pi}{\hbar} V^2 \rho_{DOS} \quad (1.6)$$

Why does the charge carrier not simply return to the Donor after some appropriate phase oscillation? The infinitely dense continuum has provided significant phase erosion (dephasing) such that a return to the Donor state, essentially an echo, is impossible.¹⁴

It is also important to note that while the tidy monoexponential form of Equation 1.5 is a consequence of the rather simple $\rho_{DOS}(E)$ we chose, the irreversibility is general to a continuum of arbitrarily shaped $\rho_{DOS}(E)$ and $V(E)$.¹⁵ We can now return to Equation 1.1 and compare it with our recently derived Equation 1.6. The presence of the continuum make Equations 1.1 and 1.6 “Golden Rule” type expressions. The ρ_{DOS} has been absorbed into an effective V term. The additional (DWFC) term reflects the fact that our D and A states are not necessarily energetically degenerate but are more accurately described by potential energy manifolds that describe many energies and nuclear configurations around some equilibrium configuration and energy. Replacing (DWFC), we get the Marcus equation in the non-adiabatic classical limit,

$$k_{CT} = \frac{2\pi}{\hbar} V_{RP}^2 \sqrt{\frac{1}{4\pi\lambda k_B T}} e^{-\frac{(\Delta G + \lambda)^2}{4\lambda k_B T}} \quad (1.7)$$

The additional $T^{-1/2}$ term describes dynamics in the vicinity of the potential energy curve crossing, as required by Landau-Zener transition state theory.¹⁵

We were able to build this expression by taking 2 sites, D and A, broadening one site to a continuum of levels to get a “Golden Rule” type expression, and then explicitly including the DWFC term.

1.3 Distance Dependence

How does V_{RP} (V hereafter) scale as the D and A are moved farther apart? And, more specifically, why are “anomalous distance dependences” of charge transfer so anomalous?

If two orbitals overlap in space, those formerly separated orbitals are no longer completely accurate eigenvalues of the system Hamiltonian, although, as we are in the diabatic regime, this mixing should be relatively small. The mixing between the two orbitals (the off-diagonal element when expressed in a simple Hückel picture) is proportional to the extent of spatial overlap

$$V \propto \int \psi_1 \psi_2^* d\tau \quad (1.8)$$

where ψ_i are the orbital wavefunctions and $d\tau$ is the differential volume element. Equation 1.8 is an approximation of the true V .

$$V = \langle \psi_1 | H | \psi_2 \rangle \quad (1.9)$$

However, because Equation 1.9 is more difficult to calculate, Equation 1.8, a Mulliken’s Magic Formula type expression,¹⁶ can be used as a crude approximation.

Because the radial functions of orbitals decay exponentially with distance (for $r > r_0$, a distance of approximately 2\AA), the overlap, and thus the mixing also decays exponentially with distance, as shown in Equation 1.10

$$k_{CT} \propto V^2 \propto e^{-\beta r} \quad (1.10)$$

where β is a parameter that describes the exponential decay.

When direct overlap is required, the degree of exponential decay through a vacuum is actually quite severe. Calculations on ethene groups separated by increasing distances were used to estimate the electronic coupling from one half the orbital splitting energy. A β value of $2.8\text{-}3\text{\AA}^{-1}$ was determined.¹⁷ Such a precipitous decline in electronic coupling would seem to preclude long range electron transfer.

Luckily, we do not have to rely on the conductive prowess of a vacuum! Any intervening electronic states can help retard this decline. These intervening states do not necessarily need to ever be occupied by the charge carrier either. These virtual states are sufficient to soften the exponential distance dependence.

Qualitatively, this indirect mixing or *superexchange* can be thought to act as a “transitive” property among orbitals. For example, if the Donor mixes with some bridge state and the bridge state mixes with the Acceptor, then the Donor and Acceptor mix via the B state though their direct overlap may be vanishingly small.

Quantitatively, superexchange was treated by Kramers and Anderson when describing exchange between unpaired spins via intervening paired spins.^{18,19} This concept was adapted by

McConnell in describing charge shift in aromatic radicals.²⁰ He decomposed the effective coupling, V_{eff} in terms of a sequence of microscopic couplings,

$$V_{eff} = \frac{V_{D1}V_{NA}}{E_1 - E_{D/A}} \prod_{i=1}^N \frac{V_{i,i+1}}{E_{i+1} - E_{D/A}} \quad (1.11)$$

where V_{ij} are matrix elements between the D, A, and intervening bridges and E_i is the energy of a particular site. Because this result is derived perturbatively, it requires the ratio $V/\Delta E$ to be relatively small. Alternatively, this result is only valid in the so-called deep tunneling regime, where only negligible population resides on the intervening sites.

What is the nature of these intervening sites?

In biological electron transfer, these states may involve non-protein prosthetic groups, such as hemes or quinones, embedded in the protein or membrane.⁵ In our discussion of photoinduced charge transfer between Donors and Acceptors, these states will typically belong to covalently bound bridges that semi-rigidly link the Donor and Acceptor.

The parameter β has been measured for many different chemically distinct bridges and summarized in a number of places.²¹ The β value of 2.8-3.0 \AA^{-1} softens considerably to 0.8-1.4 \AA^{-1} for proteins and 0.75-0.98 \AA^{-1} for saturated hydrocarbon bridges. By adding degrees of unsaturation the β parameter can be brought even lower to 0.5 \AA^{-1} , while maintaining complete conjugation can lead to values of 0.4 \AA^{-1} and lower. The decay parameters of these last two classes can be rationalized in terms of the existence of π -systems on the bridge resulting in a smaller McConnell denominator because of better resonance with the D and A π -system.

While this β parameter would seem to adequately describe how k_{CR} scales with distance, a number of reports describe “anomalously” low values for β . Such values of 0.2 \AA^{-1} and lower

appear to require the bridge to be nearly energetically degenerate with the D and A.²² Such a regime is poorly described by the McConnell expression and as a consequence, equation 1.10. A recent report has even endeavored to define a cutoff value for a legitimate β value, which they estimated to be between 0.2 and 0.3 Å⁻¹.²³

If these scaling laws are not adequately described by superexchange, then what is the alternative?

As the energy gap between the D and B is lowered (though not eliminated), non-negligible probability density for the charge carrier exists on the B. As a consequence, appreciable vibronic coupling effects can occur between the charge carrier and B centered nuclear motions.²⁴ Said another way, the lower energy barrier between the D and A as a result of the lowered B state will allow realistic fluctuations in B energy to influence the charge carrier.²⁵ If the energy gap between the D and B vanishes and charge transfer to the A becomes exothermic, these fluctuations, stemming from vibronic coupling to a molecular vibration or to a solvent with a dense vibrational spectrum, will result in a broadening of Bridge vibronic levels into a continuum, much in the same way a continuum was formed earlier at the terminal Acceptor.^{14, 24} As before, this broadening results in irreversible charge transfer: the charge carrier is actually *occupying* the Bridge.

If multiple B sites are present, the sequence can continue with the charge carrier moving from B to B' until ultimate capture at the A's vibronic manifold. In this way the charge carrier can be seen to *hop* from B to B'. This hopping transfer is not described by an exponential distance scaling law, but rather by a much softer 1/N law, where N is the number of bridges.²⁶ This ohmic distance dependence is essentially a macroscopic scaling law. Hopping transport is

also commonly referred to as incoherent or incoherent hopping transport. The additional “incoherent” term emphasizes the effect of the B vibronic continuum. In superexchange, a coherent transfer, phase relationships at all sites are maintained until dephasing and capture at the Acceptor. In incoherent hopping, phase relationships are destroyed at each B site resulting in occupation.

The first part of the work in this thesis is to elucidate the scaling law of k_{CT} with B length in the vicinity of the transition between the superexchange mechanism and incoherent hopping.

1.4 Multiple Spatial Pathways

While much effort has been spent on understanding the scaling law of k_{CT} with distance, relatively little effort has been devoted to looking at how k_{CT} scales with multiple spatial pathways.

On the surface, it would seem that taking multiple spatial pathways into account would be central to explaining chemical phenomena: afterall, bp-xylene is a ring, with two pathways connecting two substituents oriented *para* to each other. However, it is not obvious if viewing two halves of a xylene molecule as two individual pathways is a realistic approach.

Most investigations have been theoretical in nature, due to the lack of availability of suitable test systems. Most of these investigations have looked at the size scale described above, examining multiple intramolecular pathways. Some workers have used simple site models²⁷⁻³² while others^{17, 33-35} have attempted to more closely capture the “chemical” nature of the systems under study by examining pathways between Natural Bond Orbitals (NBO’s).³⁶ The simple additivity, or constructive interference between paths, was even suggested as being directly responsible for moderate β values in poly(alkane) systems.¹⁷ More recently, several theoretical

investigations have highlighted the possible contributions of multiple pathways in significantly larger systems: charge transfer in proteins.^{6, 37-39}

The notions of constructive and destructive interferences in multiple pathways are intimately tied with the “sign” of the electronic coupling, V .^{35, 40, 41} At a phenomenological level, V controls the ordering of symmetric and antisymmetric combinations of orbitals, with a positive coupling describing the situation where the symmetric combination is energetically above an antisymmetric combination, and a negative coupling describes the opposite situation where the antisymmetric combination is higher. Two directly overlapping orbitals always have a negative coupling, consistent with our expectation that an antisymmetric (frequently an antibonding orbital) should be higher in energy. However, when multiple orbitals are connected in a sequential manner,⁴⁰ the symmetry of the orbitals involved may impart an “effectively” positive or negative coupling between a particular pair of orbitals. At a microscopic level, the sign describes the phase of the wavefunction at a particular orbital or site with respect to another orbital or site, and while this phase has no consequences in cases where these sites are isolated, the phase may quite important in their interaction. Importantly, this sign is not a hidden quantum mechanical quantity, but is sometimes experimentally measurable using photoelectron spectroscopy.^{42, 43} However, experimental confirmation of interference between multiple molecular pathways and its effect on charge transfer is still difficult to find, although several attempts have been made.^{44, 45}

Part of the issue in confirming the additivity of multiple pathways and observing interference may be in our assumption regarding the legitimacy of simple additivity. Interference between two entities requires phase coherence between those entities. If that phase coherence is poorly defined or fluctuating, then this additivity may be invalid. We saw the effect

of “phase erosion” earlier, which results in the irreversibility that comes with coupling to a continuum¹⁴ and is required for hopping transport. Electronic decoherence, or dephasing, has been studied theoretically⁴⁶⁻⁵¹ and experimentally⁵²⁻⁵⁴ by many workers, and must be taken into consideration when describing the effect of multiple pathways. Dephasing certainly must be taken into consideration when describing a scaling law for multiple spatial pathways.

1.5 Outline

In this thesis we will investigate scaling laws for distance and multiple pathways in charge transfer in D-B-A molecules. We will use the approach described above, where we attempt to keep constant as many individual system variables as possible and only change the variable of interest.

In Chapter 2 we investigate the distance dependence of charge transfer using fluorene oligomers as our bridge group. Fluorene oligomers have the unique property among conjugated materials of an oxidation potential that is relatively constant as a function of the number of repeat units. The shifting of bridge energy levels as the number of repeat units is increased was seen to dominate in previous studies.^{55, 56} Fluorene oligomers will be used to avoid this complication, and more truly vary the distance and *only* the distance.

In Chapter 3 we continue our investigation of charge transfer in fluorene oligomers by evaluating the charge separation rate as a function of temperature. This approach will allow us to determine some of the parameters of Equation 1.7 and continue to understand how charge transfer scales with distance.

In Chapter 4 we switch our investigation to the issue of the scaling of multiple spatial pathways. We undertake a theoretical investigation where dephasing is included

phenomenologically to evaluate the additivity of multiple degenerate spatial pathways. As suggested above, the existence of constructive interference will be seen to be very sensitive to the rate of electronic dephasing.

In Chapter 5 we extend our theoretical investigation and look at how dephasing affects destructive interference. Simple trends in chemical reactivity are also recast as interference effects and a system is suggested for experimentally observing destructive interference in charge transfer.

In Chapter 6 we attempt to experimentally observe constructive interference in charge transfer. Keeping with our approach of trying to vary only a single variable, we design a system that allows a fixed geometry to be maintained while appending additional spatial pathways, phenyl rings, to fixed scaffold, bicyclo[2.2.2]octane. However, an unexpected trend is observed, which implies an active role of bicyclo[2.2.2]octane scaffold.

In Chapter 7 we offer a brief set of conclusions

In Chapter 8 we describe the experimental techniques that were employed for the work in this thesis.

In Appendix A we describe a proof-of-concept model of a “real world” application of some of the principles we have described above. The delocalized nature of charge carriers in a hole transporting material is used to create a relatively large change in the index of refraction, which is used to create a variable periodicity diffraction grating.

Chapter 2 Wire-like Charge Transport at Near Constant Bridge Energy
through Fluorene Oligomers

2.1 Introduction

Efficient long distance electron transfer is a prerequisite for molecular materials designed to serve as active components in solar cells and in some nano-scale devices. Being able to consistently achieve “wire-like” charge transport in synthetic systems requires a thorough understanding of the mechanisms involved. Recent progress has been made toward this goal^{56, 57}, but the complexity of even simple molecular systems poses a formidable challenge. In particular, the distance dependence of electron transfer has been shown to be a complex function of individual parameters including molecular geometry and energetics^{26, 47}. While the use of rigidly bound electron donor (D), bridge (B), electron acceptor (A) compounds has simplified the investigation of the distance dependence of electron transfer by keeping the donor-acceptor distance (r_{DA}) well defined, it is difficult to vary r_{DA} by changing the length of the bridge, without substantially altering the energy levels of the bridge.

In this report we examine electron transfer in a system in which r_{DA} can be changed considerably, while the oxidation potential of the intervening bridge changes very little. Approximate matching between the donor and bridge energy levels^{55, 56, 58} has been shown to be critical for promoting incoherent, or “wire-like” transport over coherent, or exponentially distance dependent superexchange transport.²⁰ These earlier studies have shown how the energetic convergence of the relevant donor and bridge results in a minimal injection barrier for hole transfer to the bridge, leading to a striking change in mechanism as the bridge is lengthened.

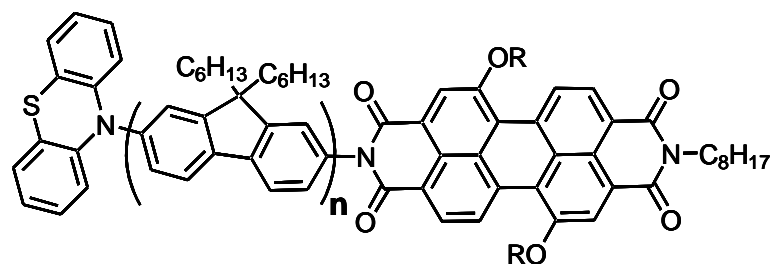
The relative importance of incoherent transport at larger values of r_{DA} has been confirmed by independent measurements of the decreasing contribution of superexchange to the overall electron transfer rate with increasing length.^{56, 59} The indirect electronic coupling between the

electron donor and acceptor via the bridge orbitals, V_{DA} , that is a result of superexchange⁷ is the same interaction responsible for long distance communication between the spins within a radical pair (RP), provided that the initial states are paramagnetic^{8, 18, 19, 60, 61}, which is true for the charge recombination process in the systems studied here. The magnetic field effect (MFE) on the yield of spin-selective RP recombination products directly reveals the magnitude of magnetic coupling between the spins of the RP, and is proportional to V_{DA}^2 .^{56, 62-64} The mechanistic details of the radical pair intersystem crossing mechanism (RP-ISC) and the theory behind the MFE have been researched extensively⁶⁵ and applied to many donor-acceptor systems^{56, 59, 66-70}. Following rapid charge separation, $^1(D^{+\bullet}-B-A^{\bullet-})$, which is initially formed in its singlet configuration, undergoes electron-nuclear hyperfine coupling-induced RP-ISC to produce $^3(D^{+\bullet}-B-A^{\bullet-})$. The charge recombination process is spin selective, i.e. $^1(D^{+\bullet}-B-A^{\bullet-})$ recombines to the singlet ground state D-B-A, and $^3(D^{+\bullet}-B-A^{\bullet-})$ recombines to yield the neutral triplet $^3(D-B-A)$. Application of a static magnetic field results in Zeeman splitting of the $^3(D^{+\bullet}-B-A^{\bullet-})$ triplet energy levels. When the Zeeman splitting equals the intrinsic singlet-triplet splitting, $2J$, of the RP, there is an increase in the intersystem crossing rate. This increase translates into a maximum in $^3(D^{+\bullet}-B-A^{\bullet-})$ production, and therefore a maximum in $^3(D-B-A)$ yield upon recombination. By monitoring the yield of $^3(D-B-A)$ as a function of applied magnetic field, $2J$ —the magnitude of the superexchange interaction^{19, 71}—can be measured directly.

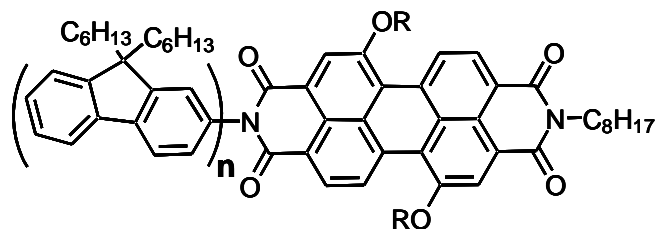
2.2 Results and Discussion

2.2.1 Molecular Geometries and Energy Levels

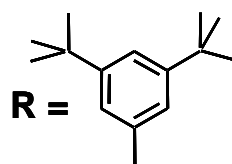
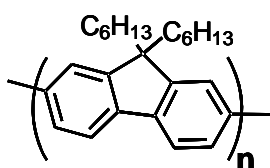
Calculations on structures geometry optimized at the AM1 level show that the FL units have torsional angles of 85° , 59° , and 37° relative to PTZ, PDI, and adjacent FL units, respectively, in the ground states of **1-4**, Figure 1. The donor-acceptor distances, r_{DA} , are measured between the centroid of the unpaired spin distributions of $\text{PTZ}^{+\bullet}$ and PDI^{\bullet} , which were in turn calculated by subtracting the β spin density from the α spin density on the diagonal of the calculated spin density matrices given by unrestricted Hartree-Fock molecular orbital calculations using the AM1 model. The energy-minimized electronic structures of $\text{FL}_n^{+\bullet}$, where $n = 1-4$, were determined by unrestricted Hartree-Fock calculations within the AM1



1-4 (n=1-4)



5-7 (n=1-3)



8-11 (n=1-4)

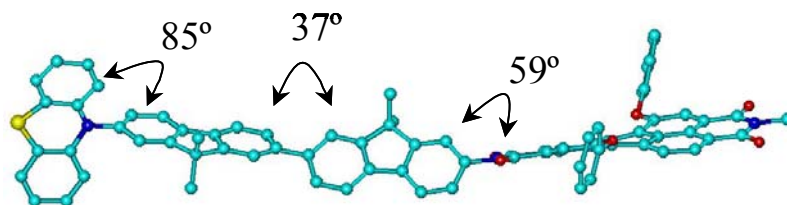


Figure 1 Structures of D/A derivatives of fluorene oligomers

model. The highest occupied molecular orbitals (HOMOs) for $n = 2-4$ are shown in Figure 2.

The calculations show that the FL-FL torsional angles decrease and the charge densities for FL₂ are distributed roughly equally throughout the bridge. However, FL₃^{•+} begins to show significant accumulation of charge density at the terminal FL units, which is accentuated in FL₄^{•+}. Thus once the FL bridge becomes longer than one unit, the charge density is localized on at most two FL molecules of the bridge. As will be discussed below, this feature will prove critical to efficient charge transport through the fluorene oligomer.

The energies of the PTZ^{•+}-FL_n-PDI[•] radical ion pairs presented in Table 2 are calculated from the one-electron redox potentials for oxidation and reduction of the electron donor and acceptor, respectively, and the distance, r_{DA} , between them using the Weller expression¹³ based on the Born dielectric continuum model,

$$\Delta G_{IP} = E_{ox} - E_{red} - \frac{e^2}{r_{DA}\epsilon_s} + e^2 \left(\frac{1}{2r_D} + \frac{1}{2r_A} \right) \left(\frac{1}{\epsilon_s} - \frac{1}{\epsilon_{sp}} \right) \quad (2.1)$$

where E_{ox} and E_{red} are, respectively, the oxidation and reduction potentials of the donor and acceptor in a polar solvent with dielectric constant ϵ_{sp} , e is the charge of the electron, r_D and r_A are the ionic radii of the radical ions, r_{DA} is the donor-acceptor distance, and ϵ_s is the static dielectric constant of the solvent in which the spectroscopy is performed ($\epsilon_s = 2.38$ for toluene).

The one-electron reduction of fluorene occurs at very negative potentials (< -2.5 V vs. SCE), making it unlikely that charge transfer proceeds via occupation of the lowest unoccupied molecular orbitals (LUMOs). The oxidation potentials of the oligofluorenes, relevant for hole transfer, were measured in dichloromethane and are summarized in Table 1. The potentials for $n = 1-3$ are reversible, whereas that for $n = 4$ is irreversible. The irreversibility in the latter case

makes E_{ox} somewhat more positive than the corresponding reversible potential, which should be considered in the analysis of bridge energies given below. For $n \geq 2$ the soft dependence of the oxidation potentials of FL_n on oligomer length is consistent with the oxidation potentials measured for other functionalized fluorene oligomers⁷² as well as the charge distributions found for the HOMOs of $FL_n^{+\bullet}$, Figure 2. In contrast, the potentials of the oligo(*p*-phenylenes)⁵⁶ and

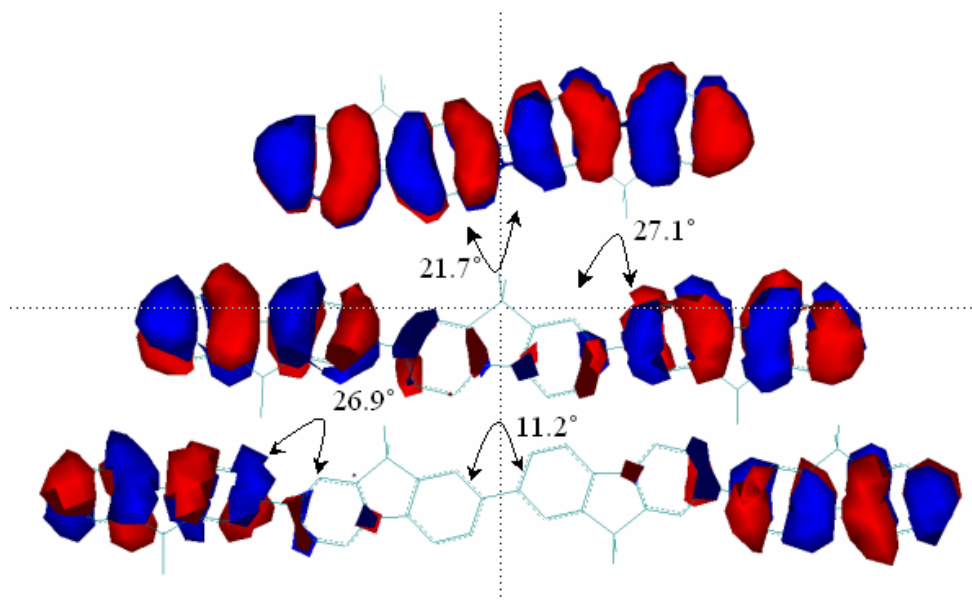


Figure 2 HOMO's of $FL_n^{+\bullet}$ for 2-4.

oligo(*p*-phenylenevinylenes)⁵⁵ studied previously vary by >1 V over similar distances. For those molecules that variation proved to be the most important factor influencing the injection barrier leading to the appearance of the incoherent hopping mechanism^{55,56}.

In order to obtain a clearer measure of the energy levels of the system in the solvent of interest, we measured one-electron oxidation potentials, E_{ox} , for the oligofluorenes directly in toluene using a microelectrode⁷³, Table 1. Unfortunately, the one-electron oxidation of the

oligofluorenes is chemically irreversible due to fast polymerization following oxidation,⁷⁴ which often proceeds well in non-polar solvent⁷⁵, so that these data cannot be used to calculate an

	PTZ _{ox}	PDI _{red}	FL _{1ox}	FL _{2ox}	FL _{3ox}	FL _{4ox}
E_{DCM}	0.32	-1.18	1.18	0.89	0.82	0.97 [†]
$E_{toluene}$	0.46 [†]	-1.36	1.11 [†]	1.05 [†]	1.10 [†]	1.10 [†]

Table 1 Summary of redox properties of the indicated species in the indicated solvents vs. Fc/Fc⁺.[†] Irreversible faradaic processes are reported as E_p values. The potentials for the oxidation of PTZ⁷⁶ and the reduction of PDI in dichloromethane⁷⁷ have been measured previously and are reversible

accurate value of ΔG_{IP} . Nevertheless, the data in Table 1 show that the observed oxidation potentials for FL_n in toluene are also weakly dependent on oligomer length. This is consistent with the picture that the charge density is primarily localized on two FL monomers when $n \geq 2$.

Calculating the energies of PTZ-FL_n^{+•}-PDI[•], the possible intermediate in the charge separation and recombination process, from the redox data in dichloromethane presents an additional complication, since our AM1 calculations show that half of the positive charge density is localized on each of the two terminal FL monomers of FL_n^{+•}, when $n \geq 2$. Equation 2.1 can be readily modified to accommodate this situation using positive ions having half of a formal charge at each of the terminal FL monomers and a single negative charge on PDI. The modified version of Equation 2.1 is shown below. The energies of PTZ-FL_n^{+•}-PDI[•] calculated in this manner are given in Table 2.

$$\Delta G_{IP} = E_{ox} - E_{red} + \frac{e^2}{\epsilon_s} \left(\frac{0.25}{r_{12}} - \frac{0.5}{r_{13}} - \frac{0.5}{r_{23}} \right) + e^2 \left(\frac{0.25}{2r_1} + \frac{0.25}{2r_2} + \frac{1}{2r_3} \right) \left(\frac{1}{\epsilon_s} - \frac{1}{\epsilon_{sp}} \right) \quad (2.2)$$

Here, E_{ox} and E_{red} are, respectively, the oxidation and reduction potentials of the fluorene donor and PDI acceptor in a polar solvent with dielectric constant ϵ_{sp} , e is the charge of the electron, $r_1 = r_2 = 4.5 \text{ \AA}$ are the ionic radii of the FL positive ions bearing one-half of a formal electronic charge, $r_3 = 7.6 \text{ \AA}$ is the radius of PDI $^{\bullet}$ bearing a unit formal electronic charge, r_{12} is the distance between the two FL monomers each bearing one-half of a formal electronic charge, r_{13} and r_{23} are the respective distances between these two FL units and PDI $^{\bullet}$ and $\epsilon_s = 2.38$ is the static dielectric constant of toluene in which the spectroscopy is performed.

PTZ-FL _n -PDI	PTZ $^{+\bullet}$ -FL _n -PDI $^{\bullet}$ ΔG_{IP} (eV)	PTZ-FL _n $^{+\bullet}$ -PDI $^{\bullet}$ ΔG_{IP} (eV)	k_{CS} (FS-TA) (s $^{-1}$)	k_{CS} , (TRF) (s $^{-1}$)	k_{CR} (s $^{-1}$)
n = 1	1.88	2.56	1.3×10^{10}	1.3×10^{10}	4.3×10^7
n = 2	2.00	2.36	1.6×10^9	1.6×10^9	3.4×10^6
n = 3	2.06	2.22	1.0×10^9	6.3×10^8	1.8×10^7
n = 4	2.10	2.37	4.2×10^8	3.3×10^8	5.9×10^7

Table 2 Summary of free energies of formation of radical ion pairs calculated as described in the text as well as rate constants for charge separation, k_{CS} , and recombination, k_{CR} . Values of free energies are accurate to approximately ± 0.1 eV. All values of k_{CS} were measured via femtosecond transient absorption (FS-TA) and time resolved fluorescence (TRF). All values of k_{CR} were measured by nanosecond transient absorption, with 1-3 measured from PDI $^{\bullet}$ decay at 720 nm and 4 measured from 3 PDI formation at 455 nm.

The steady-state optical absorption spectra of PTZ-FL_n-PDI (n=1-4), Figure 3, show that the PDI chromophore ($\lambda_{max} = 494 \text{ nm}$)⁷⁸ is unperturbed by the attached fluorene groups, while the absorption at the blue end of the spectra due to the FL oligomer^{79, 80} red shifts and increases in intensity as the bridge length increases. Note, however, that the incremental red shift exhibited by adding additional FL monomers to the oligomer is relatively small following addition of the second fluorene, and is already beginning to saturate at n = 4. The small shift of

the absorption maximum for $n \geq 2$ mirrors the weak length dependence of the FL_n oxidation potentials. Our AM1 calculations indicate that changes in the energies of the LUMOs of FL_n also contribute to the observed spectral shifts.

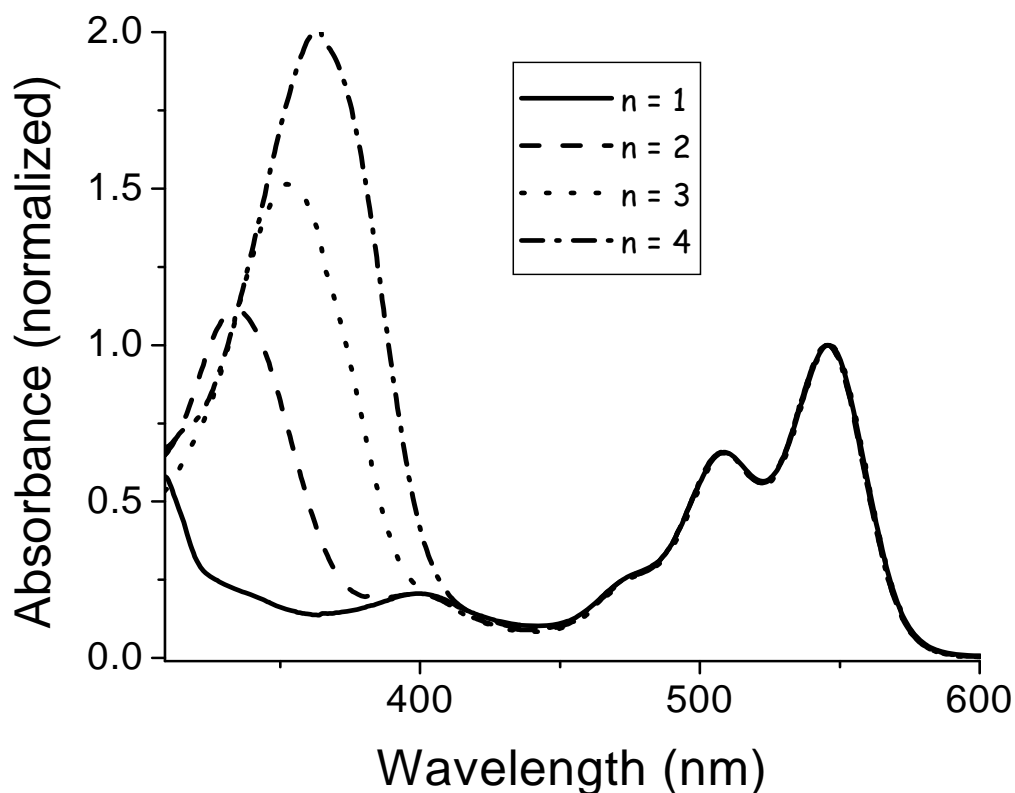


Figure 3 Steady-state absorption spectra of PTZ- FL_n -PDI in toluene.

2.2.2 Charge Separation and Recombination Dynamics

$PTZ^{+\bullet}$ and $FL^{+\bullet}$ have been shown to weakly absorb at 520 nm and 630 nm, respectively,⁸¹ yet both absorptions are obscured by the ground state bleach of PDI. Consequently, the lack of direct spectroscopic evidence for the formation of $PTZ^{+\bullet}$ and thus, for formation of the distal radical pair, $PTZ^{+\bullet}$ - FL_n - PDI^{\bullet} , necessitates an examination of model compounds of the type, FL_n -PDI, **5-7**, to see if the FL_n bridge itself can serve as a donor. The fluorescence lifetimes of **5-7** as

well as their fluorescence quantum yields are all within experimental error of those of PDI alone, 4.4 ns and 1.0, respectively. Thus, electron transfer does not occur in **5-7** leading to $FL_n^{+\bullet}$ -PDI $^{\bullet}$.

One of the products of charge separation, PDI $^{\bullet}$, absorbs strongly at 720 nm ($\epsilon = 8.0 \times 10^4 \text{ M}^{-1} \text{ cm}^{-1}$)⁷⁸, making it a convenient spectral feature to monitor during transient absorption measurements. Charge separation was identified following excitation of **1-4** with 510 nm, 150 fs laser pulses by the formation of PDI $^{\bullet}$ following the initial formation of 1^*PDI , which absorbs broadly in the same region. The transient absorption spectra for **2** at 2 and 952 ps after the laser

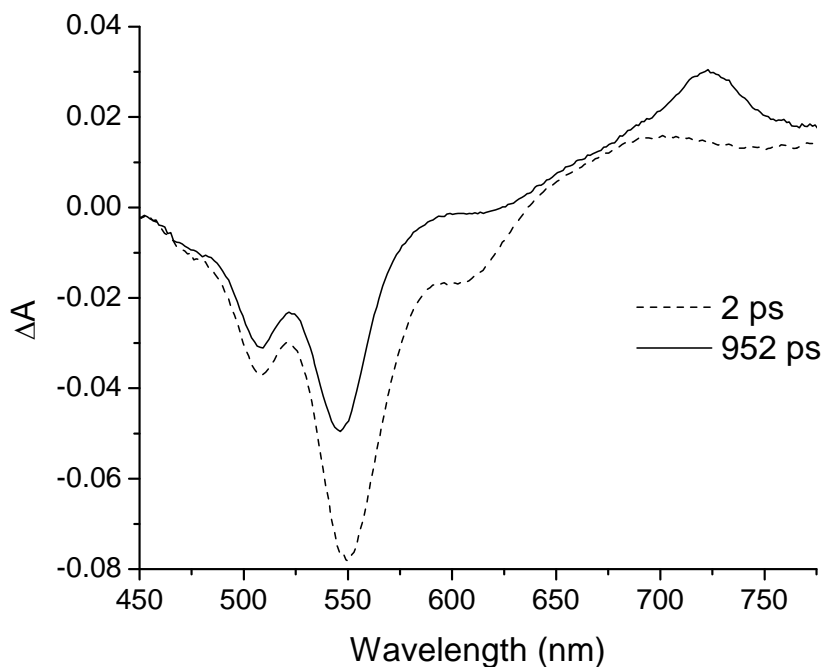


Figure 4 Transient absorption spectra of **2** following a 530 nm, 130 fs laser excitation pulse.

flash are given in Figure 4 and are typical of the time-resolved spectra observed for the series⁵⁶.

At early times, $t = 2 \text{ ps}$, the ground state bleach (510 and 550 nm), stimulated emission from

^1PDI (620 nm) and absorption from ^1PDI (675-715 nm) are apparent, while at $t = 952$ ps, the band at 720 nm due to the formation of $\text{PDI}\cdot$ is observed. For **1-3**, rate constants measured from the rise of the absorption of $\text{PDI}\cdot$, the decay of ^1PDI stimulated emission, and from the recovery of the ground state bleach were averaged to yield the rate constants presented in Table 2. For **4**, rate constants obtained from the formation of $\text{PDI}\cdot$ were contaminated to a significant degree by the absorption of ^1PDI , so that the rate constant reported in Table 2 was obtained only from the decay of the ^1PDI stimulated emission and the recovery of the ground state bleach and is therefore less accurate than those for **1-3**. For comparison, the charge separation rate constants were also obtained using time-resolved fluorescence decay data, and were calculated using the expression $k_{CS} = (1/\tau_{obs}) - (1/\tau_0)$, where $\tau_0 = 4.4$ ns is the lifetime of ^1PDI , Table 2. Good agreement between TRF and TA is obtained.

The distance dependence of the charge separation rate constants measured by TA is plotted in Figure 5. The electron transfer rate k_{ET} via superexchange has been shown to follow an exponential distance dependence, $k_{ET} = k_0 e^{-\beta(r-r_0)}$. The data points for **2-4** in Figure 5A can be fit reasonably well ($R^2=0.98$) to this equation, with $\beta = 0.093 \text{ \AA}^{-1}$. However, the relative distance independence that such a small β implies has in the past been shown to be indicative of hopping transport⁸². This mode of transport requires the formation of an oxidized bridge, $\text{PTZ-FL}_n^+\cdot\text{-PDI}\cdot$, and the energies to form that state are summarized in Table 2. The energy barrier for charge injection $\text{PTZ-FL}_n\text{-}^1\text{PDI} \rightarrow \text{PTZ-FL}_n^+\cdot\text{-PDI}\cdot$ can be calculated by subtracting the calculated energies of those two states and is 0.35 eV for **1** and drops considerably to 0.15, 0.01, and 0.15 for **2-4**, respectively. The barrier for **4** is probably somewhat high due to the irreversible nature of E_{ox} for FL_4 discussed above. The large barrier for **1** makes it likely that

the superexchange mechanism dominates, but the relatively small barriers observed for **2-4** are small enough to allow access to the oxidized bridge state^{55, 83}. Strictly speaking, the assumptions intrinsic to the simple superexchange model break down when the injection barriers are small. The rate of hopping transport should exhibit a $1/r_{DA}$ dependence²⁶. Plotting the rate constants for charge separation vs. $1/r_{DA}$, Figure 5B, shows that the experimental data for **2-4** fit well by this model ($R^2 = 0.99$). Thus it is likely that charge separation within **1** occurs via superexchange, while that within **2-4** occurs via hopping. Charge recombination within $PTZ^{+•}-FL_n-PDI^{•}$ occurs on the nanosecond time scale and results in the formation of 3PDI , which absorbs at 455 nm⁵⁶, as well as repopulation of the singlet ground state. The formation of 3PDI is a consequence of RP-ISC within $PTZ^{+•}-FL_n-PDI^{•}$ ⁸⁴

A plot of $\log k_{CR}$ vs. r_{DA} in Figure 6 shows that the rate for **2** exhibits the initial steep drop relative to that of **1** signaling the exponential distance dependence expected from superexchange-dominated transport in DBA's.^{4, 55, 56, 85, 86} In contrast, the charge recombination rates for **3** and **4** actually increase with distance, to the degree that the longest molecule, **4** recombines slightly faster than the shortest one, **1**. We have seen this turn-over behavior before in other systems^{55, 56}, although never to this extent. We attribute this behavior to the near resonance of the energy

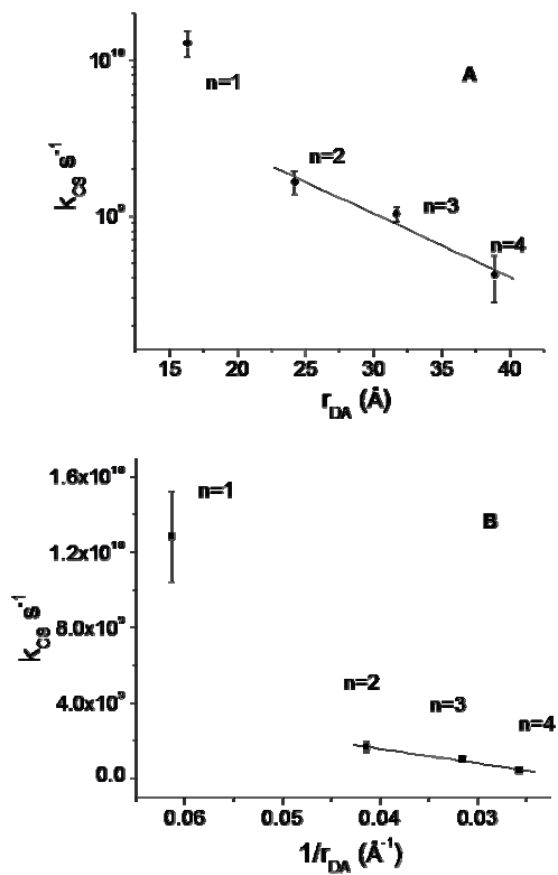


Figure 5 (A) Plot of $\log k_{CS}$ vs. distance, and (B) plot of k_{CS} vs. $1/\text{distance}$ for photoinduced charge separation in PTZ-FL_n-PDI in toluene.

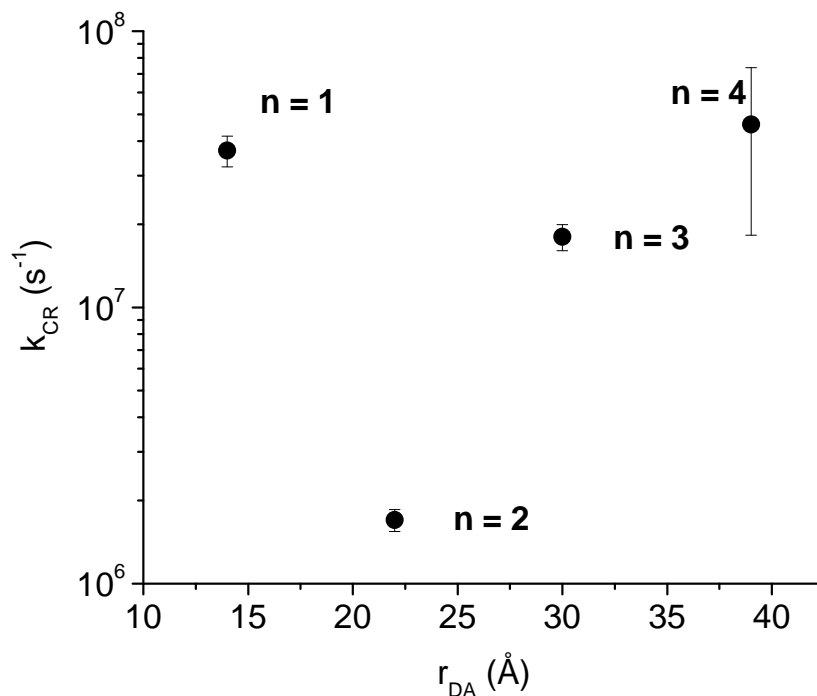


Figure 6 Plot of rate constant vs. distance for charge recombination of $\text{PTZ}^{+\bullet}\text{-FL}_n\text{-PDI}^{\bullet}$ in toluene.

level of the fully charge separated state, $\text{D}^{+\bullet}\text{-B-A}^{\bullet}$, with that of the $\text{D-B}^{+\bullet}\text{-A}^{\bullet}$ intermediate in the incoherent charge recombination process. Such an energetic resonance minimizes the injection barrier for moving the hole from the donor to the bridge, resulting in a faster process. The data in Table 2 show that the injection barriers for the charge recombination reaction

$\text{PTZ}^{+\bullet}\text{-FL}_n\text{-PDI}^{\bullet} \rightarrow \text{PTZ-FL}_n^{+\bullet}\text{-PDI}^{\bullet}$ are reasonably large, 0.68 eV and 0.36 eV for **1** and **2**, respectively, yet drop to 0.16 and 0.26 eV for **3** and **4**, respectively. Once again, the barrier for **4** is probably somewhat high due to the irreversible nature of E_{ox} for FL_4 discussed above. This suggests that charge recombination in both **1** and **2** should be dominated by superexchange, while that for **3** and **4** should be in the hopping regime because only **3** and **4** have thermally accessible bridge occupation. An alternative explanation for increasing rates as a function of

distance lies in a shifting solvent reorganization energy, λ_s , which lowers the effective injection barrier for the longer systems. However, analysis has shown^{87, 88} that in a quadrupolar solvent like toluene, λ_s should be virtually distance independent at the radical ion pair distances in **1-4**.

Once the injection barrier for placing positive charge onto the FL_n bridge is sufficiently low, the electronic structure of $FL_n^{+\bullet}$ plays a key role in propagating the charge through the bridge. The observed changes in the $FL_n^{+\bullet}$ electronic structure are consistent with the experimentally observed quinoid geometry that the fluorene cation adopts following oxidation⁸⁹. Our electronic structure calculations show that the FL-FL dihedral angles are about 37° in the ground state, and decrease by about $10-20^\circ$ in $FL_n^{+\bullet}$. These relatively small changes in torsional angle most likely occur much more rapidly than the fastest electron transfer rates measured for charge separation and recombination in **1-4**. For example, the torsional frequency of biphenyl is 55 cm^{-1} ⁹⁰, which implies that small amplitude motions along this coordinate can occur in < 1 ps.

The nature of the contact between the bridge and charge reservoirs has been shown to be of crucial importance in determining charge transport properties of molecules at metal junctions^{91, 92}. In molecular systems, μ_{RP} , the transition dipole moment between the initial and final states is related to the orbital overlap between those initial and final states⁸³. The accumulation of charge density on the two terminal FL monomers of the bridge for $n \geq 2$ is very favorable for efficient coupling to the donor and acceptor groups, and is only accessible after the bridge has been oxidized. The increase in charge recombination rates observed in transitioning from the superexchange regime to the hopping regime most likely reflects the efficient coupling imparted by the $FL_n^{+\bullet}$ charge distribution.

2.2.3 Magnetic Field Effects: Superexchange vs. Hopping

The charge recombination dynamics of $\text{PTZ}^{+\bullet}\text{-FL}_n\text{-PDI}^{\bullet}$ can be altered by the presence of an applied magnetic field. When the Zeeman splitting induced by the applied magnetic field is equal to the singlet-triplet energy gap, $2J$, of the radical ion pair, the T_{-1} state of the radical ion pair is resonant with its singlet state. This results in an increase in the RP-ISC rate, which maximizes the ^3PDI population, and in turn minimizes the overall radical ion pair population. This minimum in the radical ion pair population in systems related to ours correlates well with the maximum in the yield of ^3PDI , and indicates that the triplet recombination pathway dominates the singlet pathway⁵⁶. These observations are consistent with the fact that the small reorganization energies for charge recombination, approximately 0.6 eV for these molecules in toluene⁵⁶, put the reaction $^1(\text{PTZ}^{+\bullet}\text{-FL}_n\text{-PDI}^{\bullet}) \rightarrow \text{PTZ-FL}_n\text{-PDI}$ ($\Delta G \cong -2.0$ eV) well into the Marcus inverted region⁷, while the corresponding triplet process $^3(\text{PTZ}^{+\bullet}\text{-FL}_n\text{-PDI}^{\bullet}) \rightarrow \text{PTZ-FL}_n\text{-}^3\text{PDI}$ ($\Delta G \cong -1.0$ eV) is closer to the peak of the rate vs. free energy profile, resulting in a faster ET process.

The resonances seen in the plots of ^3PDI population vs. magnetic field strength, Figure 7, mark the energy level crossing between $^1[\text{PTZ}^{+\bullet}\text{-FL}_n\text{-PDI}^{\bullet}]$, and the T_{-1} state of $^3[\text{PTZ}^{+\bullet}\text{-FL}_n\text{-PDI}^{\bullet}]$, where RP-ISC is most efficient, and thus directly yield the singlet-triplet splitting, $2J$. No resonance was observed for compound **1**, which most likely results from the magnitude of $2J$

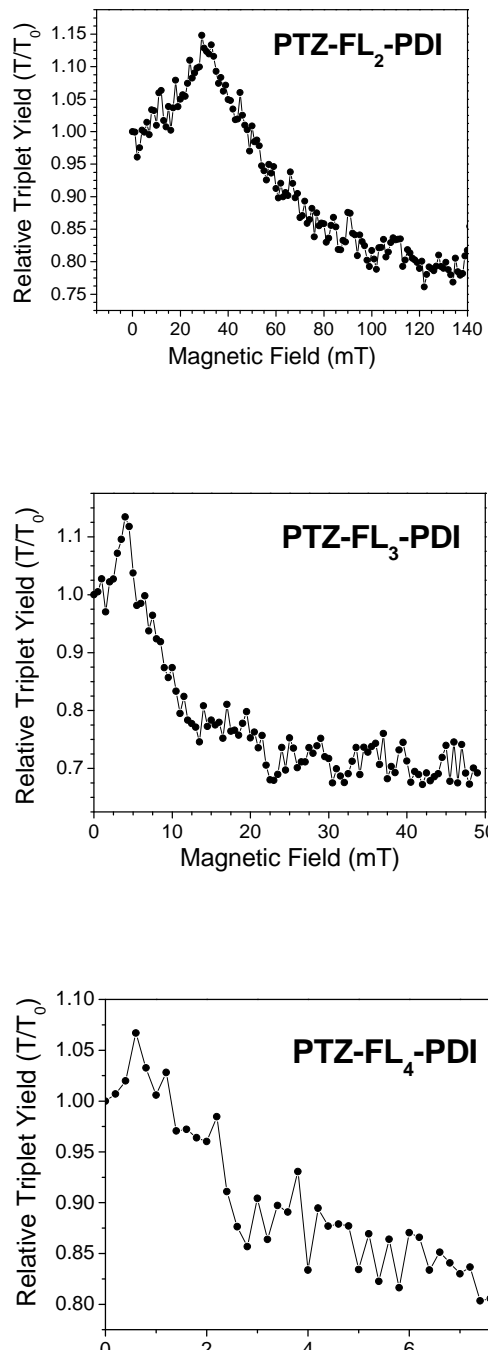


Figure 7 Plots of the relative yield of ^3PDI vs. magnetic field strength for the indicated molecules in toluene.

being larger than the magnetic field that our apparatus can apply (1.2 T). Measurements of $2J$ have been shown to provide a measure of the electronic coupling for charge recombination via superexchange^{18, 19, 60} and have been used as a probe of electron transfer mechanism in a number of studies.^{56, 59, 62, 64, 93, 94} Most importantly, the energetic splitting between the singlet and triplet states within the radical ion pair arises from an indirect exchange between the two spins made possible by their interaction with the bridge. This *superexchange* interaction results in a gap between the singlet and triplet manifold that is proportional to the square of the magnitude of the one-electron coupling,^{13, 56} $2J \propto V^2 = V_o^2 e^{-2\alpha r_{DA}}$. Thus the distance dependence of $2J$ will parallel that of V_{DA} .

Fitting the $2J$ values to an exponential distance dependence yields a good fit ($R^2=0.99$) with $2\alpha = 0.27 \text{ \AA}^{-1}$, Figure 8. The observed dependence of $2J$ on r_{DA} provides further evidence that distal radical pair, $\text{PTZ}^{+\bullet}\text{-FL}_n\text{-PDI}^\bullet$, is being formed in all cases. The increased coupling in the radical cation geometries is not seen in the measurement of $2J$ because the majority of RP-ISC occurs in the fully separated charge transfer state, before the bridge is oxidized and the conformational change occurs. The decreasing electronic communication between the donor and acceptor with distance strongly implies a decreasing contribution of superexchange to the overall electron transfer rate in the longer DBA molecules. Consistent with our charge recombination rates, superexchange likely dominates charge recombination in **1** and **2**, but is substantially diminished in **3** and **4**, so that incoherent hopping prevails during recombination for **3** and **4**.

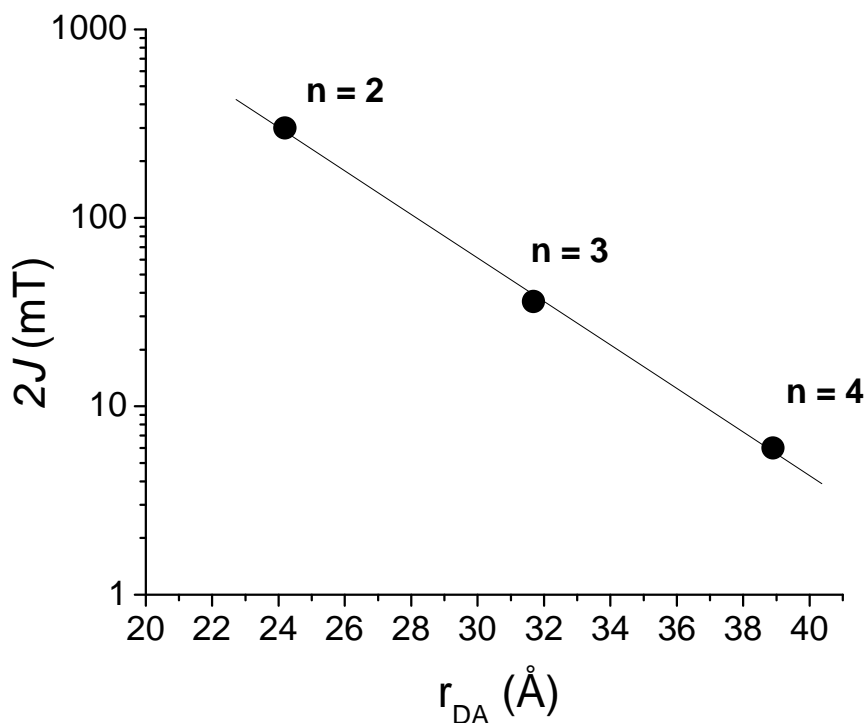


Figure 8 Logarithmic plot of the spin-spin exchange interaction, $2J$, vs. r_{DA} .

2.3 Conclusion

The electronic structure of fluorene oligomers provides a means to access the wire-like incoherent hopping regime for hole transport over long distances at nearly constant bridge energy. This is a consequence of the localization of charge at the two terminal monomers within the $FL_n^{+\bullet}$ bridge. This localization provides excellent electronic coupling between the donor and the bridge as well as the bridge and the acceptor. We are continuing to pursue a rigorous understanding of how molecular architecture determines access to the incoherent hopping mechanism at long distances. This understanding is crucial to the exploitation of wire-like behavior to make molecular connections between nano-scale devices.

Acknowledgements: Louise Sinks and Richard Kelley (femtosecond transient absorption spectroscopy), Laura Betzen and Wenhao Liu (time resolved fluorescence), Emily Weiss (helpful conversations)

2.4 Synthesis

2,7-dibromo-9,9-dihexyl-9H-fluorene (**Br-FL-Br**)

2,7-Dibromofluorene (1 g, 3.1 mmol), 1-bromohexane (1.26 g, 7.7 mmol), potassium hydroxide (730 mg, 13mmol), and potassium iodide (50 mg, 0.3 mmol) were combined suspended in 50 ml acetonitrile and heated at 60°C for 24 hours. The solvent was removed using a rotary evaporator. The crude product was suspended in chloroform, washed with water, dilute acetic acid, then twice more with water, and then purified by column chromatography on silica using hexanes as the mobile phase to afford (**Br-FL-Br**) (1.14g, 75%). ¹H NMR (CDCl₃) δ: 7.52(m, 2H), 7.43(m, 4H), 1.93(t, J=8.3Hz, 4H), 1.32-1.00(m, 12H), 0.79(t, J=7.1Hz, 6H), 0.59 (m, 4H)

10-(7-bromo-9,9-dihexyl-9H-fluoren-2-yl)-10H-phenothiazine (**Br-FL-PTZ**)

Br-FL-Br (800 mg, 1.33 mmol) and phenothiazine (**PTZ**) (242 mg, 1.2 mmol) were suspended in 60 ml toluene and N₂ was bubbled through for 20 minutes. Potassium tert-butoxide (136 mg, 1.2 mmol), tris(dibenzylideneacetone)dipalladium(0) (30 mg, 0.26 mmol), and tri-*o*-tolylphosphine (100 mg, .33 mmol) were then added and the reaction was heated under nitrogen at 90°C for 24 hours. The solvent was removed by rotary evaporation and the product was purified by column chromatography with silica with a 9:1 (V/V) combination of hexanes and chloroform to obtain the product, (**Br-FL-PTZ**) (230 mg, 23%). M. S. : 610.79 (calcd. 609.21). ¹H NMR (CDCl₃) δ: 7.82 (d, J = 8.5Hz, 1H), 7.54 (d, J=8.5Hz, 1H), 7.44 (m, 2H), 7.29 (m,

2H), 6.96 (m, 2H), 6.74 (m, 4H), 6.13 (m, 2H), 1.90 (t, J=8.3Hz, 4H) 1.07-1.01 (m, 12H), 0.79 (t, J= 7.1Hz, 6H), 0.67(m, 4H).

9,9-Dihexyl-7-phenothiazin-10-yl-9H-fluoren-2-ylamine (PTZ-FL-NH2)

Br-FL-PTZ (230 mg, 0.38 mmol) was combined with benzophenone imine (83 mg, 0.46 mmol) in 5 ml of toluene and N₂ was bubbled through the mixture for 20 minutes. Tris(dibenzylideneacetone)dipalladium(0) (4 mg, 0.035 mmol), 2,2'-bis(diphenylphosphino)-1,1'-binaphthyl (BINAP, 7 mg, 0.011 mmol), and potassium tert-butoxide (60 mg, 0.53 mmol) were then added and the reaction was heated under N₂ at 80°C for 24 hours. Column chromatography with silica and a 1:1 (V/V) mixture of hexanes and chloroform as the mobile phase yielded a crude sample of benzhydrylidene-(9,9-dihexyl-7-phenothiazin-10-yl-9H-fluoren-2-yl), (**PTZ-FL-NCPH₂**). M. S. : 710.7 (calcd. 710.37). This crude product was then dissolved in 5 ml THF and several drops of HCl were added. Further chromatography in chloroform separated out the benzophenone byproduct and yielded 9,9-dihexyl-7-phenothiazin-10-yl-9H-fluoren-2-ylamine, (**PTZ-FL-NH2**) (36 mg, 17% over both steps) M. S.: 547.9 (calcd. 546.31) ¹H NMR (CDCl₃) δ: 7.68 (d, J=8.2Hz, 1H), 7.46 (d, J=8.6Hz, 1H), 7.20(d + s, 2H), 6.92 (m, 2H), 6.71 (m, 4H), 6.63 (d + s, 2H), 6.15 (m, 2H), 3.79 (br, 2H), 1.83 (m, 4H), 0.99 (m, 12H), 0.67 (t, 6H, J=7.1Hz), 0.56(m, 4H).

N-(octyl)-*N*-(7-phenothiazin-10-yl-9,9-dihexyl-9H-fluoren-2-yl)-(3',5'-di-*t*-butylphenoxy)perylene-3,4:9,10-bis(dicarboximide) (**PTZ-FL-PDI**)

PTZ-FL-NH2 (36 mg, 0.066 mmol) and **PIA** (*N*-octyl-1,7-bis(3',5'-di-*t*-butylphenoxy)-perylene-3,4-dicarboxyanhydride-dicarboximide was synthesized as reported earlier⁷⁸). (25 mg, 0.028 mmol) were combined in 6 ml of DMF with a catalytic amount of zinc acetate, sparged

with N₂ and set to reflux for 24 hours. Silica column chromatography was performed with a 7:3 (V/V) chloroform and hexanes mixture to afford the product, *N*-(octyl)-*N*-(7-phenothiazin-10-yl-9H-fluoren-2-yl)-(3',5'-di-*t*-butylphenoxy)perylene-3,4:9,10-bis(dicarboximide) (**PTZ-FL-PDI**) (16 mg, 40%) HPLC purification was performed isocratically with a 70:30 V/V acetonitrile/chloroform eluent on C-18 reverse phase column (Altex) for spectroscopic samples. M. S.: 1441.0 (calcd. 1439.77) ¹H NMR (CDCl₃) δ: 9.68 (d + d, 2H), 8.65 (d, J=8.4 Hz, 1H), 8.60 (d, J=8.4 Hz, 1H), 8.35 (s, 1H), 8.32(s, 1H), 7.90(d, J=7.9 Hz), 7.83 (d, J=8.7 Hz, 1H), 7.47 (m, 1H), 7.36-7.24 (m, 4H), 7.06-6.94 (m, 6H), 6.75 (m, 4H), 6.17(m, 2H), 4.09 (t, J=6.9Hz, 2H), 2.27 (m, 2H), 1.92 (t, J=7.3 Hz, 4H), 1.73(m, 3H), 1.39-0.96 (m, 62H), 0.68 (t, J=6.9 Hz, 6H).

7-Bromo-9,9-dihexyl-9H-fluoren-2-ylamine (Br-FL-NH₂)

2,7 (**Br-FL-Br**) (3.35 g, 6.8 mmol) was combined with benzophenone imine (1.27g, 7.0 mmol) in 50 ml of toluene and N₂ was bubbled through the mixture for 20 minutes. Tris(dibenzylideneacetone)dipalladium(0) (65 mg, 0.55 mmol), 2,2'-bis(diphenylphosphino)-1,1'-binaphthyl (BINAP, 7 mg, 0.20 mmol), and potassium tert-butoxide (980 mg, 8.7 mmol) were then added and the reaction was heated under N₂ at 80°C for 24 hours. Column chromatography with silica and a 1:1 (V/V) mixture of hexanes and chloroform as the mobile phase yielded a crude sample of benzhydrylidene-(7-bromo-9,9-dihexyl-9H-fluoren-2-yl)-amine, (**Br-FL-NCPh₂**). This crude product was then dissolved in 10 ml THF and several drops of HCl were added. Further chromatography in chloroform separated out the benzophenone byproduct and yielded, **Br-FL-NH₂** (1.38 g, 48% over both steps) ¹H NMR (CDCl₃) δ: 7.44 (d, J=7.9Hz, 1H), 7.38(m, 3H), 6.65(m, 2H), 3.78(s, 2H), 1.86(m, 4H), 1.17-0.99(m, 12H), 0.78(t, J=7.2Hz, 6H), 0.63(m, 4H).

***N*-(octyl)-*N*-(7-bromo-9,9-dihexyl-9H-bifluoren-2-yl)-(3',5'-di-*t*-butylphenoxy)perylene-3,4:9,10-bis(dicarboximide) (Br-FL-PDI)**

Br-FL-NH₂ (140 mg, 0.33 mmol) and **PIA** (157 mg, 0.17 mmol) were suspended in 25 ml of quinoline and N₂ was bubbled for 20 min. Phosphorus pentoxide (10 mg) was then added and the reaction was heated under N₂ at 230°C for 2 days. After the solution was cooled, the mixture was poured onto 125 ml of 18% HCl. The product was extracted into chloroform and washed with water. The chloroform was removed under reduced pressure and column chromatography was performed with chloroform as the mobile phase to yield **Br-FL-PDI** (98 mg, 43%). M. S.: 1320.79 (calcd. 1320.65) ¹H NMR (CDCl₃) δ: 9.60 (d+d[appears as t], 2H), 8.59 (d, J=8.5Hz, 1H), 8.53 (d, J=8.4Hz, 1H), 8.28(s, 1H), 8.21(s, 1H), 7.70(d, J=8.7, 1H), 7.50 (d, J=7.9, 1H), 7.41(s, 1H), 7.28(m, 2H), 7.22(m, 2H), 7.17(s, 1H), 6.96(d, J=1.5Hz, 2H), 6.95(d, J=1.5Hz, 2H), 4.06(t, J=7.5Hz, 2H), 1.89-1.75(m, 6H), 1.63(m, 3H), 1.32-0.99(m, 58H), 0.78 (t, J=6.8Hz, 4H), 0.69(m, 4H).

10-[9,9-Dihexyl-7-(4,4,5,5-tetramethyl-[1,3,2]dioxaborolan-2-yl)-9H-fluoren-2-yl]-10H-phenothiazine (PTZ-FL-BE)

PTZ-FL-Br (297 mg, 0.49 mmol), 4,4,5,5-tetramethyl-[1,3,2]dioxaborolane (190 mg, 1.5 mmol), and triethylamine (152 mg, 1.5 mmol) were added to 10 ml of dioxane and N₂ was bubbled through the mixture for 20 minutes. 1,1'-bis(diphenylphosphino)ferrocene dichloropalladium(II) (complex with dichloromethane, 60 mg, 0.074 mmol) was then added and the reaction was heated under N₂ at 95°C for 24 hours. The solvent was removed by rotary evaporation and column chromatography in 1:1 hexanes/chloroform yielded **PTZ-FL-BE** (86 mg, 27%). M. S.: 657.6 (calcd. 657.38) ¹H NMR (CDCl₃) δ: 7.88 (d, J=6.7H, 1H), 7.79(d,

$J=8.7\text{Hz}$, 1H), 7.70(m, 2H), 7.28(m, 2H), 6.94(m, 2H), 6.72(m, 4H), 6.14(m, 2H), 1.93(m, 4H), 1.32(s, 12H), 1.06-0.90(m, 12H), 0.67(t, $J=7.0\text{Hz}$, 6H), 0.57(m, 4H).

N-(octyl)-N-(7-phenothiazin-10-yl-9,9',9'-tetrahexyl-9H,9'H-[2,2']bifluorenyl)-(3',5'-di-*t*-butylphenoxy)perylene-3,4:9,10-bis(dicarboximide) (PTZ-FL₂-PDI)

PTZ-FL-BE (260 mg, 0.39 mmol) and **Br-FL-PDI** (45 mg, 0.034 mmol) were combined in 10 ml of dioxane with several drops of water and potassium carbonate (41 mg, 0.30 mmol) and sparged for 20 minutes. Tetrakis(triphenylphosphine)palladium (0) (~5 mg, 0.004 mmol), was then added and the reaction was heated under N₂ at 90°C for 24 hours. The solvent was removed by rotary evaporation. Column chromatography with a 7:3 chloroform/hexanes mixture yielded **PTZ-FL₂-PDI** (29 mg, 48%). M. S.: 1772.6 (calcd. 1772.02) ¹H NMR (CDCl₃) δ : 9.68(d + d, 2H), 8.65(d, $J=8.6\text{Hz}$, 1H), 8.61(d, $J=8.2\text{Hz}$, 1H), 8.35(s, 1H), 8.32(s, 1H), 7.89 (d, $J=7.8\text{Hz}$, 1H), 7.83-7.74 (m, 3H), 7.66-7.57(m, 4H), 7.48-7.28(m, 6H), 6.99(s, 2H), 6.96(m, 2H), 6.74(m, 4H), 6.18(m, 2H), 4.10(t, $J=7.5\text{Hz}$, 2H), 1.98(m, 6H), 1.84(m, 4H), 1.66(m, 3H), 1.30-0.90 (m, 70H), 0.70(m, 12H), 0.51(m, 8H). HPLC purification was performed isocratically with a 65:35 V/V acetonitrile/chloroform eluent on C-18 reverse phase column (Altex) for spectroscopic samples.

2,7-Bis(4,4,5,5-tetramethyl-1,3,2-dioxaborolan-2-yl)-9,9-dihexylfluorene(BE-FL-BE)

Br-FL-Br (1.9 g, 3.9 mmol) in 40 ml of THF was put under a N₂ atmosphere and cooled to -78°C. After the solution had been cooled, 1.6M *n*-butyl lithium in hexanes(5.35 ml, 8.56 mol) was then slowly added. 2-Isopropoxy-4,4,5,5-tetramethyl-[1,3,2]dioxaborolane (2.38 ml, 11.7 mmol) was then quickly added, the reaction was allowed to warm to room temperature, and was then stirred for 24 hours. The reaction was then poured over 200 ml of water and extracted into

diethyl ether, washed with brine, and dried over magnesium sulfate. The diethyl ether was removed under reduced pressure, and column chromatography was performed with 1:1 chloroform/hexanes to afford **BE-FL-BE** (567 mg, 25%). $^1\text{H NMR}$ (CDCl_3) δ : 7.83 (d, $J=7.6\text{Hz}$, 2H), 7.78(s, 2H), 7.74(d, $J=7.6\text{Hz}$, 2H), 2.00 (m, 4H), 1.39 (s, 24H), 1.12-0.94 (m, 12H), 0.76(t, $J=7.1\text{Hz}$, 6H), 0.56(m, 4H).

10-[9,9,9',9'-Tetrahexyl-7'-(4,4,5,5-tetramethyl-[1,3,2]dioxaborolan-2-yl)-9H,9'H-[2,2']bifluorenyl-7-yl]-10H-phenothiazine (BE-FL₂-PTZ)

BE-FL-BE (565 mg, 0.96 mmol) and **PTZ-FL-BR** (440 mg, 0.72 mmol) were combined in 40 ml of dioxane with several drops of water and potassium carbonate (200 mg, 1.4 mmol) and sparged for 20 minutes. Tetrakis(triphenylphosphine)palladium(0) (5 mg, 0.004 mmol), was then added and the reaction was put at 80°C for 6 hours. The solvent was removed by rotary evaporation. Column chromatography with a 1:1 chloroform/hexanes mixture yielded **BE-FL₂-PTZ** (214 mg, 30%). M. S.: 989.94 (calcd. 989.63) $^1\text{H NMR}$ (CDCl_3) δ : 7.97 (d, $J=7.9$, 1H), 7.87-7.64(m, 9H), 7.38(m, 2H), 7.03(m, 2H), 6.82(m, 4H), 6.26(m, 2H), 2.07(m, 8H), 1.41(s, 12H), 1.16-0.95 (m, 24H), 0.76(m, 20H).

N-(octyl)-N-(7-phenothiazin-10-yl-9,9,9',9',9'',9''-hexahexyl-9H,9'H,9''H-

[2,2',2'']terfluorenyl)-(3',5'-di-t-butylphenoxy)perylene-3,4:9,10-bis(dicarboximide) (PTZ-FL₃-PDI)

PTZ-FL₂-BE (214 mg, 0.22 mmol) and **Br-FL-PDI** (49 mg, 0.037 mmol) were combined in 10 ml of dioxane with several drops of water and potassium carbonate (30 mg, 0.22 mmol) and sparged for 20 minutes. Tetrakis(triphenylphosphine)palladium(0) (~5 mg, 0.004 mmol), was then added and the reaction was heated under N_2 at 90°C for 24 hours. The solvent was removed

by rotary evaporation. Column chromatography on silica gel with an 8:2 chloroform/hexanes mixture yielded **PTZ-FL₃-PDI** (43 mg, 55%). HPLC purification was performed isocratically with a 60:40 V/V acetonitrile/chloroform eluent on C-18 reverse phase column (Altex) for spectroscopic samples. M. S.: 2105.67 (calcd. 2104.27) ¹H NMR (CDCl₃) δ: 9.66(d + d, 2H), 8.65(d, J=8.4Hz, 1H), 8.60(d, J=8.4Hz, 1H), 8.34(s, 1H), 8.30(s, 1H), 7.90(d, J=7.7Hz, 1H), 7.82-7.75(m, 4H), 7.67-7.57(m, 9H), 7.34-7.18(m, 6H), 6.99(m, 4H), 6.95(m, 2H), 6.75(m, 4H), 6.18(m, 2H), 4.09(t, J=7.4Hz, 2H), 2.08-1.93(m, 14H), 1.66(m, 3H), 1.32-0.98(m, 82H), 0.70(m, 30H).

7,7''-Dibromo-9,9,9',9',9'',9''-hexahexyl-9H,9'H,9''H-terfluorene (Br-FL₃-Br)

FL-FL-FL (255 mg, 0.26 mmol) was dissolved in 1 ml of chloroform. ~1 mg of ferric chloride was added and the solution was cooled to 0°C. Bromine (43 mg, 0.27 mmol) in 0.5 ml of chloroform was then slowly added over 1 hour. The reaction was then left at room temperature overnight. The reaction was then poured onto 5 ml of water and the product was extracted into the chloroform and dried over magnesium sulfate. Column chromatography in 9:1 hexanes/chloroform yielded the product, **Br-FL₃-Br** (251 mg, 83%). M. S.: 1157.11 (calcd. 1154.59) ¹H NMR (CDCl₃) δ: 7.83(m, 2H), 7.76(m, 2H), 7.69-7.59(m, 7H), 7.57(s, 1H), 7.52-7.46(m, 6H), 2.02(m, 12H), 0.79(t, J=6.4Hz, 18H), 0.72(m, 12H).

10-[9,9,9',9',9'',9''-Hexahexyl-7''-(4,4,5,5-tetramethyl-[1,3,2]dioxaborolan-2-yl)-9H,9'H,9''H-[2,2';7',2'']terfluoren-7-yl]-10H-phenothiazine (BE-FL₃-PTZ)

Br-FL₃-Br (250 mg, 0.22 mmol) and phenothiazine (**PTZ**) (43 mg, 0.22 mmol) were suspended in 10 ml toluene and N₂ was bubbled through for 20 minutes. Potassium tert-butoxide (30 mg, 0.26 mmol), tris(dibenzylideneacetone)dipalladium(0) (4 mg, 0.034 mmol), and tri-o-

tolylphosphine (12 mg, .040 mmol) were then added and the reaction was heated under nitrogen at 90°C for 24 hours. The solvent was removed by rotary evaporation column chromatography with silica with a 7:3 (V/V) combination of hexanes and yielded a crude mixture of the desired product, **Br-FL₃-PTZ**, and the disubstituted product, **PTZ-FL₃-PTZ**. M.S.: 1275.9 (calcd. 1273.71). This crude mixture, along with 4,4,5,5,4',4',5',5'-octamethyl-[2,2']bi[[1,3,2]dioxaborolanyl] (140 mg, 0.53 mmol), and potassium acetate (150 mg, 1.53 mmol) was dissolved in 5 ml of DMF and sparged with N₂ for 20 minutes. 1,1'-bis(diphenylphosphino)ferrocene dichloropalladium(II) (complex with dichloromethane, 12 mg, 0.015 mmol) was then added along with extra 1,1' bis(diphenylphosphino)ferrocene (9 mg, 0.015 mmol) and the reaction was heated under N₂ at 90°C for 24 hours. The solvent was removed under reduced pressure and column chromatography with a 1:1 chloroform/hexanes mobile phase yielded the product, **BE-FL₃-PTZ** (13 mg, 4.4% over two steps). M. S.: 1321.94 (calcd. 1321.88) ¹H NMR (CDCl₃) δ: 7.90 (d, J=7.7Hz, 1H), 7.79-7.55(m, 14H), 7.33(s, 1H), 7.30(s, J=7.9Hz, 1H), 6.96(m, 2H), 6.75(m, 4H), 6.18(m, 2H), 2.00(m, 12H), 1.33(s, 12H), 1.09-0.95(m, 48H), 0.69(m, 30H).

***N*-(octyl)-*N*-(7-phenothiazin-10-yl-9,9',9'',9''',9''''',9''''',octahexyl-9H,9'H,9''H,9''''H,9''''')-[2,2',2'',2''''']tetrafluorenyl)-(3',5'-di-*t*-butylphenoxy)perylene-3,4:9,10-bis(dicarboximide) (PTZ-FL₄-PDI)**

PTZ-FL₃-BE (13 mg, 0.0097 mmol) and **Br-FL-PDI** (13 mg, 0.0097 mmol) were combined in 5 ml of dioxane with one drop of water and potassium carbonate (2 mg, 0.014 mmol) and sparged for 15 minutes. Tetrakis(triphenylphosphine)palladium(0) (~2 mg, 0.002 mmol), was then added and the reaction was heated under N₂ at 90°C for 24 hours. The solvent was removed by rotary evaporation. Column chromatography with a 6:4 chloroform/hexanes mixture yielded **PTZ-**

FL₄-PDI (9.3 mg, 39%). HPLC purification was performed isocratically with a 55:45 V/V acetonitrile/chloroform eluent on C-18 reverse phase column (Altex) for spectroscopic samples. M. S. : 2438.8 (calc'd 2436.52.) ¹H NMR (CDCl₃) δ: 9.67(d + d, 2H), 8.72(d, J=8.1Hz, 1H), 8.68 (d, J=8.2Hz, 1H), 8.43 (s, 1H), 8.40(s, 1H), 8.04(m, 1H), 7.97(d, J=8.1Hz, 1H), 7.91-7.81 (m, 7H), 7.74-7.64(m, 15H), 7.53(m, 1H), 7.42-7.30(m, 4H), 7.09-7.02(m, 6H), 6.82 (m, 4H), 6.25(m, 2H), 4.17(t, J=7.4Hz, 2H), 2.16-1.98(m, 18H), 1.71(m, 3H), 1.39-1.05(m, 110H), 0.78(m, 24H).

9,9-Dihexyl-2-nitro-9H-fluorene (FL-NO₂)

9,9-Dihexyl-9H-fluorene (5.1 g, 15 mmol) was dissolved in 15 ml of acetic acid and put at 60°C for 20 minutes. 3.5 ml of nitric acid was then added over 30 minutes. The mixture was then heated at 90°C for 40 minutes, then left to cool over night. The product was extracted into chloroform, washed with water several times, and the solution was evaporated under reduced pressure. Column chromatography was performed in 4:1 hexanes/chloroform to obtain the product (5.7 g, 98%). M. S.: (calcd.) ¹H NMR (CDCl₃) δ: 8.26 (d, J=8.4Hz, 1H), 8.20 (s, 1H), 7.78 (m, 2H), 7.41(m, 3H), 2.02(t, J=8.3Hz, 4H), 1.14-0.95(m, 12H), 0.75 (t, J=7.0Hz, 6H), 0.57 (m, 4H).

9,9-Dihexyl-2-amino-9H-fluorene (FL-NH₂)

FL-NO₂ (497 mg, 1.3 mmol) was dissolved in 30 ml ethanol. Palladium (finely divided on carbon, 116 mg) was added and the mixture was put under 50 atmospheres H₂ for 12 hours. The catalyst was removed via a Celite plug and the ethanol was removed under reduced pressure to afford the product in quantitative yield. M. S.: (calcd.) ¹H NMR (CDCl₃) δ: 7.54 (d, J=7.3,

1H), 7.47 (d, J=6.6, 1H), 7.27(m, 2H), 7.19(d, J=8.0, 1H), 6.71(m, 2H), 3.87(br s, 2H), 1.88(m, 4H), 1.14-0.96(m, 12H), 0.76(t, J=7.1, 6H), 0.62(m, 4H).

***N*-(octyl)-*N*-(9,9-dihexyl-9H-bifluoren-2-yl)-(3',5'-di-*t*-butylphenoxy)perylene-3,4:9,10-bis(dicarboximide) (FL-PDI)**

FL-NH2 (168 mg, 0.48 mmol), and **PIA** (44 mg, 0.048 mmol) were combined in 10 ml of DMF and N₂ was bubbled through the mixture for 20 minutes. Zinc acetate (~2 mg, 0.014 mmol) was added and the reaction was refluxed for 24 hours. After the solvent was removed by rotary evaporation, column chromatography in 7:3 dichloromethane/hexanes yielded **FL-PDI** (20 mg, 33%). M. S.: 1253.9 (calcd. 1242.74) ¹H NMR (CDCl₃) δ: 9.74(d+d, 2H), 8.71(d, J=8.5Hz, 1H), 8.67(d, J=8.4Hz, 1H), 7.82(d, J=7.7Hz, 1H), 7.72(m, 2H), 7.53(m, 2H), 7.35(m, 4H), 7.05(s, 4H), 4.16(t, J=7.1Hz, 2H), 2.33(m, 6H), 1.95(m, 3H), 1.37-1.22(m, 58H), 0.89(m, 6H), 0.75(m, 4H).

2-Bromo-9,9-dihexyl-9H-fluorene (Br-FL)

2-Bromofluorene (1.25 g, 5.1 mmol), n-bromohexane (1.9 ml, 13.7 mmol), potassium hydroxide (1.25 g, 22 mmol) and potassium iodide (70 mg, 0.4 mmol) were combined in 150 ml of acetonitrile and heated at 60°C for 24 hours. The solvent was then removed by rotary evaporation, and the residue was dissolved in chloroform, washed with water, dilute acetic acid, then twice more with water and dried over magnesium sulfate. Column chromatography in hexanes yielded **Br-FL** (1.3 g, 60%). M. S.: (calcd. 412.18) ¹H NMR (CDCl₃) δ:7.66 (m, 1H), 7.55(m, 1H), 7.44(m, 2H), 7.32(m, 3H), 1.93(t, J=8.0Hz, 4H), 1.15-0.98 (m, 12H), 0.77(m, 6H), 0.59(m, 4H).

2-(9,9-Dihexyl-9H-fluoren-2-yl)-4,4,5,5-tetramethyl-[1,3,2]dioxaborolane (FL-BE)

FL-Br (0.72 g, 1.7 mmol), 4,4,5,5,4',4',5',5'-octamethyl-[2,2']bi[[1,3,2]dioxaborolanyl] (680 mg, 2.57 mmol), and potassium acetate (750 mg, 7.7 mmol) was dissolved in 15 ml of DMSO and sparged with N₂ for 20 minutes. 1,1'-bis(diphenylphosphino)ferrocene dichloropalladium(II) (complex with dichloromethane, 180 mg, 0.225 mmol) was then added along with extra 1,1'-bis(diphenylphosphino)ferrocene (45 mg, 0.075 mmol) and the reaction was heated under N₂ at 90°C for 24 hours. The solvent was removed under reduced pressure and column chromatography with a 3:2 chloroform/hexanes mobile phase yielded the product, FL-BE (600 mg, 75%). M. S.: 460.90 (calcd. 460.35) ¹H NMR (CDCl₃) δ: 7.81 (d, J=7.5Hz, 1H), 7.72(m, 3H), 7.32(m, 3H), 1.98 (m, 4H), 1.39(s, 12H), 1.12-0.97(m, 12H), 0.72(t, J=7.2Hz, 6H), 0.58(m, 4H).

***N*-(octyl)-*N*-(9,9,9',9'-tetrahexyl-9H,9'H-[2,2']bifluorenyl)-(3',5'-di-*t*-butylphenoxy)perylene-3,4:9,10-bis(dicarboximide) (FL₂-PDI)**

FL-BE (137 mg, 0.30 mmol) and Br-FL-PDI (45 mg, 0.034 mmol) were combined in 10 ml of dioxane with several drops of water and potassium carbonate (41 mg, 0.30 mmol) and sparged for 20 minutes. Tetrakis(triphenylphosphine)palladium(0) (5 mg, 0.004 mmol), was then added and the reaction was heated under N₂ at 90°C for 24 hours. The solvent was removed by rotary evaporation. Column chromatography with a 7:3 chloroform/hexanes mixture yielded FL₂-PDI (23 mg, 43%). M. S.: 1575.97 (calcd. 1574.99) ¹H NMR (CDCl₃) δ: 9.75 (d + d, 2H), 8.72 (d, J=8.3 Hz, 1H), 8.68 (d, J=8.3 Hz, 1H), 7.87(s, 1H), 7.82(s, 1H), 7.79(d, J=7.9Hz, 1H), 7.74(d, J=7.0Hz, 1H) 7.68-7.60(m, 5H), 7.39-7.27(m, 7H), 7.06(m, 4H), 4.17(t, J= 7.7Hz, 2H), 2.03(m, 10H), 1.74(m, 3H), 1.38-1.05(m, 70H), 0.78(t, J=6.9Hz, 12H), 0.51(m, 8H).

7-Bromo-9,9,9',9'-tetrahexyl-9H,9'H-[2,2']bifluorenyl (Br-FL-FL)

Br-FL-Br (5.1 g, 10.4 mmol) and **FL-BE** (1.6 g, 2.94 mmol) were combined in 90 ml of dioxane with several drops of water and potassium carbonate (406 mg, 2.94 mmol) and sparged for 20 minutes. Tetrakis(triphenylphosphine)palladium(0) (10 mg, 0.008 mmol), was then added and the reaction was heated under N₂ at 90°C for 24 hours. The solvent was removed by rotary evaporation. Column chromatography with a 1:9 chloroform/hexanes mixture yielded **Br-FL-FL** (822 mg, 37%). M. S.: 744.44 (calcd. 744.43) ¹H NMR (CDCl₃) δ: 7.78(m, 3H), 7.72-7.59(m, 5H), 7.50(m, 2H), 7.37(m, 3H), 2.04(m, 8H), 1.19-1.03 (m, 24H) 0.79(m, 12H), 0.73(m, 8H).

4,4,5,5-Tetramethyl-2-(9,9,9',9'-tetrahexyl-9H,9'H-[2,2']bifluorenyl-7-yl)-[1,3,2]dioxaborolane (BE-FL-FL)

Br-FL-FL (820 mg, 1.1 mmol), 4,4,5,5,4',4',5',5'-Octamethyl-[2,2']bi[[1,3,2]dioxaborolanyl] (571 mg, 2.2 mmol), and potassium acetate (641 mg, 6.5 mmol) were added to 15 ml of DMSO and N₂ was bubbled through the mixture for 20 minutes. 1,1' bis(diphenylphosphino)ferrocene dichloropalladium(II) (complex with dichloromethane, 49 mg, 0.06 mmol) was then added along with extra 1,1' bis(diphenylphosphino)ferrocene (35 mg, 0.06mmol) and the reaction was heated under N₂ at 95°C for 24 hours. The solvent was removed by rotary evaporation and column chromatography in 1:1 hexanes/chloroform yielded **BE-FL-FL** (121 mg, 14%). M. S.: 792.82 (calcd. 792.60) ¹H NMR (CDCl₃) δ: 7.77-7.64(m, 6H), 7.56(m, 4H), 7.27(m, 3H), 1.97(m, 8H), 1.06-0.94 (m, 24H), 0.62(m, 12H), 0.62(m, 8H).

N-(octyl)-N-(9,9,9',9',9'',9''-hexahexyl-9H,9'H,9''H-[2,2',2'']terfluorenyl)-(3',5'-di-*t*-butylphenoxy)perylene-3,4:9,10-bis(dicarboximide) (FL₃-PDI)

FL₂-BE (120 mg, 0.15 mmol) and **Br-FL-PDI** (50 mg, 0.04 mmol) were combined in 10 ml of dioxane with several drops of water and potassium carbonate (21 mg, 0.15 mmol) and sparged for 20 minutes. Tetrakis(triphenylphosphine)palladium(0) (5 mg, 0.004 mmol), was then added and the reaction was heated under N₂ at 90°C for 24 hours. The solvent was removed by rotary evaporation. Column chromatography with a 7:3 chloroform/hexanes mixture yielded **FL₃-PDI** (46 mg, 60%). M. S.: 1908.16 (calcd. 1907.24) ¹H NMR (CDCl₃) δ: 9.75 (d + d, 2H), 8.72 (d, J=8.3 Hz, 1H), 8.68 (d, J=8.3 Hz, 1H), 8.43 (s, 1H), 8.40(s, 1H), 7.88(d, J=8.0Hz, 1H), 7.83(m, 3H), 7.79(d, J=7.8Hz, 1H), 7.75(d, J=7.1Hz, 1H), 7.68-7.63 (m, 4H), 7.39-7.28(m, 9H), 7.06(m, 4H), 4.17 (t, J=7.6Hz, 2H), 2.15-1.98 (m, 14H), 1.74(m, 3H), 1.38-1.04(m, 82H), 0.77 (m, 30H).

Chapter 3 Temperature Dependence of Charge Separation Through
Fluorene Oligomers: An Ideal System for Studying Charge Transfer
Mechanisms

3.1 Introduction

The nature of how charge is propagated through molecular materials is at the heart of molecular electronics^{3, 95} as well as being of fundamental importance in the design of organic photovoltaic devices and light emitting diodes⁹⁶⁻⁹⁸ and understanding the mechanism of the photosynthetic reaction center.^{4, 99} Intrinsically, such charge transfer processes challenge our understanding of fundamental charge dynamics in molecular systems and numerous investigations spanning many decades have examined this question, frequently using two redox centers covalently bound to the bridge group that is under study. These bridge groups can be generally classified into three categories, σ -systems,^{21, 100} linear π -systems^{55, 56, 101-103} and cofacial π -systems, of which DNA is the most heavily studied.¹⁰⁴ Due to their smaller HOMO-LUMO gaps and consequently more energetically accessible orbitals, π -systems have shown the greatest potential for long distance charge transfer. This trend is consistent with McConnell's relation,²⁰

$$V_{eff} = \frac{V_{D1}V_{NA}}{E_1 - E_{D/A}} \prod_{i=1}^N \frac{V_{i,i+1}}{E_{i+1} - E_{D/A}} \quad (3.1)$$

where V_{ij} are matrix elements between different sites (D, donor, A, acceptor), E_i is the energy of a particular site, and N is the number of bridge sites, which shows the importance of energetic resonance conditions. McConnell's relation also suggests an exponential decay of the charge transfer rate, k_{CT} , as a function of distance between the redox centers.²¹ A parameter, β , is typically used to describe that decay

$$k_{CT} = Ce^{-\beta r} \quad (3.2)$$

where r is the redox center/redox center distance and has been the object of many experimental and theoretical studies.^{21, 95} However, McConnell's relation is a perturbative expression and fails for small energy gaps. In this regime the bridge orbitals are expected to take on a more active role in the transfer process than simply acting as virtual states in a superexchange type reaction. Actual occupation of bridge sites and transfer among them, giving thermally activated hopping transport, is characterized by a much weaker distance dependence and can provide efficient long distance charge transfer.⁵¹

The conditions for transition between superexchange and hopping transport have been of particular theoretical^{22, 23, 26, 105, 106} and experimental interest.^{55, 56, 101, 107} Typically, one increases the number of repeat units of an oligomeric bridge to evaluate the distance dependence of k_{CT} . However, this approach has been repeatedly complicated by other system parameters that change as a function of bridge length, including bridge oxidation (or reduction) potential^{55, 56} and conformational stability. The latter issue has been particularly evident in the temperature dependence of k_{CT} in linear π -systems which frequently demonstrated negative activation energies.^{101, 108} This complex temperature dependence suggests the existence of additional rate processes that may occlude an analysis of the transition from superexchange to hopping.

In the last chapter, we detailed the use of an oligomeric fluorene bridge as a means to avoid large changes in bridge oxidation potential as a function of bridge length because the oligomers exhibit relatively static oxidation potentials.^{48, 101, 109} In this chapter we add to that study by presenting the temperature dependence of k_{CT} , and show that these molecules exhibit temperature dependence that is well described by the semi-classical Marcus equation. As a consequence of their thermal and energetic uniformity, they are ideal candidates for exploring the transition from superexchange to incoherent hopping. We will then show that their observed

3.2 Results and Discussion

3.2.1 Variable Temperature Transient Absorption

The oligomers were prepared with a phenothiazine (PTZ) hole acceptor and a perylenediimide (PDI) hole donor, Figure 9. Selective photoexcitation of the PDI component at 532 nm with 150 fs pulses produces the locally excited state, $^1\text{PDI}^*$ (broad absorption at 715 nm), which dominates the transient absorption spectra at early times, Figure 10. Intramolecular charge transfer produces the distal radical ion pair, $\text{PDI}^{\bullet-}\text{-FL}_n\text{-PTZ}^{\bullet+}$. Formation of the charge transferred state can be monitored by the quenching of $^1\text{PDI}^*$ which can be inferred from decay of the excited state absorption feature or decay of the stimulated emission feature (610 nm).

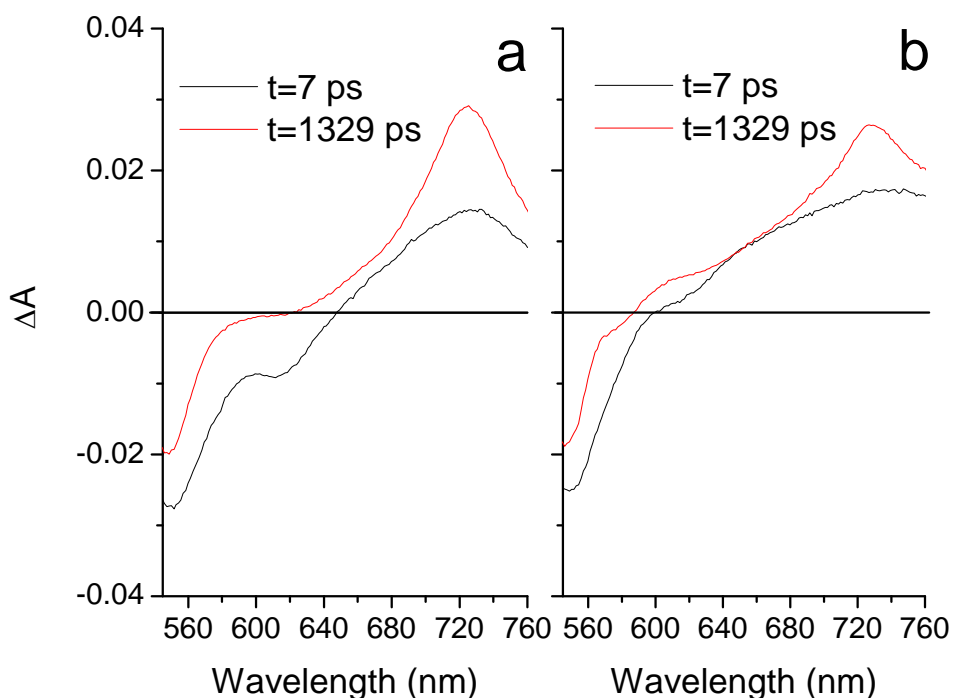


Figure 10 Transient absorption spectra of 1 in toluene with 532 nm excitation at A) 300 K and B) 210 K

Charge transfer can also be monitored directly as the transient absorption of the anion, PDI⁻, which appears as a sharper feature (725 nm) overlapping with the more broad transient absorption of PDI^{1*}, Figure 10A.

Transient absorption studies were conducted on **1-3** in toluene over a range of temperatures. Charge separation kinetics were taken at 725 nm (absorption of PDI⁻). For **1** and **2**, all observed kinetics were monoexponential. For **3**, kinetics consistently showed a small fast (4-13%, 50 ps) component. For our analysis, this component was kept constant for all temperatures. The rate, k_{CT} , is seen to decrease monotonically with temperature over the range studied. To analyze the temperature dependences of the rates we use the semi-classical Marcus equation¹¹⁷ in the non-adiabatic limit,¹⁵

$$k_{CS} = \frac{2\pi}{\hbar} V_{ij}^2 \sqrt{\frac{1}{4\pi\lambda_0 k_B T}} \exp\left(\frac{-\Delta G^\ddagger}{k_B T}\right) \quad (3.3)$$

where $\Delta G^\ddagger = \frac{(\lambda + \Delta G)^2}{4\pi\lambda}$. Use of Equation 3.3 in the adiabatic limit (no T dependence in prefactor) yields a marginally worse fit. Employing a functional form of Equation 1, $k_{CT} = AT^{-1/2} \exp(-E_a/kT)$, we plot $1/T$ versus $k_{CT}T^{1/2}$ on a natural logarithm scaled plot for **1-3** in Figure 3. Crucial parameters can be easily extracted from the slope and intercept, are summarized in Table 3, and are further discussed below.

3.2.2 Aggregation

Our accessible temperature range for **2** and **3** is limited by two factors: charge transfer yield and inhomogeneous broadening of the anion spectral feature. The decline in yield is consistent with a temperature independent fluorescence lifetime of unsubstituted PDI of 4.4 ns:

as temperature is dropped, k_{CT} slows and becomes comparable with the fluorescence lifetime, and the correspondingly lower yield of anion becomes more difficult to resolve from the broad overlapping 1PDI transient absorption. However, this reduction of yield alone cannot account for the broadening of the anion feature, Figure 10B. Additionally, the stimulated emission feature is also significantly reduced at lower temperatures, Figure 10B.

Steady-state absorption in the same range of temperatures, Figure 12, shows significant changes from the room temperature spectra. These changes are a result of the exciton coupling¹¹⁸ that accompanies aggregation, and have been seen before in many other PDI-derivatives.^{98, 119} The loss of the stimulated emission is also consistent with aggregation-

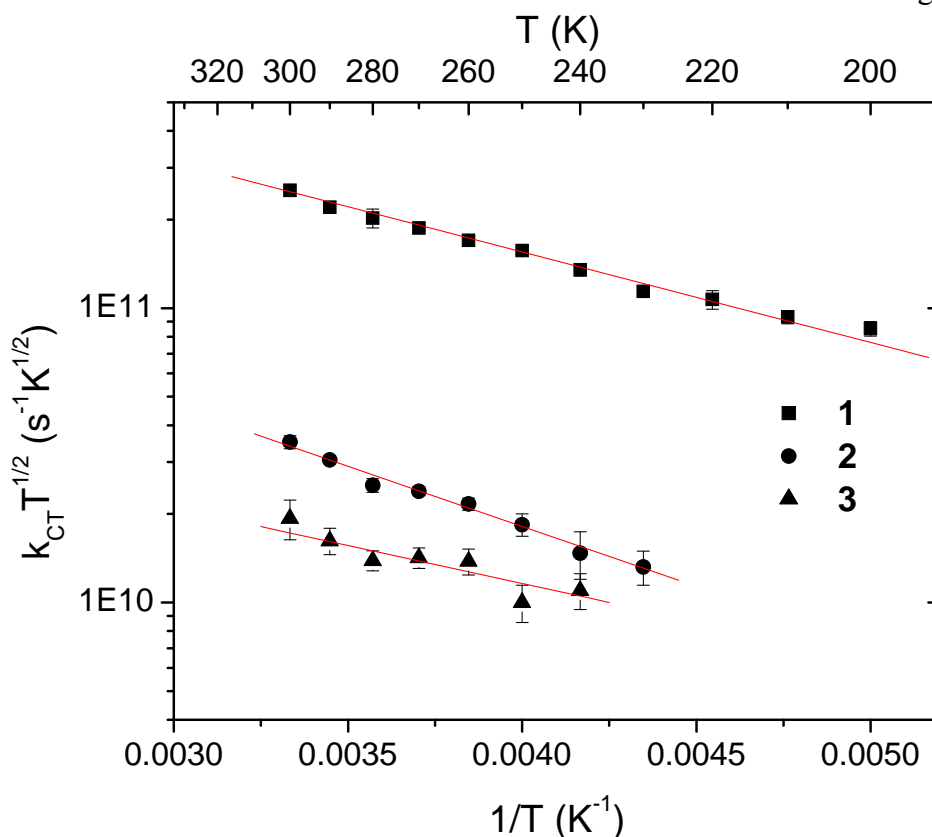


Figure 11 Semilogarithmic plot of $k_{CT}T^{1/2}$ vs $1/T$ for 1-3 and linear fits

induced exciton coupling: excitation into the higher exciton level is symmetry allowed, but rapid internal conversion to the lower exciton level results in the excitation residing in a state that is

symmetry forbidden from radiatively decaying back to the ground state in the absence of significant vibronic coupling. The aggregation also broadens the anion transient absorption feature,¹¹⁹ likely as a result of multiple similar conformations (inhomogeneous broadening), making the anion more difficult to resolve from excited state absorption. Interestingly, k_{CT} shows no deviation from linearity even through the onset of aggregation. This insensitivity to aggregation was also seen previously,¹¹⁹ and likely stems from the effect of a lower excited state

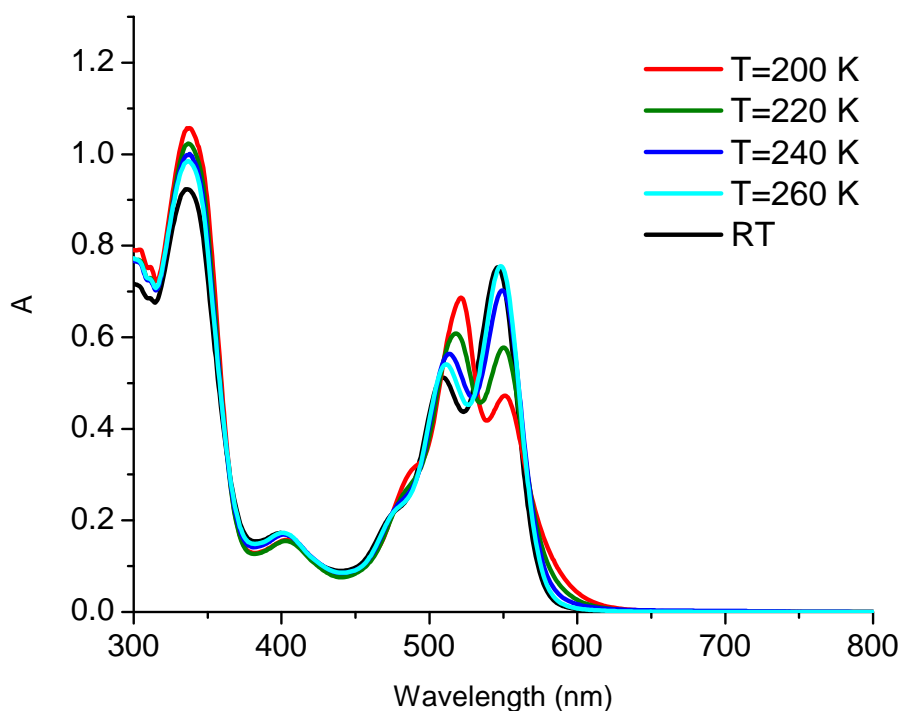


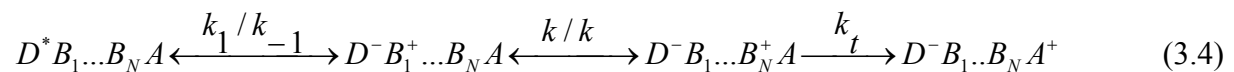
Figure 12 Steady-state UV-vis absorption of 2 in toluene over a range of temperatures showing evidence of exciton coupling

energy, because of the rapid conversion to the lower exciton state, being compensated for by a lower ion pair energy, because of the additional stabilization in the aggregate.

3.2.3 Rate Analysis

Examination of Figure 11 shows k_{CT} to be well described by Equation 3.3 over the region studied. This behavior is in stark contrast with highly non-monotonic behavior observed in similar systems,^{101, 108} in some cases over a comparable temperature range. While the broadening mentioned above results in only a limited range of temperatures being accessible, more than enough temperature points are available to allow determination of the parameters of Equation 3.3 in the vicinity of room temperature, which are summarized in Table 1, and to establish behavior at room temperature as being activated.

Possessing more information about the temperature dependence of k_{CT} , we can reinterpret the length dependence of k_{CT} , presented in Figure 5A.¹⁰¹ The energetic barrier to charge carrier bridge occupation has been calculated to be approximately 0.1-0.2 eV¹⁰¹ using Weller's estimation of the energy of a pair of charges embedded in a dielectric continuum.¹³ This value is very close to the value of 0.2 eV reported^{123, 124} for bridge occupation in DNA A-tracks¹²⁵ of the form, GA_n . Bixon and Jortner¹⁰⁵ have analyzed thermally induced hopping transport in A-tracks produced by Giese and coworkers,¹⁰⁷ using a classical kinetic model,



where k_1 and k_{-1} refer to the rates of the charge carrier shifting on and off of the bridge from the hole donor, k is the rate of hopping between bridge sites, and k_t is the rate of the hole shifting onto the final hole acceptor. This last process is assumed to be irreversible due to fast relaxation

in the dense vibronic quasicontinuum of the lower energy final hole acceptor.¹⁴ The classical form of 3.4 is used instead of a quantum mechanical expression because of the rapid dephasing that occurs at each individual bridge site, a consequence of the finite and non-vanishing amount of time the charge resides on each bridge²⁵ and coupling to each bridge's own vibronic density of states.²⁴ Bixon and Jortner's expression for the rate of accumulation of charge at the final acceptor is

$$k_{CT}(N) = \left(\frac{kk_t + kk_{-1} + (N-1)k_{-1}k_t}{kk_1k_t} + \frac{N}{k_t} + \frac{N(N-1)}{2k} \right)^{-1} \quad (3.5)$$

where N is the number of bridge sites.

When analyzed in the limit of $k_t \gg k_{-1}, k \gg k_1$ (slow population of the bridge, fast transfer to the hole acceptor), one gets

$$k_{CT}(N) = \frac{C'}{1 + \frac{k_1}{k - k_{-1}} N} \quad (3.6)$$

Where $C' = k_1 / (1 - k_{-1} / k)$. However, large scale motions required of the PTZ suggest that shift of the carrier onto the hole acceptor, k_t , may be rate limiting. In addition, the equilibrium angle between two fluorene units is considerably less than the angles between a fluorene unit and a hole donor or acceptor.¹⁰¹ Consequently, a more accurate limit may be $k \gg k_{-1}, k_t, k_1$, in which case the expression reduces to

$$k_{CT}(N) = \frac{C''}{1 + \frac{k_1}{k_{-1} + k_t} N} \quad (3.7)$$

Where $C'' = k_1 k_t / (k_t + k_{-1})$. Both of these forms are very similar to forms derived by Segal, Nitzan, and coworkers,¹⁰⁶ who also predicted a $1/(a+bN)$ form. However, all of these expressions appear very different from the monoexponential form of Equation 3.2. But in the limit of small β , Equation 3.2 can be Taylor expanded to low order and approximated as

$$k_{CT} = Ce^{-\beta r} \approx \frac{C}{1 + \beta r} = \frac{C}{1 + \beta a N} \quad (3.8)$$

where a is the length of a bridge monomer in Å.

Depending on the relative rates in Equation 3.8 as well as the specifics of the system, charge carrier occupation of the bridge can be directly probed spectroscopically¹²⁶ or implied by a delay between the appearance of one ionized redox center and the other.¹²⁷ However, in the absence of these signatures, the relation in Equation 3.8 shows that distance dependence alone is *insufficient* to distinguish between superexchange and thermally activated hopping because both mechanisms show such similar distance dependencies in the slowly-decaying regime. The very small β values that are measured in some cases (in this case 0.09 \AA^{-1}) and the necessarily small energy gaps that are required in these cases strongly imply that transfer is being dominated by thermally activated hopping. Analysis of the distance dependence using Equations 3.6 or 3.7 yields a β value of 0.06 \AA^{-1} , very similar to the value of 0.09 \AA^{-1} using Equation 3.2.

3.3 Conclusion

In summary, we have presented the temperature dependence of charge separation, k_{CT} , in fluorenes oligomers covalently bound to a hole donor and hole acceptor. This temperature dependence was well described by the semi-classical Marcus equation in the non-adiabatic limit and showed positive activation energies. This simple description as well as static redox

potentials make fluorene oligomers an ideal system to explore the shift in mechanism from superexchange to hopping. Analysis based on Bixon and Jortner's kinetic model is in agreement with the soft exponential distance dependence that is experimentally observed. Further analysis of this model suggests that distance alone cannot distinguish between superexchange and hopping, although small energy gaps strongly imply the latter.

Acknowledgements: Orlando DeLeon (synthesis), Daniel Finkelstein-Shapiro (cryostat), Dongho Kim, Yuri Berlin, and Joshua Vura-Weis (helpful conversations)

Chapter 4 Scaling Laws for Charge Transfer in Multiply Bridged
Donor/Acceptor Molecules in a Dissipative Environment

4.1 Introduction

The search for vectorial charge and excitation transfer in molecules and nanostructures is motivated by advances in the design of molecular electronic and photonic devices,³ insights into the microscopic processes in photovoltaics,¹ and furthering our understanding of photosynthesis.⁴ Studies in this last category have shown that multiple spatial pathways may contribute to the overall charge and exciton transfer rates.^{6, 37-39} The explanation of observed experimental rates advanced in some of these studies demands that coherences exist among different and not necessarily proximal spatial pathways. However, the nature of the environment surrounding these paths will determine whether those coherences can survive.^{47, 50} Consequently, rules governing the additivity of multiple spatial pathways for charge and exciton transfer, rules that include a dissipative environment, must be addressed. Beyond charge and exciton transfer in proteins, conductance measurements on self-assembled monolayers of molecules implicitly involve measurements on many molecules simultaneously, and any kind of extrapolation regarding the behavior of a single molecule must be made very carefully. Conductance measurements on molecules in mechanically produced break junctions often result in integer multiples of some unit of molecular conductance,¹²⁸ implying additive contributions from multiple molecules.

Several theoretical efforts have examined the additivity of multiple spatial molecular conduction channels. Lang and Avouris,¹²⁹ and Yaliraki and Ratner³¹ concentrated on “crosstalk” interactions between contributing molecules while Larsson,¹³⁰ and Magoga and Joachim¹³¹ looked at scaling laws for transport through multiple equivalent spatial pathways. Magoga and Joachim predicted that as the number of spatially distinct pathways (N) increased,

the conductance should increase either linearly or quadratically (with N), depending on the system connectivity. If the molecules were each individually connected to the leads, the linear law would apply, whereas if the molecules were connected by some molecular node before connecting to the lead, the quadratic law would apply. Several efforts in a number of different experimental test beds have demonstrated a linear dependence, although some deviations appeared with large N .^{128, 132, 133}

All of these theoretical studies investigated the coherent limit. However, the environment is known to cause the system to lose coherence,^{47, 50} and previous studies have shown that interference can be significantly affected by a dissipative environment.^{57, 134, 135} When applied to transport in Donor-Bridge-Acceptor (D-B-A) molecules, the inclusion of dephasing enables the operation of a new and qualitatively different transport regime: the incoherent or hopping transport mechanism. Calculations predicted different length dependencies for the purely coherent superexchange mechanism and the incoherent mechanism,^{22, 26, 106, 136} predictions that were later borne out experimentally.^{55, 56, 101, 137} The aim of this report is to make similar predictions about the dependence on N of superexchange and incoherent transport, and to explore more generally how decoherence affects the role of multiple spatial pathways in charge transfer in D-B-A molecules.

4.2 Method

Our calculation utilizes a simple and purely electronic¹³⁸ tight-binding Hamiltonian which completely defines the system connectivity. D and A sites are taken to be

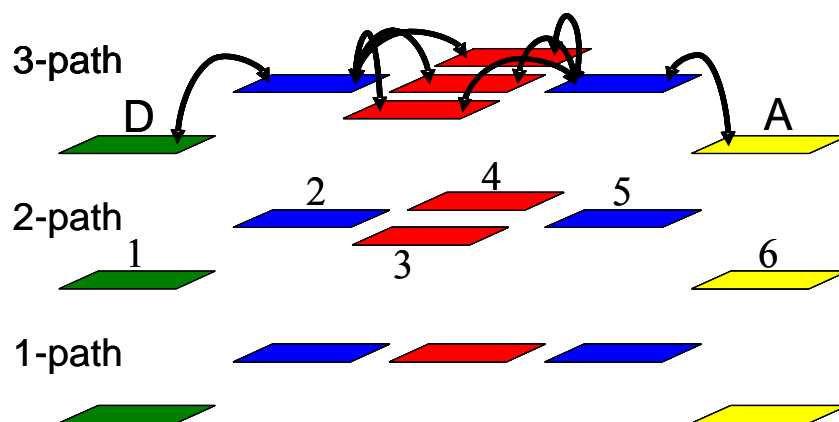


Figure 13 Connectivities of multiple spatial pathway Donor-Bridge-Acceptor systems. The red (bridge) and blue (node) sites are energetically degenerate. The numbers denote the sites.

degenerate and define the zero energy level of the system. All bridge sites are taken to be ω above the D and A sites in energy. All couplings are of magnitude V . Following the approach of Bixon and Jortner, an absorbing boundary condition (an energy width of magnitude κ , with $\kappa \sim 1/T_1$) simulates the final deposition of a charge carrier within the vibrational manifold of the A site causing irreversible, as opposed to oscillatory, charge transfer.¹³⁹

Equations of motion (EOM) are expressed using the density matrix formalism with dynamics determined by the quantum-Liouville equation.

$$\dot{\rho} = \frac{-i}{\hbar}[H, \rho] + L_D \rho \quad (4.1)$$

Solution of the dynamics constitutes an initial value problem (IVP), with the initial condition simply being all carrier population beginning on the D site (representing photoexcitation). The IVP can be solved, albeit with some difficulty, via spectral decomposition. An alternate method

of solution entails forcing the system to reach a non-trivial steady state (SS) followed by relating the flux through the system at this SS to the rate from the IVP.¹⁵ More specifically, the terms describing the dynamics of the D site are modified so that the population remains constant. This constant population keeps the system from reaching a trivial SS by replenishing population lost via the absorbing boundary condition. There are two ways of executing this modification:¹³⁶ one method (termed “constant population”) involves modifying only the EOM of the diagonal elements of the density matrix (ρ) while the other (termed “constant amplitude and phase”) also involves modification of the EOM of the coherences associated with the D site. We want to emphasize that our use of this forced SS method is to simplify solving our IVP, and so the latter method is chosen because of better agreement with the solution of the IVP. Conditions for agreement between the SS and IVP methods have been addressed previously¹⁰⁶ and will be further discussed below. Related approaches have been used previously to look at charge transfer rates in D-B-A systems,^{26, 106, 136} most recently in multiple spatial pathway systems¹³⁵ and dendrimers.¹⁴⁰ All EOM are given in the final section of this chapter.

Pure dephasing is added to the calculation by modulation of the EOM for the coherences in the density matrix linking the various sites. We use the term “pure dephasing” to include any elastic process that destroys phase relationships within the wavefunction of the charge carrier as it passes through the sites of the system without directly affecting the populations.^{48,47} When applied to an ensemble of molecules, signals that rely on a coherent sum from members of the ensemble decay, often exponentially, with some characteristic time constant, called T_2 in magnetic resonance literature. However, the concept can also be applied to just a single member of an ensemble where the density matrix, instead of providing statistical information about the ensemble, reflects uncertainty in our knowledge about the state. We include pure dephasing by

adding to the EOM for the coherences, $\rho_{ij, i \neq j}$, a decay term first order in ρ_{ij} with rate constant γ , where essentially, $\gamma=1/T_2^*$. It is then apparent that dephasing over time converts the pure state (with maximum coherence $\rho_{ij} = \sqrt{|\rho_{ii}\rho_{jj}|}$) to a statistical mixture of diabatic states (with vanishing coherence). This form of dephasing, affecting only the off-diagonal elements of ρ , arises from fluctuations in the energy levels of the diabatic states, and is caused by shifts in the diagonal elements of the Hamiltonian. Skinner and Hsu have derived the first order rate process form of pure dephasing using both quantum mechanical and stochastic formulations.⁵⁰ For a D-B-A molecule in solution, vibrational interaction with the solution bath and intramolecular vibrations will likely be the dominant contributions. Ignoring small fluctuations in the off-diagonal elements of the Hamiltonian is valid in the weak electronic coupling regime.⁴⁶ The value of γ ($1/T_2^*$) and its temperature dependence will depend on vibrational coupling⁵⁰ as well as the spectral density of the bath.^{46, 49} Assumption of a Markovian bath with vanishing correlation time yields the familiar Redfield picture.¹⁴¹ EOM of the off diagonal elements of ρ have contributions from both pure dephasing and relaxation, consistent with the Bloch relation,

$$\frac{1}{T_2} = \frac{1}{T_2^*} + \frac{1}{2T_1} \quad (4.2)$$

In our model the diabatic states are part of an electronic site basis. Consequently, dephasing results in a loss of the wavefunction's ability to spread over multiple sites, and localization ensues. Pure electronic dephasing rates of chromophores have been reported over a range of values, with coherence lifetimes $T_2^* \gg 10$ ps ($\gamma \ll 3$ cm⁻¹) at liquid helium temperatures, and $T_2^* < 0.1$ ps ($\gamma > 300$ cm⁻¹) projected for chromophores in solution at room temperature.⁵¹ The rates are measured using spectral hole burning, photon echo or resonance

Raman techniques amongst others.⁵³ More recently, two color photo echo techniques have explored the dephasing time between non- degenerate chromophores and even suggested that a protein sheath might play a role in preserving coherences.^{52, 142} The many solution studies of chromophores show electronic dephasing times loosely clustered in the range given above,⁵³ suggesting these are good values for a “typical” chromophore, although future two color experiments are necessary and should show the inter-chromophore dephasing rate to be sensitive to the vibronic coupling between chromophores and solvent and the solvent’s vibrational spectral density.^{51, 53, 54, 143, 144} The lifetime of the coherence between a fully occupied state and a weakly occupied state (although not yet a virtual state, which would have no dephasing based on Büttiker-Landauer tunneling time arguments²⁵) is a more subtle issue and is currently under theoretical investigation. Rational modulation of the electronic dephasing time could possibly be effected by altering the magnitude of solvent induced energetic fluctuations and correlation times which could be accomplished by varying solvent dipole moment, viscosity, and temperature.

The concept of a participation ratio (PR) has been introduced¹⁴⁵ to give a measure of the delocalization of the wavefunction and recently applied^{146, 147} in the context of electron transfer. Mukamel and coworkers^{148, 149} have adapted the PR concept for the density matrix and used it as a measure of the coherence length. They define two quantities, the population participation ratio (PPR)

$$PPR = \left(\sum_n \rho_{nn}^2 \right)^{-1} \quad (4.3)$$

and the coherence participation ratio (CPR)

$$CPR = \frac{\left(\sum_{mn} |\rho_{mn}| \right)^2}{PPR \cdot \sum_{mn} |\rho_{mn}|^2} \quad (4.4)$$

The PPR ranges from 1 to N and gives a measure of the number of sites at which the charge carrier is likely to be found. The CPR reflects the strength of the phase relationships between those sites and is indicative of delocalization.

4.3 Results

4.3.1 Rate Ratios

We begin by examining the system geometries shown in Figure 13, in the coherent limit. In the highly non-resonant regime, with $\omega \gg V, \kappa$ (variables defined in the above text), we determined the analytical solutions for the rate constant of ET to take the form

$$k_{ET} = \frac{4N^2V^2}{\kappa} \left(\frac{V}{\omega} \right)^{2L} \quad (4.5)$$

where the charge transfer rate constant is seen to vary as the square of the number of pathways (N). The rate expression's dependence on L, the number of linear bridge units, has been discussed previously.²⁶

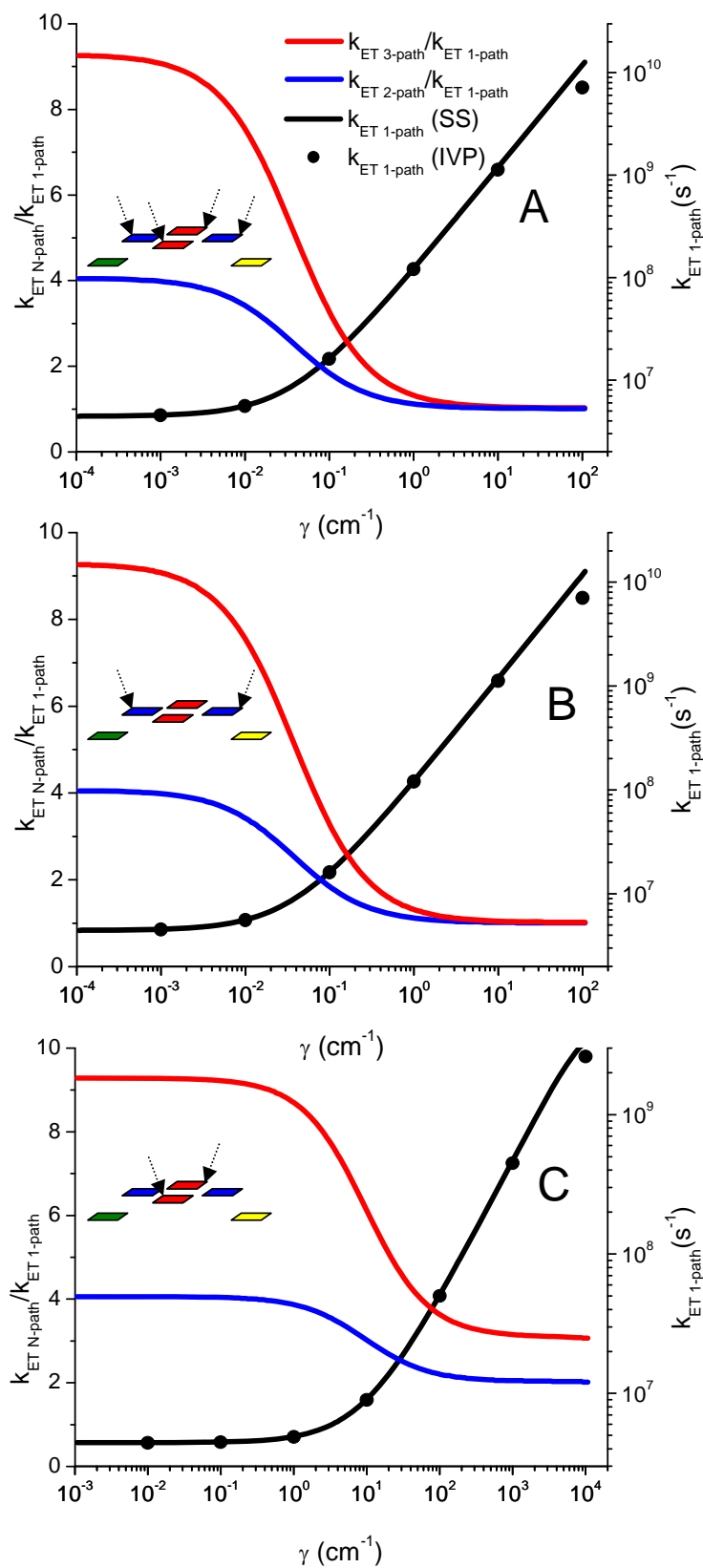


Figure 14 Rate ratios for the 2 (blue line) and 3 (red line) path systems, absolute rate for the 1 path system (black line) calculated with the enforced SS, and comparison with that rate calculated as an IVP (black circle). The above values were calculated for increasing dephasing on the red and blue sites (A), just the blue sites (B), and just the red sites (C).

Magoga and Joachim¹³¹ have predicted this quadratic dependence (on N) for systems that converge to single molecular nodes before coupling to the band structure of an electrode.

The calculated ratio of the rates for the N -pathway system to the single pathway system is plotted in Figure 14. The value of ω , the B energy gap, of 8000 cm^{-1} (1 eV) is consistent with a small aromatic bridge, while the V coupling between sites, 500 cm^{-1} , corresponds to a typical coupling between individual phenyl rings. The decay rate from the A site, κ , is set at 400 cm^{-1} , following previous investigations.¹⁰⁶ The small deviations from the N^2 limit on the left hand side of the plots are indicative of the relatively weak but finite dephasing as well as not being completely in the highly non-resonant regime. The absolute rate for the linear system ($N=1$) is shown for comparison.

Dephasing is initially added to the EOM for all of the coherences involving B (red and blue) sites, Figure 14A. As the dephasing rate is increased, the rate ratios for the multiple pathway structures decrease and ultimately converge to unity. In contrast, the absolute rate of the linear system increases with γ (until $\gamma \approx \omega$), as shown previously.²⁶ Pure dephasing opens up an additional incoherent transport channel that quickly overwhelms the superexchange channel. This incoherent channel is seen to be independent of N , the number of pathways. Just as the shift from superexchange to incoherent transport results in a different length dependence for ET, this same shift also results in a different dependence on the number of spatial pathways.

Modulation of the system parameters leaves Figure 14 qualitatively unchanged. Decreasing ω makes the rate ratio less sensitive to γ . This is consistent with earlier work,²⁶ as a smaller energetic barrier enhances the contribution of the coherent channel to a greater extent than it enhances the incoherent channel, allowing the coherent limit of the rate ratio to survive

over a larger range of dephasing strengths. Modulation of V distorts the shape of the rate ratio curve, but the coherent and incoherent ratio limits are preserved, as long as the system remains in the highly non-resonant regime. Changing κ has minimal effect, as long as κ remains small compared to ω .

4.3.2 Initial Value Problem

To verify that the SS method returns the correct solution to the IVP, we also solved the IVP directly for several values of γ . These values are also seen in the rate ratio plots (for $N=1$) and show good agreement with the SS method. At higher values of γ the IVP rates become multiexponential and the rate calculated by the SS method may become irrelevant. As discussed by Segal, Nitzan, and coworkers,¹⁰⁶ the conditions for the system attaining a monoexponential decay (and thus agreeing with the SS method) entail the system reaching a pre-equilibrium very quickly compared to the total population decay. If the system can attain this pre-equilibrium fast enough, the multi-site system behaves essentially as a single carrier reservoir and obeys first order kinetics. This situation is similar to SS approximation behavior in simple classical chemical kinetics.

Previous studies of the influence of pure dephasing on ET have shown that the representation^{56, 130, 150} in which dephasing is introduced can significantly influence the transport behavior. In the limit of extremely fast decoherence, these different representations correspond to different environment-induced super selection (einselection) operations, resulting in different “pointer states” being available for measurement.¹⁵¹ Consequently, we varied the dephasing behavior within the site basis, dephasing on just the nodes (the blue sites in Figure 13), Figure 14B, and dephasing on just the degenerate bridge sites (the red sites in Figure 13), Figure 14C.

Dephasing on the nodes yields nearly identical behavior as dephasing on all of the B sites. However, dephasing only on the degenerate bridge sites yields qualitatively different behavior. Instead of converging to unity, the rate ratios converge to N . Magoga and Joachim¹³¹ predicted a linear dependence on N for molecular junctions where multiple molecular pathways connected with the electrode without connecting first via a molecular node, while a linear dependence was also observed in several experimental junctions whose geometry has this character.^{132, 133} This different dephasing scheme also more weakly hinders the formation of the pre-equilibrium as compared to the other two dephasing schemes. Consequently, it is possible to examine rate ratios at much higher values of γ , although values much greater than 10^2 cm^{-1} are likely unphysically large.

4.4 Discussion

4.4.1 Participation Ratios

To understand better this shift from quadratic to linear dependence we looked more closely at the pre-equilibrium. As stated before, the formation of this pre-equilibrium is necessary for the validity of the SS approximation. However, the nature of this pre-equilibrium, the values of the populations and coherences, may help us understand, mechanistically, the action of the different dephasing schemes.

In Figure 15, we plot the PPR and CPR with increasing dephasing strength for the different dephasing schemes for the $N=2$ system. The PPR (solid lines) correctly captures the gradual shift to more population existing on the B sites at higher values of γ , although most of the population still resides on the D site. When dephasing only operates on the degenerate bridge

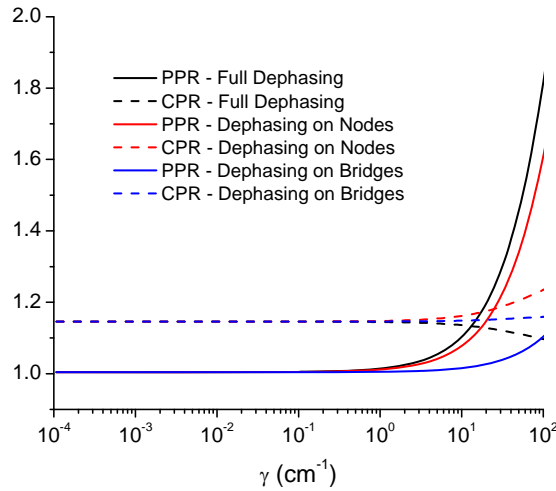


Figure 15 Participation Ratios with different dephasing schemes

sites (as in Figure 14C), less population accumulates on the B sites than other dephasing schemes at equivalent γ . Maintaining population mainly on the D site is a necessary condition for agreement between the SS and IVP methods.¹⁰⁶

4.4.2 Percent Maximal Coherence

Unfortunately, the CPR shows very little change. Because the value of the CPR is dominated by the stronger coherence values, it cannot give us information about potentially important changes in the weaker coherences. To examine these changes, we adopt a strategy related to Mukamel and coworkers' real space plotting of the density matrix.⁵¹ Rather than show the absolute values of the coherences, where even with a logarithmic scale, small changes in the weaker coherences would be difficult to see, we plot a quantity we term the "Percent Maximum Coherence (PMC)," which we define as

$$PMC_{ij} = \frac{\rho_{ij}}{\sqrt{|\rho_{ii}\rho_{jj}|}} \times 100 \quad (4.6)$$

In a pure state (ie, ρ is idempotent), the PMC will be 100 while in a statistical mixture of states, the PMC is zero. Notice that by definition, diagonal elements of the density matrix have a PMC of 100. In Figure 16, PMC's are plotted for the pre-equilibria formed for different dephasing schemes at selected dephasing strengths.

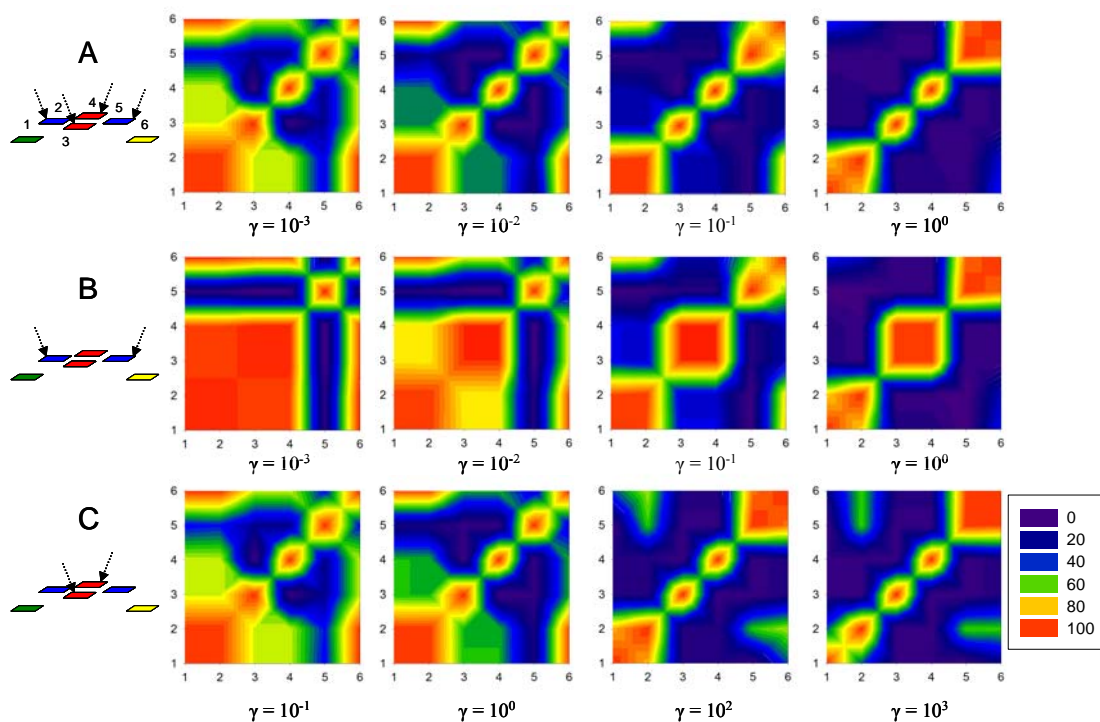


Figure 16 Plots of the Percent Maximal Coherence (PMC) of each position of the density matrix at increasing dephasing strength for three dephasing schemes: dephasing on the red and blue sites (A), the blue sites (B), and the red sites (C). The numbers on the axes denote the different sites (from Figure 13).

The PMC plots can provide information as to which Liouville space pathways¹⁵² offer the greatest contributions for transport. Positioning the decoherences on the nodes (Figure 16B) compared to the full dephasing (Figure 16A) treatment shows PMC plots that differ only in the coherences between degenerate bridge sites. However, since these two decoherence schemes

show only marginal effect on the rate ratio, these coherences likely constitute an irrelevant Liouville space pathway, as is physically reasonable.

An interesting issue is the distinction between the scenario where the newly opened incoherent channel simply dominates the transport and the scenario where the dephasing actually reduces the absolute effectiveness of the coherent, superexchange channel. One definition of superexchange defines the process as requiring passage through the ρ_{DA} or ρ_{AD} Liouville state.¹⁵² At values of $\gamma > 10^{-3}$, the incoherent channel quickly becomes dominant (as evidenced by the increased absolute rate), while only at values of $\gamma > 10^{-1}$ does the PMC of ρ_{DA} decrease in magnitude. This implies a reduction in the efficacy of superexchange at high γ , showing that both scenarios are correct: the incoherent channel quickly overshadows the coherent channel, which, already reduced in relative contribution, eventually becomes reduced in absolute contribution.

The coherence ρ_{DA} retains its high PMC over a much larger γ with dephasing applied only on the degenerate bridges. In our calculations on linear systems, we found that the impact of dephasing on a particular site was significantly enhanced by that site's proximity to the starting point of the carrier. While other explanations for dephasing contact effects have been suggested,¹⁵⁰ we feel that this condition is likely causing the weaker effects in this dephasing scheme. However, the origin of the different convergent rate ratio (Figure 14 A and B as compared to C) needs to be addressed. In all parts of Figure 16, the PMC of ρ_{DA} significantly diminishes at large dephasing strengths. On the other hand, the PMC of ρ_{25} (the coherence between the nodes, red sites, see Figure 13) retains a relatively large value even into unphysically large dephasing ranges for Figure 16C. The absence of this Liouville path in the other decoherence schemes, as evidenced by the lack of PMC at that position, implies that this

path is responsible for the different convergent rate ratio. This behavior makes sense when one looks at the subsystem made up of just the red and blue sites (a valid perspective since the coherence ρ_{DA} has already become negligible). All of the sites in this subsystem are energetically degenerate and the coherences between the red sites have been destroyed (PMC=0). Without these interference terms to cause the N^2 dependence, the two pathways will sum like classical microscopic rate processes, with $k_{tot}=N*k_{micro}$.

As mentioned above, this situation is qualitatively similar to the one discussed by Magoga and Joachim regarding the N dependence of the conductance of molecules individually wired to the electrodes. In that case also, the interference terms are destroyed, resulting in the N dependence. However, in their work it is the band structure of the electrodes that causes the critical coherences to be destroyed, while in this case, it is the environment that causes those terms' destruction.

In the coherent limit (no dephasing), the Liouville pathway connecting the D and A sites is dominant and the contributions from the multiple spatial pathways sum coherently to give the N^2 dependence, as is expected for superexchange. When we dephase on the nodes, all relevant coherences are destroyed and incoherent transport dominates. In this situation, the localized charge carrier must essentially choose a single pathway, regardless of the number of pathways available, leading to the rate ratio of unity.

4.5 Conclusion

In summary, we have examined charge transfer model systems representing D-B-A molecules with multiple spatial pathways, using a combination of enforced SS and IVP methods. After returning rate ratios that are in agreement with what others have predicted in the coherent

limit, we have shown that adding pure (or T_2^*) dephasing significantly affects the rate ratio. In addition, we observed different convergent rate ratios depending on which local decoherence scheme was applied. We examined the differences between these schemes by looking at the Percent Maximum Coherence of the different elements of the corresponding density matrix of the pre-equilibrium attained. Different decoherence schemes opened up different Liouville pathways that are responsible for the respective rate ratios. These pathways show rate ratios that vary from an N^2 dependence for full coherence, to an N dependence for dephasing only on the parallel bridge sites, to being N -independent for dephasing on the nodes.

4.6 Equations of Motion

Below are the details of our calculations. All calculations were performed with Maple 8.

EOM for $N=1$ are given below.

For Decoherence Scheme 1, Full Dephasing (on blue and red sites), $\gamma_{ij}=\gamma$ for all i,j

For Decoherence Scheme 2, Dephasing on Nodes only (on blue sites), $\gamma_{ij}=\gamma$ for i or $j=2$ or 4 , $\gamma_{ij}=0$ for all other i,j

For Decoherence Scheme 3, Dephasing on Degenerate Bridges only (on red sites), $\gamma_{ij}=\gamma$ for i or $j=3$, $\gamma_{ij}=0$ for all other i,j

$$\rho_{1,1}(t) = 1$$

$$\frac{d}{dt}\rho_{1,2}(t) = (V\rho_{1,1}(t) + \omega\rho_{1,2}(t) + V\rho_{1,3}(t))I - \frac{1}{2}\gamma_{1,2}\rho_{1,2}(t)$$

$$\frac{d}{dt}\rho_{1,3}(t) = (V\rho_{1,2}(t) + \omega\rho_{1,3}(t) + V\rho_{1,4}(t))I - \frac{1}{2}\gamma_{1,3}\rho_{1,3}(t)$$

$$\frac{d}{dt} \rho_{1,4}(t) = (V \rho_{1,3}(t) + \omega \rho_{1,4}(t) + V \rho_{1,5}(t)) I - \frac{1}{2} \gamma_{1,4} \rho_{1,4}(t)$$

$$\frac{d}{dt} \rho_{1,5}(t) = -\frac{1}{2} \kappa \rho_{1,5}(t) + V \rho_{1,4}(t) I$$

$$\frac{d}{dt} \rho_{2,1}(t) = -(V \rho_{1,1}(t) + \omega \rho_{2,1}(t) + V \rho_{3,1}(t)) I - \frac{1}{2} \gamma_{2,1} \rho_{2,1}(t)$$

$$\frac{d}{dt} \rho_{2,2}(t) = -I (V \rho_{1,2}(t) + V \rho_{3,2}(t) - V \rho_{2,1}(t) - V \rho_{2,3}(t))$$

$$\frac{d}{dt} \rho_{2,3}(t) = -(V \rho_{1,3}(t) + V \rho_{3,3}(t) - V \rho_{2,2}(t) - V \rho_{2,4}(t)) I - \gamma_{2,3} \rho_{2,3}(t)$$

$$\frac{d}{dt} \rho_{2,4}(t) = -(V \rho_{1,4}(t) + V \rho_{3,4}(t) - V \rho_{2,3}(t) - V \rho_{2,5}(t)) I - \gamma_{2,4} \rho_{2,4}(t)$$

$$\frac{d}{dt} \rho_{2,5}(t) = -\frac{1}{2} \kappa \rho_{2,5}(t) - (V \rho_{1,5}(t) + \omega \rho_{2,5}(t) + V \rho_{3,5}(t) - V \rho_{2,4}(t)) I - \frac{1}{2} \gamma_{2,5} \rho_{2,5}(t)$$

$$\frac{d}{dt} \rho_{3,1}(t) = -(V \rho_{2,1}(t) + \omega \rho_{3,1}(t) + V \rho_{4,1}(t)) I - \frac{1}{2} \gamma_{3,1} \rho_{3,1}(t)$$

$$\frac{d}{dt} \rho_{3,2}(t) = -(V \rho_{2,2}(t) + V \rho_{4,2}(t) - V \rho_{3,1}(t) - V \rho_{3,3}(t)) I - \gamma_{3,2} \rho_{3,2}(t)$$

$$\frac{d}{dt} \rho_{3,3}(t) = -I (V \rho_{2,3}(t) + V \rho_{4,3}(t) - V \rho_{3,2}(t) - V \rho_{3,4}(t))$$

$$\frac{d}{dt} \rho_{3,4}(t) = -(V \rho_{2,4}(t) + V \rho_{4,4}(t) - V \rho_{3,3}(t) - V \rho_{3,5}(t)) I - \gamma_{3,4} \rho_{3,4}(t)$$

$$\frac{d}{dt} \rho_{3,5}(t) = -\frac{1}{2} \kappa \rho_{3,5}(t) - (V \rho_{2,5}(t) + \omega \rho_{3,5}(t) + V \rho_{4,5}(t) - V \rho_{3,4}(t)) I - \frac{1}{2} \gamma_{3,5} \rho_{3,5}(t)$$

$$\frac{d}{dt} \rho_{4,1}(t) = -(V \rho_{3,1}(t) + \omega \rho_{4,1}(t) + V \rho_{5,1}(t)) I - \frac{1}{2} \gamma_{4,1} \rho_{4,1}(t)$$

$$\frac{d}{dt} \rho_{4,2}(t) = -(V \rho_{3,2}(t) + V \rho_{5,2}(t) - V \rho_{4,1}(t) - V \rho_{4,3}(t)) I - \gamma_{4,2} \rho_{4,2}(t)$$

$$\frac{d}{dt} \rho_{4,3}(t) = -(V \rho_{3,3}(t) + V \rho_{5,3}(t) - V \rho_{4,2}(t) - V \rho_{4,4}(t)) I - \gamma_{4,3} \rho_{4,3}(t)$$

$$\frac{d}{dt} \rho_{4,4}(t) = -I (V \rho_{3,4}(t) + V \rho_{5,4}(t) - V \rho_{4,3}(t) - V \rho_{4,5}(t))$$

$$\frac{d}{dt} \rho_{4,5}(t) = -\frac{1}{2} \kappa \rho_{4,5}(t) - (V \rho_{3,5}(t) + \omega \rho_{4,5}(t) + V \rho_{5,5}(t) - V \rho_{4,4}(t)) I - \frac{1}{2} \gamma_{4,5} \rho_{4,5}(t)$$

$$\frac{d}{dt} \rho_{5,1}(t) = -\frac{1}{2} \kappa \rho_{5,1}(t) - V \rho_{4,1}(t) I$$

$$\frac{d}{dt} \rho_{5,2}(t) = -\frac{1}{2} \kappa \rho_{5,2}(t) - (V \rho_{4,2}(t) - V \rho_{5,1}(t) - \rho_{5,2}(t) \omega - V \rho_{5,3}(t)) I - \frac{1}{2} \gamma_{5,2} \rho_{5,2}(t)$$

$$\frac{d}{dt} \rho_{5,3}(t) = -\frac{1}{2} \kappa \rho_{5,3}(t) - (V \rho_{4,3}(t) - V \rho_{5,2}(t) - \rho_{5,3}(t) \omega - V \rho_{5,4}(t)) I - \frac{1}{2} \gamma_{5,3} \rho_{5,3}(t)$$

$$\frac{d}{dt} \rho_{5,4}(t) = -\frac{1}{2} \kappa \rho_{5,4}(t) - (V \rho_{4,4}(t) - V \rho_{5,3}(t) - \rho_{5,4}(t) \omega - V \rho_{5,5}(t)) I - \frac{1}{2} \gamma_{5,4} \rho_{5,4}(t)$$

$$\frac{d}{dt} \rho_{5,5}(t) = -\kappa \rho_{5,5}(t) - (V \rho_{4,5}(t) - V \rho_{5,4}(t)) I$$

EOM for N=2 are given below.

For Decoherence Scheme 1, Full Dephasing (on blue and red sites), $\gamma_{ij}=\gamma$ for all i,j

For Decoherence Scheme 2, Dephasing on Nodes only (on blue sites), $\gamma_{ij}=\gamma$ for i or $j=2$ or 5 ,

$\gamma_{ij}=0$ for all other i,j

For Decoherence Scheme 3, Dephasing on Degenerate Bridges only (on red sites), $\gamma_{ij}=\gamma$ for i or $j=3$ or 4 , $\gamma_{ij}=0$ for all other i,j

$$\rho_{1,1}(t) = 1$$

$$\frac{d}{dt}\rho_{1,2}(t) = (V\rho_{1,1}(t) + \omega\rho_{1,2}(t) + V\rho_{1,3}(t) + V\rho_{1,4}(t))I - \frac{1}{2}\gamma_{1,2}\rho_{1,2}(t)$$

$$\frac{d}{dt}\rho_{1,3}(t) = (V\rho_{1,2}(t) + \omega\rho_{1,3}(t) + V\rho_{1,5}(t))I - \frac{1}{2}\gamma_{1,3}\rho_{1,3}(t)$$

$$\frac{d}{dt}\rho_{1,4}(t) = (V\rho_{1,2}(t) + \omega\rho_{1,4}(t) + V\rho_{1,5}(t))I - \frac{1}{2}\gamma_{1,4}\rho_{1,4}(t)$$

$$\frac{d}{dt}\rho_{1,5}(t) = (V\rho_{1,3}(t) + V\rho_{1,4}(t) + \omega\rho_{1,5}(t) + V\rho_{1,6}(t))I - \frac{1}{2}\gamma_{1,5}\rho_{1,5}(t)$$

$$\frac{d}{dt}\rho_{1,6}(t) = -\frac{1}{2}\kappa\rho_{1,6}(t) + V\rho_{1,5}(t)I$$

$$\frac{d}{dt}\rho_{2,1}(t) = -(V\rho_{1,1}(t) + \omega\rho_{2,1}(t) + V\rho_{3,1}(t) + V\rho_{4,1}(t))I - \frac{1}{2}\gamma_{2,1}\rho_{2,1}(t)$$

$$\frac{d}{dt}\rho_{2,2}(t) = -I(V\rho_{1,2}(t) + V\rho_{3,2}(t) + V\rho_{4,2}(t) - V\rho_{2,1}(t) - V\rho_{2,3}(t) - V\rho_{2,4}(t))$$

$$\frac{d}{dt}\rho_{2,3}(t) = -(V\rho_{1,3}(t) + V\rho_{3,3}(t) + V\rho_{4,3}(t) - V\rho_{2,2}(t) - V\rho_{2,5}(t))I - \gamma_{2,3}\rho_{2,3}(t)$$

$$\frac{d}{dt}\rho_{2,4}(t) = -(V\rho_{1,4}(t) + V\rho_{3,4}(t) + V\rho_{4,4}(t) - V\rho_{2,2}(t) - V\rho_{2,5}(t))I - \gamma_{2,4}\rho_{2,4}(t)$$

$$\frac{d}{dt}\rho_{2,5}(t) =$$

$$-(V\rho_{1,5}(t) + V\rho_{3,5}(t) + V\rho_{4,5}(t) - V\rho_{2,3}(t) - V\rho_{2,4}(t) - V\rho_{2,6}(t))I - \gamma_{2,5}\rho_{2,5}(t)$$

$$\begin{aligned} \frac{d}{dt} \rho_{2,6}(t) = & -\frac{1}{2} \kappa \rho_{2,6}(t) - (V \rho_{1,6}(t) + \omega \rho_{2,6}(t) + V \rho_{3,6}(t) + V \rho_{4,6}(t) - V \rho_{2,5}(t)) I \\ & - \frac{1}{2} \gamma_{2,6} \rho_{2,6}(t) \end{aligned}$$

$$\frac{d}{dt} \rho_{3,1}(t) = -(V \rho_{2,1}(t) + \omega \rho_{3,1}(t) + V \rho_{5,1}(t)) I - \frac{1}{2} \gamma_{3,1} \rho_{3,1}(t)$$

$$\frac{d}{dt} \rho_{3,2}(t) = -(V \rho_{2,2}(t) + V \rho_{5,2}(t) - V \rho_{3,1}(t) - V \rho_{3,3}(t) - V \rho_{3,4}(t)) I - \gamma_{3,2} \rho_{3,2}(t)$$

$$\frac{d}{dt} \rho_{3,3}(t) = -I (V \rho_{2,3}(t) + V \rho_{5,3}(t) - V \rho_{3,2}(t) - V \rho_{3,5}(t))$$

$$\frac{d}{dt} \rho_{3,4}(t) = -(V \rho_{2,4}(t) + V \rho_{5,4}(t) - V \rho_{3,2}(t) - V \rho_{3,5}(t)) I - \gamma_{3,4} \rho_{3,4}(t)$$

$$\frac{d}{dt} \rho_{3,5}(t) = -(V \rho_{2,5}(t) + V \rho_{5,5}(t) - V \rho_{3,3}(t) - V \rho_{3,4}(t) - V \rho_{3,6}(t)) I - \gamma_{3,5} \rho_{3,5}(t)$$

$$\frac{d}{dt} \rho_{3,6}(t) = \frac{1}{2} \kappa \rho_{3,6}(t) - (V \rho_{2,6}(t) + \omega \rho_{3,6}(t) + V \rho_{5,6}(t) - V \rho_{3,5}(t)) I - \frac{1}{2} \gamma_{3,6} \rho_{3,6}(t)$$

$$\frac{d}{dt} \rho_{4,1}(t) = -(V \rho_{2,1}(t) + \omega \rho_{4,1}(t) + V \rho_{5,1}(t)) I - \frac{1}{2} \gamma_{4,1} \rho_{4,1}(t)$$

$$\frac{d}{dt} \rho_{4,2}(t) = -(V \rho_{2,2}(t) + V \rho_{5,2}(t) - V \rho_{4,1}(t) - V \rho_{4,3}(t) - V \rho_{4,4}(t)) I - \gamma_{4,2} \rho_{4,2}(t)$$

$$\frac{d}{dt} \rho_{4,3}(t) = -(V \rho_{2,3}(t) + V \rho_{5,3}(t) - V \rho_{4,2}(t) - V \rho_{4,5}(t)) I - \gamma_{4,3} \rho_{4,3}(t)$$

$$\frac{d}{dt} \rho_{4,4}(t) = -I (V \rho_{2,4}(t) + V \rho_{5,4}(t) - V \rho_{4,2}(t) - V \rho_{4,5}(t))$$

$$\frac{d}{dt} \rho_{4,5}(t) = -(V \rho_{2,5}(t) + V \rho_{5,5}(t) - V \rho_{4,3}(t) - V \rho_{4,4}(t) - V \rho_{4,6}(t)) I - \gamma_{4,5} \rho_{4,5}(t)$$

$$\frac{d}{dt} \rho_{4,6}(t) = -\frac{1}{2} \kappa \rho_{4,6}(t) - (V \rho_{2,6}(t) + \omega \rho_{4,6}(t) + V \rho_{5,6}(t) - V \rho_{4,5}(t)) I - \frac{1}{2} \gamma_{4,6} \rho_{4,6}(t)$$

$$\frac{d}{dt} \rho_{5,1}(t) = -(V \rho_{3,1}(t) + V \rho_{4,1}(t) + \omega \rho_{5,1}(t) + V \rho_{6,1}(t)) I - \frac{1}{2} \gamma_{5,1} \rho_{5,1}(t)$$

$$\begin{aligned} \frac{d}{dt} \rho_{5,2}(t) = \\ -(V \rho_{3,2}(t) + V \rho_{4,2}(t) + V \rho_{6,2}(t) - V \rho_{5,1}(t) - V \rho_{5,3}(t) - V \rho_{5,4}(t)) I - \gamma_{5,2} \rho_{5,2}(t) \end{aligned}$$

$$\frac{d}{dt} \rho_{5,3}(t) = -(V \rho_{3,3}(t) + V \rho_{4,3}(t) + V \rho_{6,3}(t) - V \rho_{5,2}(t) - V \rho_{5,5}(t)) I - \gamma_{5,3} \rho_{5,3}(t)$$

$$\frac{d}{dt} \rho_{5,4}(t) = -(V \rho_{3,4}(t) + V \rho_{4,4}(t) + V \rho_{6,4}(t) - V \rho_{5,2}(t) - V \rho_{5,5}(t)) I - \gamma_{5,4} \rho_{5,4}(t)$$

$$\frac{d}{dt} \rho_{5,5}(t) = -I (V \rho_{3,5}(t) + V \rho_{4,5}(t) + V \rho_{6,5}(t) - V \rho_{5,3}(t) - V \rho_{5,4}(t) - V \rho_{5,6}(t))$$

$$\begin{aligned} \frac{d}{dt} \rho_{5,6}(t) = -\frac{1}{2} \kappa \rho_{5,6}(t) - (V \rho_{3,6}(t) + V \rho_{4,6}(t) + \omega \rho_{5,6}(t) + V \rho_{6,6}(t) - V \rho_{5,5}(t)) I \\ - \frac{1}{2} \gamma_{5,6} \rho_{5,6}(t) \end{aligned}$$

$$\frac{d}{dt} \rho_{6,1}(t) = -\frac{1}{2} \kappa \rho_{6,1}(t) - V \rho_{5,1}(t) I$$

$$\begin{aligned} \frac{d}{dt} \rho_{6,2}(t) = -\frac{1}{2} \kappa \rho_{6,2}(t) - (V \rho_{5,2}(t) - V \rho_{6,1}(t) - \rho_{6,2}(t) \omega - V \rho_{6,3}(t) - V \rho_{6,4}(t)) I \\ - \frac{1}{2} \gamma_{6,2} \rho_{6,2}(t) \end{aligned}$$

$$\frac{d}{dt} \rho_{6,3}(t) = -\frac{1}{2} \kappa \rho_{6,3}(t) - (V \rho_{5,3}(t) - V \rho_{6,2}(t) - \rho_{6,3}(t) \omega - V \rho_{6,5}(t)) I - \frac{1}{2} \gamma_{6,3} \rho_{6,3}(t)$$

$$\frac{d}{dt} \rho_{6,4}(t) = -\frac{1}{2} \kappa \rho_{6,4}(t) - (V \rho_{5,4}(t) - V \rho_{6,2}(t) - \rho_{6,4}(t) \omega - V \rho_{6,5}(t)) I - \frac{1}{2} \gamma_{6,4} \rho_{6,4}(t)$$

$$\begin{aligned} \frac{d}{dt} \rho_{6,5}(t) = & -\frac{1}{2} \kappa \rho_{6,5}(t) - (V \rho_{5,5}(t) - V \rho_{6,3}(t) - V \rho_{6,4}(t) - \rho_{6,5}(t) \omega - V \rho_{6,6}(t)) I \\ & - \frac{1}{2} \gamma_{6,5} \rho_{6,5}(t) \end{aligned}$$

$$\frac{d}{dt} \rho_{6,6}(t) = -\kappa \rho_{6,6}(t) - (V \rho_{5,6}(t) - V \rho_{6,5}(t)) I$$

EOM for N=3 are given below.

For Decoherence Scheme 1, Full Dephasing (on blue and red sites), $\gamma_{ij}=\gamma$ for all i,j

For Decoherence Scheme 2, Dephasing on Nodes only (on blue sites), $\gamma_{ij}=\gamma$ for i or $j=2$ or 6 ,
 $\gamma_{ij}=0$ for all other i,j

For Decoherence Scheme 3, Dephasing on Degenerate Bridges only (on red sites), $\gamma_{ij}=\gamma$ for i or
 $j=3$ or 4 or 5 , $\gamma_{ij}=0$ for all other i,j

$$\rho_{1,1}(t) = 1$$

$$\frac{d}{dt} \rho_{1,2}(t) = (V \rho_{1,1}(t) + \omega \rho_{1,2}(t) + V \rho_{1,3}(t) + V \rho_{1,4}(t) + V \rho_{1,5}(t)) I - \frac{1}{2} \gamma_{1,2} \rho_{1,2}(t)$$

$$\frac{d}{dt} \rho_{1,3}(t) = (V \rho_{1,2}(t) + \omega \rho_{1,3}(t) + V \rho_{1,6}(t)) I - \frac{1}{2} \gamma_{1,3} \rho_{1,3}(t)$$

$$\frac{d}{dt} \rho_{1,4}(t) = (V \rho_{1,2}(t) + \omega \rho_{1,4}(t) + V \rho_{1,6}(t)) I - \frac{1}{2} \gamma_{1,4} \rho_{1,4}(t)$$

$$\frac{d}{dt} \rho_{1,5}(t) = (V \rho_{1,2}(t) + \omega \rho_{1,5}(t) + V \rho_{1,6}(t)) I - \frac{1}{2} \gamma_{1,5} \rho_{1,5}(t)$$

$$\frac{d}{dt} \rho_{1,6}(t) = (V \rho_{1,3}(t) + V \rho_{1,4}(t) + V \rho_{1,5}(t) + \omega \rho_{1,6}(t) + V \rho_{1,7}(t)) I - \frac{1}{2} \gamma_{1,6} \rho_{1,6}(t)$$

$$\frac{d}{dt} \rho_{1,7}(t) = -\frac{1}{2} \kappa \rho_{1,7}(t) + V \rho_{1,6}(t) I$$

$$\frac{d}{dt} \rho_{2,1}(t) = -(V \rho_{1,1}(t) + \omega \rho_{2,1}(t) + V \rho_{3,1}(t) + V \rho_{4,1}(t) + V \rho_{5,1}(t)) I - \frac{1}{2} \gamma_{2,1} \rho_{2,1}(t)$$

$$\begin{aligned} \frac{d}{dt} \rho_{2,2}(t) = & -I (V \rho_{1,2}(t) + V \rho_{3,2}(t) + V \rho_{4,2}(t) + V \rho_{5,2}(t) - V \rho_{2,1}(t) - V \rho_{2,3}(t) \\ & - V \rho_{2,4}(t) - V \rho_{2,5}(t)) \end{aligned}$$

$$\begin{aligned} \frac{d}{dt} \rho_{2,3}(t) = & \\ & -(V \rho_{1,3}(t) + V \rho_{3,3}(t) + V \rho_{4,3}(t) + V \rho_{5,3}(t) - V \rho_{2,2}(t) - V \rho_{2,6}(t)) I - \gamma_{2,3} \rho_{2,3}(t) \end{aligned}$$

$$\begin{aligned} \frac{d}{dt} \rho_{2,4}(t) = & \\ & -(V \rho_{1,4}(t) + V \rho_{3,4}(t) + V \rho_{4,4}(t) + V \rho_{5,4}(t) - V \rho_{2,2}(t) - V \rho_{2,6}(t)) I - \gamma_{2,4} \rho_{2,4}(t) \end{aligned}$$

$$\begin{aligned} \frac{d}{dt} \rho_{2,5}(t) = & \\ & -(V \rho_{1,5}(t) + V \rho_{3,5}(t) + V \rho_{4,5}(t) + V \rho_{5,5}(t) - V \rho_{2,2}(t) - V \rho_{2,6}(t)) I - \gamma_{2,5} \rho_{2,5}(t) \end{aligned}$$

$$\begin{aligned} \frac{d}{dt} \rho_{2,6}(t) = & -(V \rho_{1,6}(t) + V \rho_{3,6}(t) + V \rho_{4,6}(t) + V \rho_{5,6}(t) - V \rho_{2,3}(t) - V \rho_{2,4}(t) \\ & - V \rho_{2,5}(t) - V \rho_{2,7}(t)) I - \gamma_{2,6} \rho_{2,6}(t) \end{aligned}$$

$$\begin{aligned} \frac{d}{dt} \rho_{2,7}(t) = & \frac{1}{2} \kappa \rho_{2,7}(t) \\ & - (V \rho_{1,7}(t) + \omega \rho_{2,7}(t) + V \rho_{3,7}(t) + V \rho_{4,7}(t) + V \rho_{5,7}(t) - V \rho_{2,6}(t)) I \\ & - \frac{1}{2} \gamma_{2,7} \rho_{2,7}(t) \end{aligned}$$

$$\frac{d}{dt} \rho_{3,1}(t) = -(V \rho_{2,1}(t) + \omega \rho_{3,1}(t) + V \rho_{6,1}(t)) I - \frac{1}{2} \gamma_{3,1} \rho_{3,1}(t)$$

$$\frac{d}{dt} \rho_{3,2}(t) = -(V \rho_{2,2}(t) + V \rho_{6,2}(t) - V \rho_{3,1}(t) - V \rho_{3,3}(t) - V \rho_{3,4}(t) - V \rho_{3,5}(t)) I - \gamma_{3,2} \rho_{3,2}(t)$$

$$\frac{d}{dt} \rho_{3,3}(t) = -I (V \rho_{2,3}(t) + V \rho_{6,3}(t) - V \rho_{3,2}(t) - V \rho_{3,6}(t))$$

$$\frac{d}{dt} \rho_{3,4}(t) = -(V \rho_{2,4}(t) + V \rho_{6,4}(t) - V \rho_{3,2}(t) - V \rho_{3,6}(t)) I - \gamma_{3,4} \rho_{3,4}(t)$$

$$\frac{d}{dt} \rho_{3,5}(t) = -(V \rho_{2,5}(t) + V \rho_{6,5}(t) - V \rho_{3,2}(t) - V \rho_{3,6}(t)) I - \gamma_{3,5} \rho_{3,5}(t)$$

$$\frac{d}{dt} \rho_{3,6}(t) = -(V \rho_{2,6}(t) + V \rho_{6,6}(t) - V \rho_{3,3}(t) - V \rho_{3,4}(t) - V \rho_{3,5}(t) - V \rho_{3,7}(t)) I - \gamma_{3,6} \rho_{3,6}(t)$$

$$\frac{d}{dt} \rho_{3,7}(t) = -\frac{1}{2} \kappa \rho_{3,7}(t) - (V \rho_{2,7}(t) + \omega \rho_{3,7}(t) + V \rho_{6,7}(t) - V \rho_{3,6}(t)) I - \frac{1}{2} \gamma_{3,7} \rho_{3,7}(t)$$

$$\frac{d}{dt} \rho_{4,1}(t) = -(V \rho_{2,1}(t) + \omega \rho_{4,1}(t) + V \rho_{6,1}(t)) I - \frac{1}{2} \gamma_{4,1} \rho_{4,1}(t)$$

$$\frac{d}{dt} \rho_{4,2}(t) = -(V \rho_{2,2}(t) + V \rho_{6,2}(t) - V \rho_{4,1}(t) - V \rho_{4,3}(t) - V \rho_{4,4}(t) - V \rho_{4,5}(t)) I - \gamma_{4,2} \rho_{4,2}(t)$$

$$\frac{d}{dt} \rho_{4,3}(t) = -(V \rho_{2,3}(t) + V \rho_{6,3}(t) - V \rho_{4,2}(t) - V \rho_{4,6}(t)) I - \gamma_{4,3} \rho_{4,3}(t)$$

$$\frac{d}{dt} \rho_{4,4}(t) = -I (V \rho_{2,4}(t) + V \rho_{6,4}(t) - V \rho_{4,2}(t) - V \rho_{4,6}(t))$$

$$\frac{d}{dt} \rho_{4,5}(t) = -(V \rho_{2,5}(t) + V \rho_{6,5}(t) - V \rho_{4,2}(t) - V \rho_{4,6}(t)) I - \gamma_{4,5} \rho_{4,5}(t)$$

$$\frac{d}{dt} \rho_{4,6}(t) = -(V \rho_{2,6}(t) + V \rho_{6,6}(t) - V \rho_{4,3}(t) - V \rho_{4,4}(t) - V \rho_{4,5}(t) - V \rho_{4,7}(t)) I - \gamma_{4,6} \rho_{4,6}(t)$$

$$\frac{d}{dt} \rho_{4,7}(t) = \frac{1}{2} \kappa \rho_{4,7}(t) - (V \rho_{2,7}(t) + \omega \rho_{4,7}(t) + V \rho_{6,7}(t) - V \rho_{4,6}(t)) I - \frac{1}{2} \gamma_{4,7} \rho_{4,7}(t)$$

$$\frac{d}{dt} \rho_{5,1}(t) = -(V \rho_{2,1}(t) + \omega \rho_{5,1}(t) + V \rho_{6,1}(t)) I - \frac{1}{2} \gamma_{5,1} \rho_{5,1}(t)$$

$$\frac{d}{dt} \rho_{5,2}(t) = -(V \rho_{2,2}(t) + V \rho_{6,2}(t) - V \rho_{5,1}(t) - V \rho_{5,3}(t) - V \rho_{5,4}(t) - V \rho_{5,5}(t)) I - \gamma_{5,2} \rho_{5,2}(t)$$

$$\frac{d}{dt} \rho_{5,3}(t) = -(V \rho_{2,3}(t) + V \rho_{6,3}(t) - V \rho_{5,2}(t) - V \rho_{5,6}(t)) I - \gamma_{5,3} \rho_{5,3}(t)$$

$$\frac{d}{dt} \rho_{5,4}(t) = -(V \rho_{2,4}(t) + V \rho_{6,4}(t) - V \rho_{5,2}(t) - V \rho_{5,6}(t)) I - \gamma_{5,4} \rho_{5,4}(t)$$

$$\frac{d}{dt} \rho_{5,5}(t) = -I (V \rho_{2,5}(t) + V \rho_{6,5}(t) - V \rho_{5,2}(t) - V \rho_{5,6}(t))$$

$$\frac{d}{dt} \rho_{5,6}(t) = -(V \rho_{2,6}(t) + V \rho_{6,6}(t) - V \rho_{5,3}(t) - V \rho_{5,4}(t) - V \rho_{5,5}(t) - V \rho_{5,7}(t)) I - \gamma_{5,6} \rho_{5,6}(t)$$

$$\frac{d}{dt} \rho_{5,7}(t) = \frac{1}{2} \kappa \rho_{5,7}(t) - (V \rho_{2,7}(t) + \omega \rho_{5,7}(t) + V \rho_{6,7}(t) - V \rho_{5,6}(t)) I - \frac{1}{2} \gamma_{5,7} \rho_{5,7}(t)$$

$$\frac{d}{dt} \rho_{6,1}(t) = -(V \rho_{3,1}(t) + V \rho_{4,1}(t) + V \rho_{5,1}(t) + \omega \rho_{6,1}(t) + V \rho_{7,1}(t)) I - \frac{1}{2} \gamma_{6,1} \rho_{6,1}(t)$$

$$\frac{d}{dt} \rho_{6,2}(t) = -(V \rho_{3,2}(t) + V \rho_{4,2}(t) + V \rho_{5,2}(t) + V \rho_{7,2}(t) - V \rho_{6,1}(t) - V \rho_{6,3}(t) - V \rho_{6,4}(t) - V \rho_{6,5}(t)) I - \gamma_{6,2} \rho_{6,2}(t)$$

$$\begin{aligned} \frac{d}{dt} \rho_{6,3}(t) = & \\ & -(V \rho_{3,3}(t) + V \rho_{4,3}(t) + V \rho_{5,3}(t) + V \rho_{7,3}(t) - V \rho_{6,2}(t) - V \rho_{6,6}(t)) I - \gamma_{6,3} \rho_{6,3}(t) \end{aligned}$$

$$\begin{aligned} \frac{d}{dt} \rho_{6,4}(t) = & \\ & -(V \rho_{3,4}(t) + V \rho_{4,4}(t) + V \rho_{5,4}(t) + V \rho_{7,4}(t) - V \rho_{6,2}(t) - V \rho_{6,6}(t)) I - \gamma_{6,4} \rho_{6,4}(t) \end{aligned}$$

$$\begin{aligned} \frac{d}{dt} \rho_{6,5}(t) = & \\ & -(V \rho_{3,5}(t) + V \rho_{4,5}(t) + V \rho_{5,5}(t) + V \rho_{7,5}(t) - V \rho_{6,2}(t) - V \rho_{6,6}(t)) I - \gamma_{6,5} \rho_{6,5}(t) \end{aligned}$$

$$\begin{aligned} \frac{d}{dt} \rho_{6,6}(t) = & -I (V \rho_{3,6}(t) + V \rho_{4,6}(t) + V \rho_{5,6}(t) + V \rho_{7,6}(t) - V \rho_{6,3}(t) - V \rho_{6,4}(t) \\ & - V \rho_{6,5}(t) - V \rho_{6,7}(t)) \end{aligned}$$

$$\begin{aligned} \frac{d}{dt} \rho_{6,7}(t) = & -\frac{1}{2} \kappa \rho_{6,7}(t) \\ & - (V \rho_{3,7}(t) + V \rho_{4,7}(t) + V \rho_{5,7}(t) + \omega \rho_{6,7}(t) + V \rho_{7,7}(t) - V \rho_{6,6}(t)) I \\ & - \frac{1}{2} \gamma_{6,7} \rho_{6,7}(t) \end{aligned}$$

$$\frac{d}{dt} \rho_{7,1}(t) = -\frac{1}{2} \kappa \rho_{7,1}(t) - V \rho_{6,1}(t) I$$

$$\begin{aligned} \frac{d}{dt} \rho_{7,2}(t) = & -\frac{1}{2} \kappa \rho_{7,2}(t) \\ & - (V \rho_{6,2}(t) - V \rho_{7,1}(t) - \rho_{7,2}(t) \omega - V \rho_{7,3}(t) - V \rho_{7,4}(t) - V \rho_{7,5}(t)) I \\ & - \frac{1}{2} \gamma_{7,2} \rho_{7,2}(t) \end{aligned}$$

$$\frac{d}{dt} \rho_{7,3}(t) = -\frac{1}{2} \kappa \rho_{7,3}(t) - (V \rho_{6,3}(t) - V \rho_{7,2}(t) - \rho_{7,3}(t) \omega - V \rho_{7,6}(t)) I - \frac{1}{2} \gamma_{7,3} \rho_{7,3}(t)$$

$$\frac{d}{dt} \rho_{7,4}(t) = -\frac{1}{2} \kappa \rho_{7,4}(t) - (V \rho_{6,4}(t) - V \rho_{7,2}(t) - \rho_{7,4}(t) \omega - V \rho_{7,6}(t)) I - \frac{1}{2} \gamma_{7,4} \rho_{7,4}(t)$$

$$\frac{d}{dt} \rho_{7,5}(t) = -\frac{1}{2} \kappa \rho_{7,5}(t) - (V \rho_{6,5}(t) - V \rho_{7,2}(t) - \rho_{7,5}(t) \omega - V \rho_{7,6}(t)) I - \frac{1}{2} \gamma_{7,5} \rho_{7,5}(t)$$

$$\frac{d}{dt} \rho_{7,6}(t) = -\frac{1}{2} \kappa \rho_{7,6}(t)$$

$$- (V \rho_{6,6}(t) - V \rho_{7,3}(t) - V \rho_{7,4}(t) - V \rho_{7,5}(t) - \rho_{7,6}(t) \omega - V \rho_{7,7}(t)) I$$

$$- \frac{1}{2} \gamma_{7,6} \rho_{7,6}(t)$$

$$\frac{d}{dt} \rho_{7,7}(t) = -\kappa \rho_{7,7}(t) - (V \rho_{6,7}(t) - V \rho_{7,6}(t)) I$$

Acknowledgement: Abraham Nitzan (helpful conversations)

Chapter 5 Electron Transfer in Multiply-Bridged Donor-Acceptor
Molecules: Dephasing and Quantum Coherence

5.1 Introduction

While phase coherence in macroscopic charge transport phenomena (including in conjugated polymers) is relatively unimportant,¹⁵³ it can be very significant in micro- and nanoscale charge transport. Indeed, phase coherence has been shown to be crucial to the observation of Aharonov-Bohm effects in microscopic metal rings,¹⁵⁴ to the explanation of amplified conformational sensitivity of electron transfer rates in photosynthetic proteins,³⁷ and to the proposed mechanism of some quantum molecular devices.¹⁵⁵⁻¹⁵⁷ Consequently, dephasing processes will have a profound effect on these phenomena, requiring careful study of the mechanisms of these dephasing processes. In this paper, we explore, for a few simple site models, the role of local pure dephasing in determining electron transfer rate constants in multiply-bridged donor-acceptor systems. We believe pure dephasing to be relevant to a large range of physical and chemical behavior, and contrast its effects on electron transfer with the effects of an energy loss mechanism.

We consider a system with connectivity defined by Figure 17A in which Site D denotes the electron Donor, A the electron Acceptor, and B the covalently bound intervening chemical Bridge. The system is immersed in a solvent bath where dephasing can result from a number of interactions between the electron and the internal degrees of freedom of the molecular nuclei and/or the molecule's environment.⁴⁷ Elastic processes driven by coupling to the vibronic quasicontinuum of the B electronic state result in "phase erosion" and can cause the population buildup on the B site, that is the hallmark of sequential, or "hopping" transport.²⁴ Inelastic (or relaxation) processes have become especially important in interrogation of the molecule in the

context of a M-M-M (metal-molecule-metal) transport junction,¹⁵⁸ but they also cause the phase loss on the site A that is necessary for irreversible (ie, non oscillatory) electron transfer.¹⁵

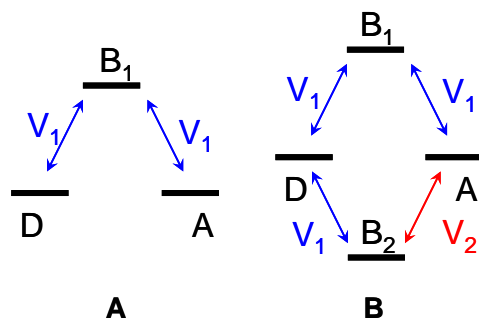


Figure 17 (A) Simple D-B-A connectivity, (B) Connectivity of a “Joachim” type molecular interferometer. B_n levels are at an energy ω above the degenerate D and A levels

This paper explicitly treats a system defined by the connectivity illustrated in Figure 17B. Here, the consequences of phase coherence are much more easily visualized as the output of a molecular interferometer. Beginning with the work of Sautet and Joachim³², a number of reports have explored multiple spatial pathway electron transfer^{27, 30, 37, 38, 44, 56, 57, 131, 152, 159, 160}. Skourtis, Waldeck, and Beratan⁵⁷ have shown that if the tunneling electron deposits energy into the vibronic manifold of a B site, then this inelastic interaction is sufficient to destroy coherence between the two pathways and may result in the recovery of effective communication between the D and A sites that was previously lost due to destructive interference. For this system geometry we will show that elastic processes, i.e, dephasing without relaxation, can also destroy coherence between pathways and recover transport. These elastic dephasing processes can be interpreted as the result of coupling to a solvent bath, and are thus general to a range of chemical phenomena.

5.2 Results and Discussion

5.2.1 System, Dynamics, and Steady State.

We adopt a simple tight-binding Hückel type Hamiltonian, with the connectivity defined by Figure 17B reflected in the off-diagonal coupling V between sites. The energies of the D and A sites are taken to be degenerate and define the zero level of energy for the system. The energy of all B sites is taken to be ω above the D and A sites. This Hamiltonian is completely electronic,¹³⁸ no vibrational degrees of freedom are included.

The density matrix formalism provides a convenient method to probe the nature of coherent interaction between sites.¹⁶¹ Dynamics are then calculated from the quantum Liouville equation

$$\dot{\rho} = \frac{-i}{\hbar}[H, \rho] + L_D \rho \quad (5.1)$$

where H is the Hückel Hamiltonian, ρ is the electronic density matrix, and L_D contains any non-Hamiltonian dynamics. In all cases presented here, L_D contains terms that phenomenologically induce the thermal relaxation arising from nuclear motions absent in our simple electronic Hamiltonian. Such an approach is nearly universal when describing relaxation processes^{22, 51, 161} beginning with NMR¹⁶². Along with the simplification described below arising from making a steady-state assumption, this method has been used previously to show the loss of coherence in Raman scattering processes¹⁶³ and to show the transition from coherent superexchange to incoherent “hopping” in intramolecular electron transfer^{26, 106, 136, 164}. Depending on the nature of L_D , this approach can become equivalent to the calculation of transmission coefficients using the Green’s function formalism in the limit of relaxation to a continuum of sites.¹³⁶

Following these previous examples, the wavefunction associated with the D site is maintained at constant amplitude and phase while population deposited on the A site is “relaxed” out of the site at with a rate $C = \kappa\rho_{AA}$, and rate constant, κ . This relaxation is provided by an absorbing boundary. Note that this relaxation only occurs on the A site and thus does not directly affect the coherences among the bridge sites that result in interferences. The electron transfer rate is then calculated as a product of this rate constant, κ , and the ratio of the steady state populations on the D and A sites,

$$k_{ET} = \kappa \frac{\rho_{AA}^{SS}}{\rho_{DD}^{SS}} \quad (5.2)$$

Pure dephasing is added via further extension of the L_D term. These terms are pure real values that are added in the off diagonal coherences among bridge sites in the density matrix. When the new dynamics are calculated using the quantum Liouville equation, such local pure real terms relax the inter-bridge coherences to zero, corresponding to a pure local dephasing on the bridge. The rate constant for the process, γ , to be discussed later, can be viewed as a temperature dependent parameter that reflects the magnitude of thermal dephasing as a result of coupling to the bath.

Rather than calculate the dynamics as the system reaches its steady state, which is computationally prohibitive for the larger dimensionality systems, $\dot{\rho}$ is set to zero and the steady state populations are determined. The steady state approximation has been verified for low dimensional systems (chapter 4). Full computational details are presented in the appendix

5.2.2 Destructive Interference and Dephasing.

A general formulation of destructive interference during intramolecular electron transfer was first advanced by Joachim and coworkers^{44, 159} and is depicted in Figure 17B. Both pathways to B sites from D are equivalent, but the couplings from B to A have different values.

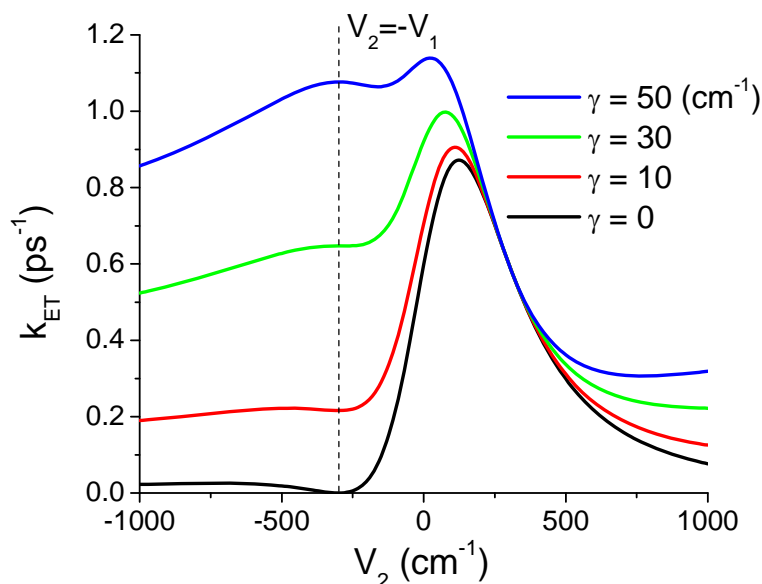


Figure 18 Recovery of transport with increasing pure dephasing rate in a system with connectivity defined by Figure 1(B). $V_1 = 300 \text{ cm}^{-1}$ $\omega = 500 \text{ cm}^{-1}$ $\kappa = 20 \text{ cm}^{-1}$.

Modulation of V_2 significantly affects the overall electron transfer rate, with the rate going to zero due to complete destructive interference when $V_2 = -V_1$. This model was applied by Skourtis and coworkers⁵⁷ in discussion of the observations of Zeng and Zimmt⁴⁵ on symmetry-forbidden electron transfer. This study is one of the only unambiguous experimental examples of destructive interference in D-B-A systems. The symmetry prohibition of the electron transfer can be seen as resulting from destructive interference between two pathways of opposite

coupling sign. Skourtis and coworkers predicted that the interference could be erased by the electron depositing energy inelastically on one of the B sites.

As demonstrated in Figure 18, we also see complete destructive interference when $V_2 = -V_1$ in the coherent limit. However, in addition to previously described inelastic processes, the interference can also be erased with no energy loss, by a pure dephasing process. As the dephasing rate γ increases in magnitude, the value of k_{ET} rises from zero at $V_2 = -V_1$. The destructive interference is seen to be completely destroyed and the transport recovered.

What is the physical basis of γ ? By destroying the coherences among B sites but not causing any (inelastic) relaxation processes, γ can be identified¹⁶⁵ with T_2^* processes in analogy with broadening in magnetic resonance^{162, 166}, where (after separating out effects for field inhomogeneity) T_2^* processes chiefly stem from dipolar interactions.¹⁶⁷ However, pure dephasing can be recast as any interaction that alters phase of the relevant wavefunction components but does not affect population. The form of that interaction is responsible for the dependency of the dephasing rate on temperature, solvent dielectric, or any other environmental parameter.¹⁶⁸ For intramolecular electron transfer within the D-B-A molecule in solution, relevant contributors will include electrostatic interactions, vibrational motion changing the value of V , and collisions with the solvent bath. These contributors could be seen as causing the recovery of transport in Figure 18. Larger values of ω make the system more resistant to dephasing processes, with similar transport recovery being obtained only with correspondingly higher values of γ . This behavior stems from a shorter contact time (analogous to the Landauer-Buttiker time^{25, 169}) on the bridge as a result of the larger gap.

What is a realistic expectation for the range of values of γ ? Time resolved studies on the timescales (T_2) for the dephasing of coherent interactions between optically prepared excitons in

conjugated polymers^{170, 171} and on Raman cross sections of chromophores in the bacterial photosynthetic reaction center¹⁷² put dephasing times in the range of tens to several hundred fs. This range of times translates into a range of energies from tens to many hundreds of cm^{-1} . Though these experimental studies cannot separate T_2 and T_2^* , it seems reasonable to consider values of γ on the order of a thousand cm^{-1} .

The non-symmetric behavior of k_{ET} with V_2 is also noteworthy. This asymmetry is a consequence of the interference of two non-degenerate pathways in the presence of level broadening (contributed here from either κ or γ and κ). This interference is qualitatively similar to the physical basis of the Fano resonance,¹⁷³ which was derived to explain features of atomic excitation spectra¹⁷⁴. Indeed, the shape of Figure 18, which is relatively independent of the values of κ and ω , is strongly reminiscent of the familiar Fano lineshape. The rise at larger values of V_2 with non-zero values of γ is a result of bridge occupation and hopping transport and has been discussed previously.²⁶

5.2.3 Benzene and Davidene.

While orbital symmetry can introduce a negative sign in the coupling between a donor and acceptor, negative coupling can also be introduced by system connectivity. One such system is defined in Figure 19A and, by design, strongly resembles benzene. The calculated k_{ET} rate for this system with different A contact points is shown in Figure 19B. In the coherent limit ($\gamma = 0$), effective coupling via the ortho and para linkages is non-zero, whereas coupling via the meta linkage is analytically zero. As γ increases, transport via the ortho and para linkages is diminished while transport via the meta linkage rises. As γ reaches extremely high values, transport via all three geometries attains the same value.

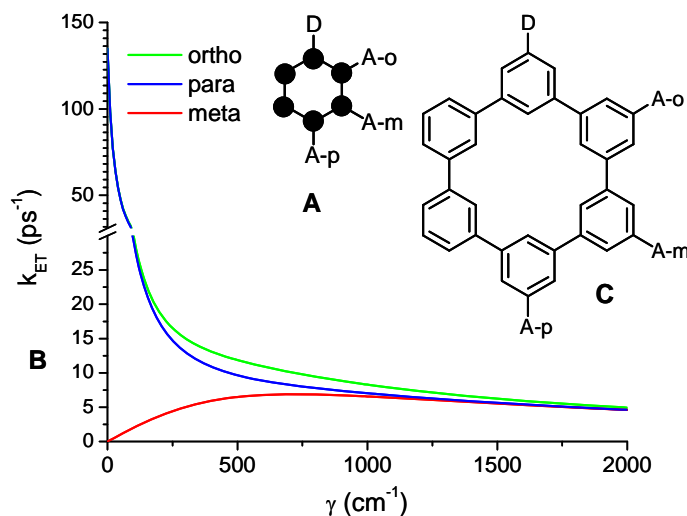


Figure 19 (A) “Benzene” type system connectivity, (B) Coalescence of ortho, meta, and para conductance with increasing pure dephasing rate. $V = 300 \text{ cm}^{-1}$, $\omega = 0 \text{ cm}^{-1}$, $\kappa = 20 \text{ cm}^{-1}$, (C) A davidene molecule.

While greater coupling via para or ortho connection compared to a meta connection between D and A sites is expected from general physical organic arguments,¹⁷⁵ it can also be viewed as resulting from destructive interference between multiple pathways along the carbon chain. Interference effects on the conductance of cyclic hydrocarbons has been addressed by several groups.^{27, 30, 32} The destructive interference is a result of the “parity rule,”^{40, 41, 176} which stems from shifts in the phase of the molecular wavefunction as more atomic orbitals are added in a linear path. An odd number of intervening orbitals are said to impart a “positive coupling” between the two distal orbitals, whereas the through-space interaction (as well as an even number of orbitals) is intrinsically a “negative coupling.” The sign of the effective coupling is

important in the rationalization of spectra of excited state mixed valence compounds,¹⁷⁷ and has also been implicated in the origin of STM images¹⁷⁸ and in the explanation of destructive interference during electron transfer through organic molecules.^{44, 159}

In the limit of complete coherence the meta effective coupling is identically zero, though we know that experimentally the meta effective coupling should be reduced but finite. Using non-zero values of γ or lifting the energetic degeneracy of the atomic orbitals can provide the physically observed non-zero effective meta coupling, thus raising the question of which mechanism is more important, energy shift based on substituents or dephasing? For benzene, it is unlikely that local pure dephasing is dominant. The effects of dephasing are strongly dependent on the length scale over which the dephasing occurs.⁵⁶ Our model demands that two bridge sites lose their coherence, requiring each to interact independently with its environment. This independence seems difficult to obtain on the length scale of a single benzene unit, since discrete solvent molecules are roughly of the same size scale as the entire benzene unit. Dephasing over several bonds could lead to reduced interference and may be operative in benzene.⁵⁶ However, a D-B-A molecule built around a davidene¹⁷⁹ core, as seen in Figure 3C, would provide an interesting vehicle to exaggerate the effects of dephasing. While davidene is known to be non-planar,¹⁸⁰ its twisted geometry is still highly symmetric and nearest neighbor interactions between the phenyl rings are still expected to be dominant. Fluctuations in coupling strength between the rings will likely constitute an important source of dephasing. More importantly, phenyl units could interact with the solvent independently of each other, and the magnitude of the already weak meta coupling between units would make the system more sensitive to γ . Consequently, by adjusting temperature and solvent conditions one could hope to approach regions of Figure 19B where dephasing effects cause a convergence of the electron

transfer rates measured in all three effective “ortho, meta, and para” connectivities of davidene. Then, the electron transfer rate could provide a clear observation of the dephasing effect.

5.3 Conclusion

In summary, we have shown that elastic pure local dephasing is capable of erasing interference effects in D-B-A molecules; whether the cause of the interference arises from the number of units in the pathway or from a negative coupling in one of the pathways, pure local dephasing can eliminate the destructive interference. The issue of pure dephasing should be addressed in any system that is required or assumed to behave coherently. The davidene series of molecules offers a considerable synthetic challenge, but the chance to observe experimentally the elimination of destructive interferences as a result of interaction with the environment would significantly enhance, in a simple model system, our understanding of the interplay of coherent and incoherent phenomena.

5.4 Equations of Motion

For the 4 site system depicted in Figure 17B, a tight-binding Hückel type Hamiltonian was constructed

$$H = \begin{pmatrix} 0 & V_1 & V_1 & 0 \\ V_1 & \omega & 0 & V_1 \\ V_1 & 0 & \omega & V_2 \\ 0 & V_1 & V_2 & 0 \end{pmatrix} \quad (5.3)$$

Equations of motion were written for the terms comprising the density matrix.

$$\dot{\rho} = \frac{-i}{\hbar}[H, \rho] + L_D \rho \quad (5.4)$$

$\rho_{11} = 1$ for all systems studied. This constraint, along with the absorbing boundary, allows k_{ET} to be calculated as the flux through the system.¹³⁶

$$\dot{\rho}_{nm} = \dot{c}_n c_m^* + c_n \dot{c}_m^* \quad (5.5)$$

$$\dot{\rho}_{1m} = \dot{c}_1 c_m^* + c_1 \dot{c}_m^* = \dot{c}_m^* \quad (5.6)$$

$$\dot{\rho}_{n1} = \dot{c}_n c_1^* + c_n \dot{c}_1^* = \dot{c}_n \quad (5.7)$$

where $|\Psi\rangle = \sum_n c_n |\phi_n\rangle$, $|\phi_n\rangle$ are the atomic orbitals (comprising a “site basis”), and

$\dot{c}_n = -\frac{i}{\hbar} \langle \phi_n | H | \Psi \rangle$ except for \dot{c}_1 , which, trivially, is zero.

L_D includes the relaxation and pure dephasing terms, and can be decomposed into $L_D = L_{D-R} + L_{D-D}$.

Relaxation from the acceptor site (here $n, m = 4$) is simulated by defining

$$\langle \phi_n | L_{D-R} \rho | \phi_m \rangle = -\frac{1}{2} \kappa \rho_{nm} \delta_{n4} - \frac{1}{2} \kappa \rho_{nm} \delta_{m4} \quad (5.8)$$

where δ is the Kronecker delta and is formally equivalent to adding an imaginary component, $-\frac{i}{2} \kappa$, to the energy of the terminal site.

Additional terms are added to the equations of motion for the coherences among bridge sites (here $n, m = 2, 3$) to simulate pure dephasing.

$$\langle \phi_n | L_{D-D} \rho | \phi_m \rangle = \sum_{j=2,3} \left(-\frac{1}{2} \gamma \rho_{nm} \delta_{nj} (1 - \delta_{nm}) - \frac{1}{2} \gamma \rho_{nm} \delta_{mj} (1 - \delta_{nm}) \right) \quad (5.9)$$

Equations of motion for 4-site system:

$$\rho_{11} = 1$$

$$\dot{\rho}_{22} = -i(V_1 \rho_{12} + V_1 \rho_{42} - V_1 \rho_{21} - V_1 \rho_{24})$$

$$\dot{\rho}_{33} = -i(V_1\rho_{13} + V_2\rho_{43} - V_1\rho_{31} - V_2\rho_{34})$$

$$\dot{\rho}_{44} = -i(V_1\rho_{24} + V_2\rho_{34} - V_1\rho_{42} - V_2\rho_{43}) - \kappa\rho_{44}$$

$$\dot{\rho}_{21} = -i(V_1\rho_{11} + \omega\rho_{21} - V_1\rho_{41}) - \frac{1}{2}\gamma\rho_{21}$$

$$\dot{\rho}_{31} = -i(V_1\rho_{11} + \omega\rho_{31} + V_2\rho_{41}) - \frac{1}{2}\gamma\rho_{31}$$

$$\dot{\rho}_{32} = -i(V_1\rho_{12} + V_2\rho_{42} - V_1\rho_{31} - V_1\rho_{34}) - \frac{1}{2}\gamma\rho_{32}$$

$$\dot{\rho}_{41} = -i(V_1\rho_{21} + V_2\rho_{31}) - \frac{1}{2}\kappa\rho_{41}$$

$$\dot{\rho}_{42} = -i(V_1\rho_{22} + V_2\rho_{32} - V_1\rho_{41} - \omega\rho_{42} - V_1\rho_{44}) - \frac{1}{2}\kappa\rho_{42} - \frac{1}{2}\gamma\rho_{42}$$

$$\dot{\rho}_{43} = -i(V_1\rho_{23} + V_2\rho_{33} - V_1\rho_{41} - \omega\rho_{43} - V_2\rho_{44}) - \frac{1}{2}\kappa\rho_{43} - \frac{1}{2}\gamma\rho_{43}$$

The equations of motion are solved by making a steady state approximation and setting all

$$\dot{\rho}_{mm} = 0. \text{ }^{136}$$

k_{ET} is then defined as the ratio of the steady state populations on the acceptor and donor sites multiplied by the flux through the system from the relaxation term,

$$k_{ET} = \kappa \frac{\rho_{AA}^{SS}}{\rho_{DD}^{SS}} \quad (5.10)$$

For the davidene system, a series of Hamiltonians are defined for the ortho, meta, and para connectivities

$$\begin{aligned}
H_{ortho} &= \begin{pmatrix} 0 & V & 0 & 0 & 0 & 0 & 0 & 0 \\ V & \omega & V & 0 & 0 & 0 & V & 0 \\ 0 & V & \omega & V & 0 & 0 & 0 & 0 \\ 0 & 0 & V & \omega & V & 0 & 0 & 0 \\ 0 & 0 & 0 & V & \omega & V & 0 & 0 \\ 0 & 0 & 0 & 0 & V & \omega & V & 0 \\ 0 & V & 0 & 0 & 0 & V & \omega & V \\ 0 & 0 & 0 & 0 & 0 & 0 & V & 0 \end{pmatrix} & H_{meta} &= \begin{pmatrix} 0 & V & 0 & 0 & 0 & 0 & 0 & 0 \\ V & \omega & V & V & 0 & 0 & 0 & 0 \\ 0 & V & \omega & 0 & 0 & 0 & V & 0 \\ 0 & V & 0 & \omega & V & 0 & 0 & 0 \\ 0 & 0 & 0 & V & \omega & V & 0 & 0 \\ 0 & 0 & 0 & 0 & V & \omega & V & 0 \\ 0 & 0 & V & 0 & 0 & V & \omega & V \\ 0 & 0 & 0 & 0 & 0 & 0 & V & 0 \end{pmatrix} \\
H_{para} &= \begin{pmatrix} 0 & V & 0 & 0 & 0 & 0 & 0 & 0 \\ V & \omega & V & 0 & V & 0 & 0 & 0 \\ 0 & V & \omega & V & 0 & 0 & 0 & 0 \\ 0 & 0 & V & \omega & 0 & 0 & V & 0 \\ 0 & V & 0 & 0 & \omega & V & 0 & 0 \\ 0 & 0 & 0 & 0 & V & \omega & V & 0 \\ 0 & 0 & 0 & V & 0 & V & \omega & V \\ 0 & 0 & 0 & 0 & 0 & 0 & V & 0 \end{pmatrix} & & (5.11)
\end{aligned}$$

Equations of motion are written as above, with the ρ_{11} maintained at 1, relaxation from the acceptor site ($n = 8$) and dephasing between the bridge sites ($n = 2-7$). k_{ET} is then calculated as above from the ratio of the steady state populations multiplied by the relaxation flux.

Acknowledgements: Abraham Nitzan and Vladimiro Mujica (helpful conversations)

Chapter 6 Never Underestimate Your σ -System: Charge Transfer
Through Benzo-Annulated Bicyclo[2.2.2]octanes and Triptycene

6.1 Introduction

Covalently linked Donor-Bridge-Acceptor (D-B-A) molecules, where the bridge is comprised of a σ -bond network, have provided a means of elucidating many of the important aspects of intramolecular charge and energy transfer. Saturated spacer groups provided the first unambiguous confirmation of the existence of the Marcus inverted region.^{8, 9} Bicyclo[2.2.2]octane¹⁰⁰ and norbornane¹⁸¹ spacers provided early means to determine the distance dependence of intramolecular charge transfer through the incremental increase in the length of an oligomeric bridge group. The utility of these classes of molecules stems from their role as nearly rigid spacers or molecular rods.¹⁸² Despite earlier assumptions about their designation as *inert* spacers,²¹ systems containing saturated hydrocarbon bridges have been clearly shown to be electronically relevant to intramolecular charge transfer^{21, 183} and to possess a rich electronic structure,^{33, 34, 39, 130} including interference effects.³⁵ More recently, the majority of attention has moved away from looking at bridges having all σ -bonds to those with π -bonds. Such a shift was motivated by the increased ability of these π -bridges to convey electronic communication between the π systems of the D and A groups by maintaining closer energetic resonance, suggested by McConnell's expression,²⁰ Equation 1,

$$V_{eff} = \frac{V_{D1}V_{NA}}{E_1 - E_{D/A}} \prod_{i=1}^N \frac{V_{i,i+1}}{E_{i+1} - E_{D/A}} \quad (6.1)$$

where V_{ij} are matrix elements between the different subunit wavefunctions and E_i is the energy of a particular subunit.

The pursuit of greater electronic communication has been driven by the potential development of molecular electronic devices (molecular wires)³ as well as understanding

ultrafast energy and electron transfer in the photosynthetic reaction center and related systems.⁹⁸ Studies of π -bridges have revealed qualitatively new transfer regimes that depend on energetic resonance conditions.^{24, 26, 55, 56, 101} Albinsson and coworkers have recently shown a stark contrast between the efficacy of σ - and π -type bridges by comparing a phenyl group and a bicyclo[2.2.2]octane group in equivalent positions in a D-B-A system.^{12, 184} Following the predictions of many earlier experimental and theoretical studies, charge transfer was strongly inhibited by the σ -bridge.

Other recent studies attempting to elucidate ultrafast charge transfer in biological systems have suggested that multiple spatial pathways,^{6, 37-39} possibly summing coherently, may contribute to the overall charge transfer rate. As part of our ongoing efforts to understand charge transfer through multiple spatial pathways,^{56, 135, 185} we attempted to utilize the dichotomy between σ - and π -type bridges to form model D-B-A molecules as systems with which to test predictions about the role of multiple spatial pathways in charge transfer. We had hoped that a σ -system could provide a relatively inert scaffold on which to append multiple weakly interacting π -bridges. In this way, one could maintain a constant geometry, and thus be able to compare meaningfully the effect of additional bridges.

For our σ -scaffold, we chose a 1,4 substituted bicyclo[2.2.2]octane (BCO) group. An electron donor, pyrrolidinophenyl (PP), and acceptor, 9-cyanoanthracene (CA), were then attached via alkyne linkages to the bridge. π -Pathways were then added by replacing the BCO with benzo-annulated BCO's. Up to three π -pathways could be added, with the three-phenyl system comprised of a bridge-head substituted triptycene, as seen in Figure 20. While a few examples of charge and energy transfer systems using asymmetric bridgehead substituted BCO^{100, 183, 186} and triptycene¹⁸⁷ bridges have been reported, and many reports have used various

benzo-annulated BCO molecules to investigate the relative importance of through space and through bond effects,^{188, 189} to our knowledge, this is the first report to examine the full series of four doubly bridgehead substituted benzo-annulated BCO's.

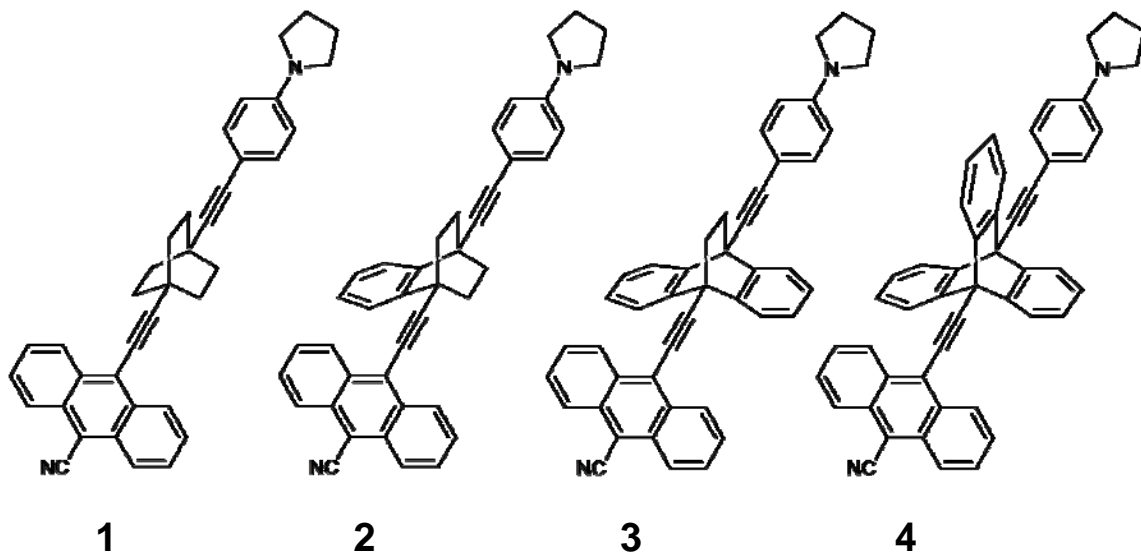


Figure 20 Structures of Donor-Bridge-Acceptor molecules with benzo-annulated BCO bridges

6.2 Results

6.2.1 Molecular Design

Compounds **1-4** were prepared in order to compare the influence of multiple spatially distinct π -pathways in equivalent geometries. The D and A were chosen because of excellent spectroscopic and redox properties, as will be described later, and because they can connect with the bridge via alkyne linkage, which was believed to be capable of conveying electronic communication between the D/A and the bridge π -system.

The synthesis of **1-4** was executed using a building-block approach. Aryl halides of the donor and acceptor were prepared in one step from commercial materials. The synthesis of *p*-

iodopyrrolidinobenzene followed from a literature procedure,¹⁹⁰ while 9-bromo-10-cyanoanthracene¹⁹¹ was prepared from the dibromoderivative using CuCN. The synthesis of the phenyl ethynylated BCO bridges comprised the main synthetic challenge. The diethynyl BCO was prepared using variants of known procedures employed by Sukenik,¹⁹² Kurreck,⁹⁹ Albinsson,¹² and coworkers, Figure 21. The dialkyne derivative of triptycene was prepared using a modification of the procedure of Michl and coworkers,¹⁹³ Figure 22.

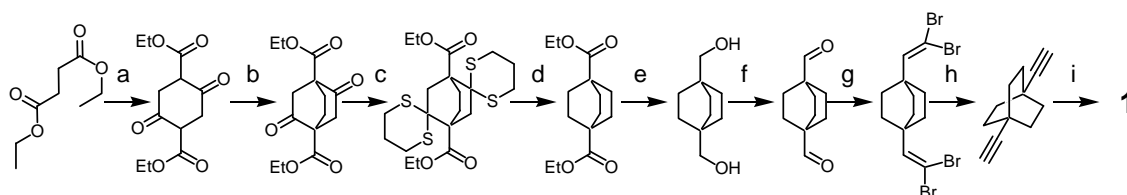


Figure 21 Synthesis of **1** a) KOC_2H_5 , EtOH, 55% b) 1. NaH, DME 2. $\text{C}_2\text{H}_4\text{Br}_2$, 71% c) $\text{HS}(\text{CH}_2)_3\text{SH}$, $\text{BF}_3 \cdot \text{Et}_2\text{O}$, CHCl_3 , 80% d) Raney Ni, EtOH, 98% e) LiAlH_4 , Et_2O , 89% f) oxalyl chloride, DMSO, DCM, quant. g) CBr_4 , PPh_3 , Zn, DCM, hexanes, 53% h) $n\text{-BuLi}$, THF, 76% i) 1. iodophenylpyrrolidine, piperidine, CuI, $\text{Pd}(\text{PPh}_3)_4$ 2. bromocyananthracene, TEA, CuI, $\text{Pd}(\text{PPh}_3)_2\text{Cl}_2$, 9%

In contrast, the benzobicyclo[2.2.2]octane (BBCO) and dibenzobicyclo[2.2.2]octane (DBCO) derivatives with alkynes at the bridgeheads were unknown. The preparation of BBCO, Figure 23, started from dimethyl-1,3-cyclohexadiene-1,4 dicarboxylate, which can be produced in multigram quantities from the corresponding saturated cyclohexyl derivative.¹⁹⁴ The esters were reduced following Chu's procedure¹⁹⁵ and the alcohols were immediately protected with a *tert*-butyldimethylsilyl (TBDMS) group. Reduction of the esters was necessary at this stage because they deactivated the ring system to a degree that made the diene inert toward Diels-

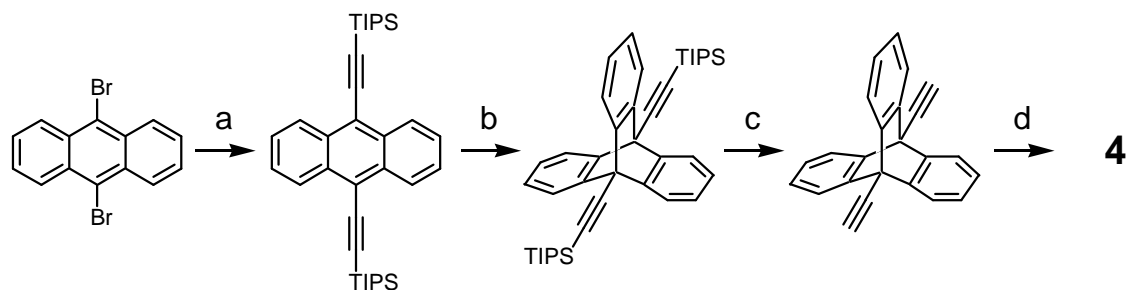


Figure 22 Synthesis of **4** a) TIPS acetylene, DEA, CuI, Pd(PPh₃)₂Cl₂, 95% b) isoamyl nitrite, anthranilic acid, dioxane, 43% c) TBAF, THF, 73% d) 1. bromocycloanthracene, TEA, CuI, Pd(PPh₃)₂Cl₂ 2. iodophenylpyrrolidine, piperidine, CuI, Pd(PPh₃)₄, 15%

Alder reaction with benzoquinone and benzyne. The protected diol, however, reacted easily with benzoquinone to form the BBCO core while attempted reaction with benzyne yielded a complex mixture of products. Following procedures of Schmid¹⁹⁶ and Lin,²³ the Diels-Alder adduct was

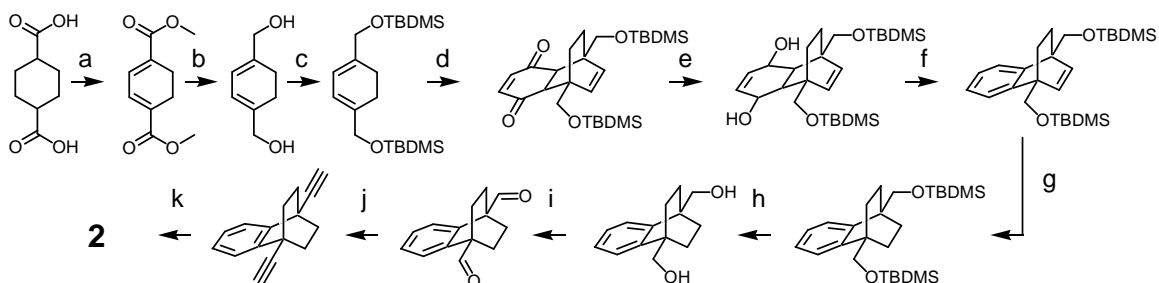


Figure 23 Synthesis of **2** a) 1. SOCl₂, Br₂, MeOH, hv 2. pyridine, 22% b) DIBALH, THF, 42% c) TBDMSCl, DMF, 66% d) *p*-benzoquinone, toluene, 83% e) NaBH₄, CeCl₃·7H₂O, MeOH, DCM, quant. f) POCl₃, pyridine, 68% g) H₂, Pd/C, EtOH, EtOAc, 90% h) TBAF, THF, 95% i) PCC, DCM, 73% j) dimethyl-1-diazo-2-oxopropylphosphonate, K₂CO₃, MeOH, 87% k) 1. bromocycloanthracene, TEA, CuI, Pd(PPh₃)₂Cl₂ 2. iodophenylpyrrolidine, piperidine, CuI, Pd(PPh₃)₄, 5%

reduced, and re-aromatized. The remaining olefin was reduced and the alcohols deprotected. Arbitrary functionality could be added at this point at the bridgehead positions. To construct the alkynes we first oxidized the alcohols to aldehydes. The Corey-Fuchs procedure failed at this

point to produce the desired alkyne. However, application of Bestman's reagent¹⁹⁷ afforded the alkyne directly from the aldehyde in good yield.

Synthesis of the DBCO system, Figure 24, began with the bis-chloromethylation of anthracene,¹⁹⁸ followed by conversion to the bis-acetoxy derivative.¹⁹⁹ Previous attempts to produce ethanoanthracenes relied on addition of maleic anhydride followed by hydrolysis and bisdecarboxylation with lead acetate.²⁰⁰ This route is, however, inconsistent and low yielding. The crucial step in our method is the high pressure Diels-Alder addition of ethene. This addition has been reported previously,¹⁹⁷ but was low yielding in our hands. In contrast, the simple addition of toluene²⁰¹ to the high pressure autoclave allowed the quantitative production of the ethanoanthracene derivative. The acetoxy groups were hydrolyzed and the alcohols were oxidized to aldehydes. The Bestmann reagent was again applied to convert the aldehydes directly to the alkyne.

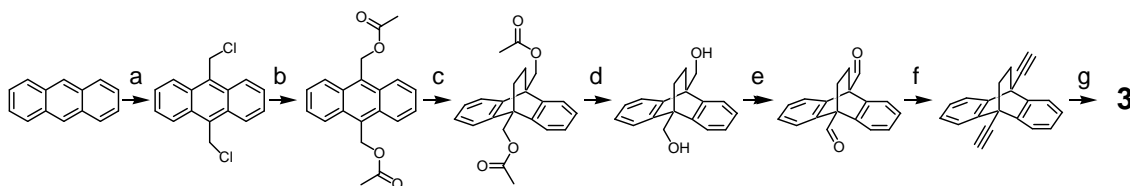


Figure 24 Synthesis of **3** a) paraformaldehyde, $\text{HCl}_{(g)}$, dioxane, 50% b) NaOAc, HOAc, 78% c) toluene, C_2H_4 (2400 psi) d) EtOH, KOH, 93% e) PCC, DCM, 56% f) dimethyl-1-diazo-2-oxopropylphosphonate, K_2CO_3 , MeOH, 92% g) 1. bromocycanoanthracene, TEA, CuI, $\text{Pd}(\text{PPh}_3)_2\text{Cl}_2$ 2. iodophenylpyrrolidine, piperidine, CuI, $\text{Pd}(\text{PPh}_3)_4$, 7%

Sonogashira coupling of the redox active groups to the BCO bridges proved to be difficult, partially because of the reactivities of the D and A aryl halides and partially because of the need to asymmetrically substitute the BCO bridge. Coupling the 9-bromo-10-cyanoanthracene frequently resulted in only the formation of the disubstituted adduct. Coupling the *p*-iodopyrrolidinobenzene proved difficult because of the electron rich nature of the aryl

halide and susceptibility of the alkyne to degradation. Other workers^{12, 202} have reported the successful use of piperidine to couple electron rich aryl halides to bicyclooctyl or triptyceny l alkynes and so we attempted using it as base and/or solvent. After optimizing the conditions, we found that we could form the monosubstituted pyrrolidinobenzene adduct in acceptable yield. However, this monoalkyne quickly degraded with the application of heat or chromatography on silica. Consequently, after washing with water, the crude monoalkyne was used in the next step without further purification. The subsequent reaction of the monoalkyne with 9-bromo-10-cyanoanthracene was successful and the final products **1-4**, though still sensitive to silica gel, could be purified via conventional techniques including preparatory HPLC.

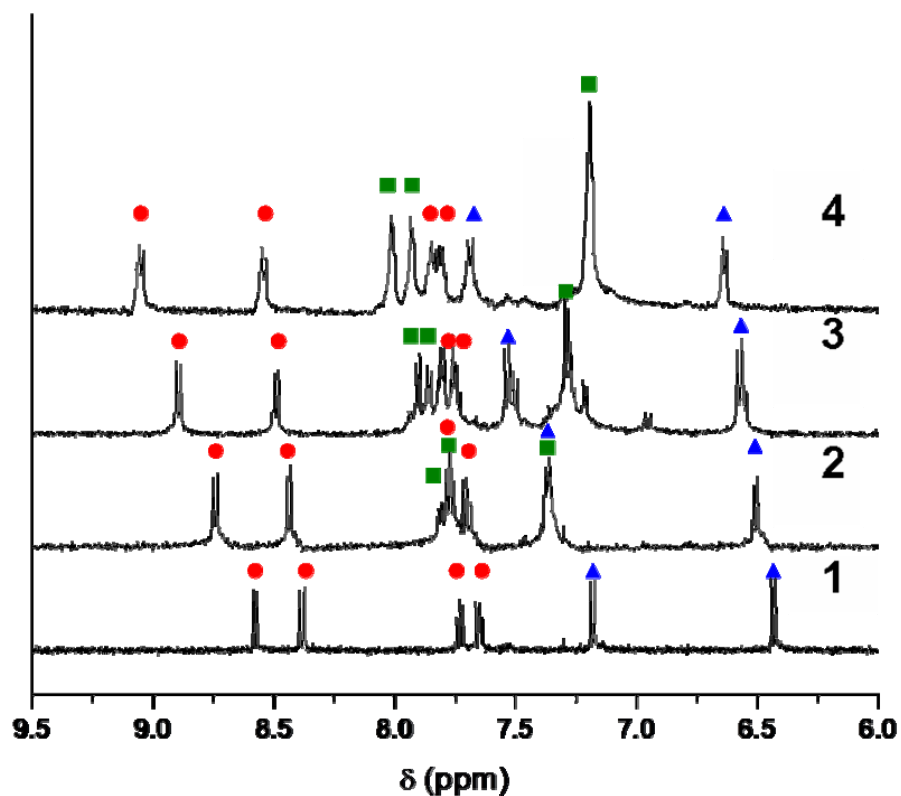


Figure 25 ¹H NMR spectra of the aromatic regions of 1-4 at 300 K in CDCl₃. Red circles denote peaks from CA, blue triangles denote peaks from PP, and green squares denote peaks from the bridge. Notice the downshifting circles and squares.

The aromatic regions of the NMR spectra of 1-4 are shown in Figure 25. As further evidence of the structure, one can see the progressive downfield shift of the protons on the donor and acceptor oriented toward the BCO bridge. As more phenyl groups are fused to the bridge, these protons spend more time caught in the deshielding ring current of the bridge phenyl groups, resulting in this incremental shift down field.

6.2.2 Energy Levels

The donor and acceptor were chosen to meet specific redox and spectroscopic requirements and have been used in previous photoinduced electron transfer studies.¹²⁹ Compounds **5** and **6** were prepared as appropriate models, Figure 26. Cyclic voltammetry was performed and the results are summarized in Table 3

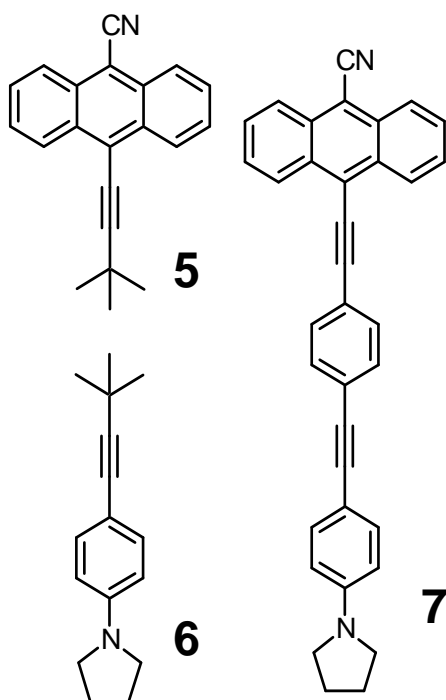


Figure 26 Structures of model compounds with CA and PP

These values were used to estimate the energy of the radical pair state by employing Weller's expression,¹³ which relies on the Born dielectric continuum model. The free energy change for charge separation, ΔG_{CS} , from the locally excited CA group can then be calculated. To calculate internal reorganization energies for the donor and acceptor, λ_i , we first geometry optimized the appropriate ions of **5** and **6**. Taking the difference in self-consistent field (SCF) energy of the charged and neutral species in this geometry yielded λ_i . The solvent reorganization energy, λ_s , was calculated from Marcus's formula¹¹⁷ assuming a dielectric continuum. Finally, using the

classical Marcus expression,¹¹⁷ the activation barrier for charge separation can be calculated.

Results for toluene and MTHF are shown in

Table 3, and sample calculations are presented in a later section.

E_{ox}	E_{red}		ΔG_{CS}	λ_{I}	λ_{O}	$\Delta G_{\text{CS}}^{\ddagger}$
0.74	-1.27	Toluene	-0.02	0.21	0.05	0.055
		MTHF	-0.57	0.21	0.72	0.034

Table 3 Relevant electron transfer parameters for 1-4

6.2.3 Spectroscopy

Ground state absorption spectra of **1-5** and another model compound, **7** (Figure 26), are shown in Figure 27. The CA acceptor dominates the absorption in this region, although the progressive red shift of the bridge absorption can also be seen. Comparison of **1-4** with **5** shows only minimal deviations, showing that the CA acceptor is effectively electronically isolated from the rest of the molecule. In contrast, the absorption spectra of **7** is very different, indicative of significant communication between the donor and acceptor.

Photoexcitation of CA at either 416 or 430 nm results in efficient charge transfer to form the radical ion pair, $\text{PP}^{+\bullet}\text{-B-CA}^{\bullet-}$. The transient absorption spectra are dominated by absorption of ^1CA at early times and $\text{CA}^{\bullet-}$ at later times, as shown in Figure 28. The observed $\text{CA}^{\bullet-}$ absorption is qualitatively similar to the electrochemically generated anion of a related substituted CA compound.¹²⁹ Transient absorption spectra of **5** in toluene shows only ^1CA while **1-4** and **7** show the distinct features of $\text{CA}^{\bullet-}$. Transient absorption spectra of **1-4** show different λ_{max} values for $\text{CA}^{\bullet-}$, while all the spectra are essentially identical in toluene, Figure 29.

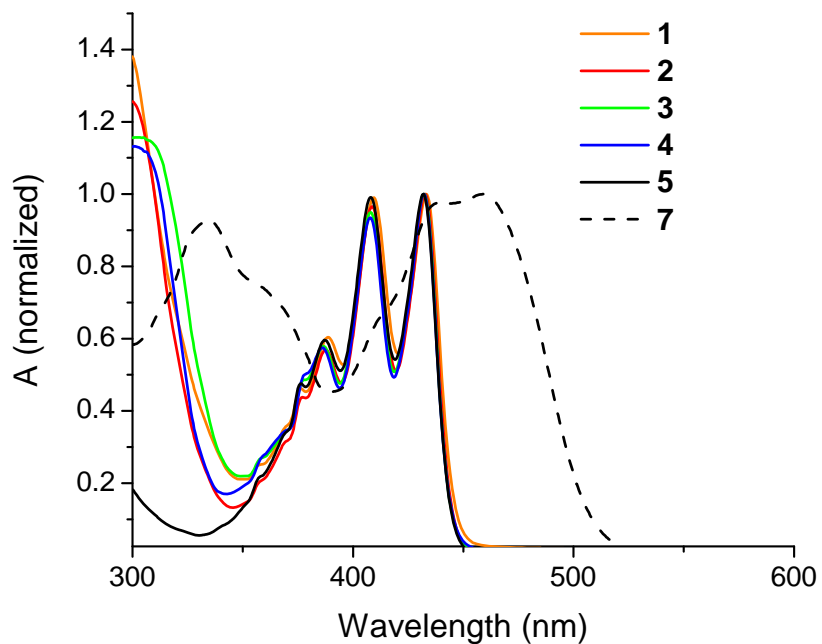


Figure 27 Steady-state UV-vis spectra of **1-5** and **7** in toluene at **295 K**.

Charge separation (CS) and recombination (CR) dynamics can be examined by measuring the rise and the fall of the $CA^{\cdot-}$ feature. Representative kinetics for **1-4** are shown in Figure 30, while time constants for CS and CR are summarized in Table 4. The CS and CR time constants for **1-4** in toluene at 295 K are very similar. CS in **7** is comparable or faster than the instrument response function ($\tau_{\text{IRF}} = 0.15$ ps). CS of **2** and **3** in MTHF at 295 K is marginally slower than that of **1** and **4**. CS times in glassy MTHF at 80K are faster than at room

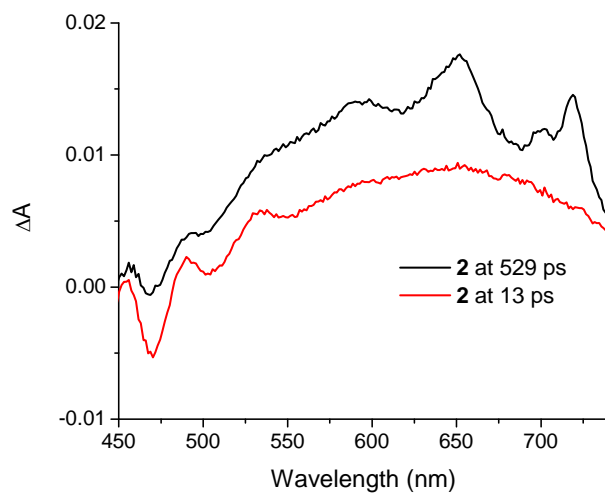


Figure 28 Transient absorption spectra of **2** at 295 K in toluene.

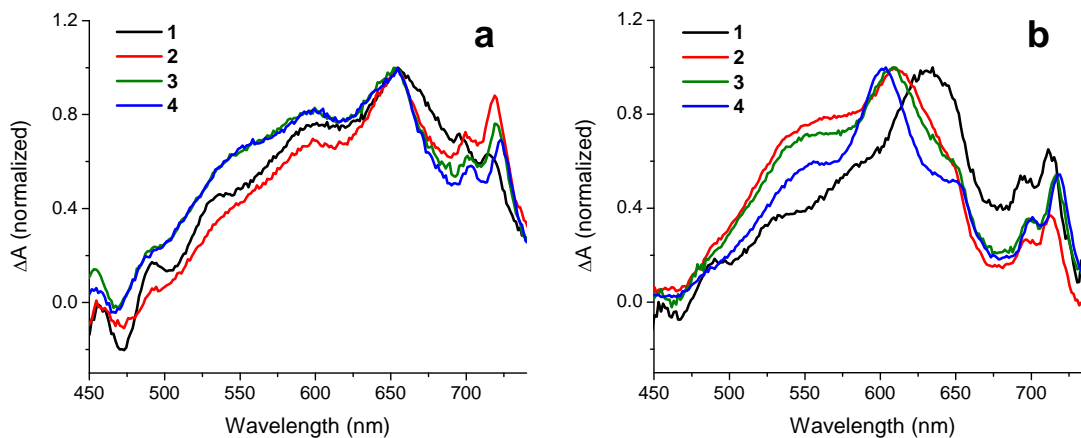


Figure 29 Transient absorption spectra of **1-4** at 295 K in a) toluene at 1029 ps and b) in MTHF at 239 ps

temperature, with CS in **1** occurring marginally faster than **2-4**. CR for **1-4** in MTHF at 295 K is too slow to be accurately measured using our ultrafast transient absorption apparatus, but too fast to be measured with our nanosecond transient absorption apparatus, ($\tau_{\text{IRF}} = 7$ ns), although the time constants are in the range of 2-4 ns.

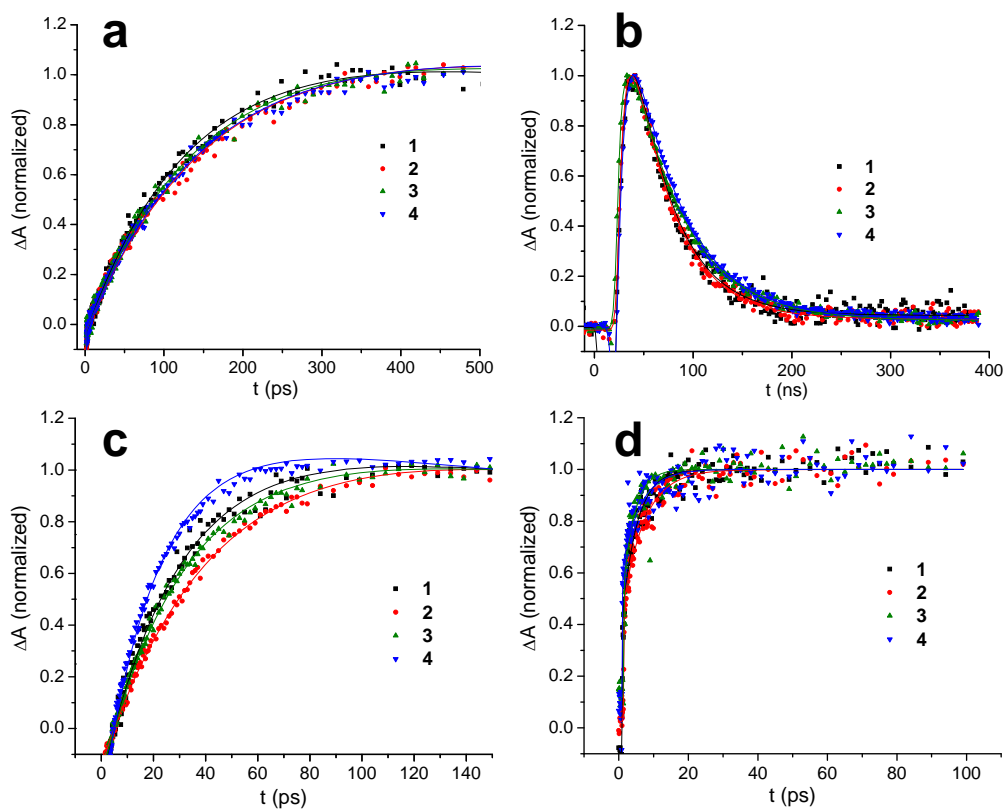


Figure 30 Transient absorption kinetics of 1-4 measured in a) toluene at 643 nm at 295 K b) toluene at 655 nm at 295 K c) MTHF at 613 nm at 295 K d) MTHF at 80K at 716 nm at 80 K

	τ_{CS} (toluene) (ps)	τ_{CR} (toluene) (ps)	τ_{CS} (MTHF 300K) (ps)	τ_{CS} (MTHF 80K) (ps)
1	130±12	48000±5000	27±3	2.5±1.6
2	145±17	45000±5000	44±5	6.5±1.0
3	133±5	54000±4000	33±3	3.9±1.9
4	141±10	55000±4000	22±4	6.7±2.7

Table 4 Electron transfer time constants in benzo-annulated BCO's

6.3 Discussion

Molecules **1-4** were designed to show the effect of an increasing number of π -pathways on the rate of charge transfer. Implicit in our design was the assumption that any π -pathway would significantly accelerate charge transfer over a σ -pathway. However, the essentially equal CS and CR rate constants of **1-4** show that the π system has no overall effect, contrary to our expectations from McConnell's expression. Clearly, the relative roles of the π - and σ -systems need to be re-examined.

The absence of an effect on the CS and CR rates of the bridge π -system is made additionally interesting by the work of Walton, Adcock and coworkers, which examined the hyperfine coupling between bridgehead radicals and functionality at the opposite bridgehead in bicyclo[2.2.2]octane and triptycene derivatives.²⁰³ They found significant hyperfine coupling

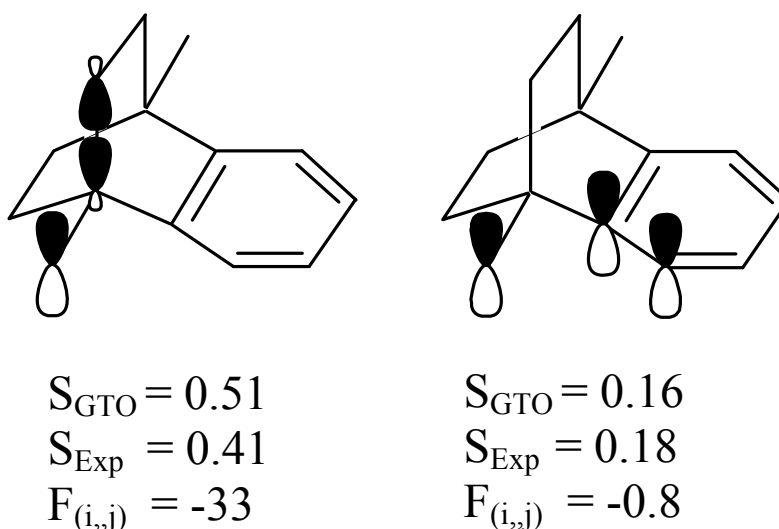


Figure 31 Relevant orbitals for overlap with the bridge σ and π systems. S refers to spatial overlap and F (mH) refers to the appropriate Fock matrix element

through the bicyclo[2.2.2]octane system to a variety of substituents at the other bridgehead, but found no coupling in the triptycene system for any of the substituents. Hyperfine couplings are communicated via the same superexchange type interactions that mediate electron transfer because the magnitude of the hyperfine coupling is proportional to the local population of the radical at that nucleus. Consequently, any model proposed for electronic interactions in our system must also be able to accommodate their results. Our expectation was that the π -pathways would *increase* communication between bridgehead anchored groups. Our experimental result is that the π -pathway has a negligible effect. However, their experiments suggest that the π -pathways *decrease* communication. Coupling is suggested to be mediated via overlap between a series of anti-periplanar sp^3 hybridized orbitals. Such an orientation is optimal for maximum overlap (Cieplak's model).^{204, 205}

6.3.1 Contribution of the Bridge π -System

The charge separation rate of **7** was significantly faster than in **1-4**, consistent with our expectations from Equation 6.1 and previous work¹² and showing that a conjugated π -system does provide greater electronic communication than a σ -system. To understand why our non-conjugated π -pathways failed to accelerate k_{CT} , we estimated the respective overlaps of the π system of the chromophores with the π and σ systems on the bridge, focusing on nearest and next-nearest neighbor interactions, as shown in Figure 31. We examine the overlap on a per “rung,” basis (i.e., though the σ system has three equivalent σ pathways, we will focus on one at a time where each rung is a set of two methylene carbons) as well as focusing on the impact of one additional phenyl ring at a time, as seen in Figure 31. The proximal alkyne p_π orbital will be considered the only point of communication between the chromophores and the bridge.

Hydrogen-like angular functions were used²⁰⁶ with two types of radial functions. We used the radial function of the slowest decaying carbon Gaussian-type orbital (GTO) for the 6-31G* basis set. This primitive had a decay constant of 0.48 \AA^{-2} . We also used a simple exponentially decaying radial function with a decay constant of 1.5 \AA^{-1} which was based on the calculated β distance parameter for the through-space distance dependence of electron transfer, 3 \AA^{-1} .¹⁷ Full calculation details including relevant bond angles are given in the Sample Calculations section. The overlap between the alkyne p orbital and the bridge σ system is only two to three times larger than the overlap with the marginally more distant π system, Figure 31.

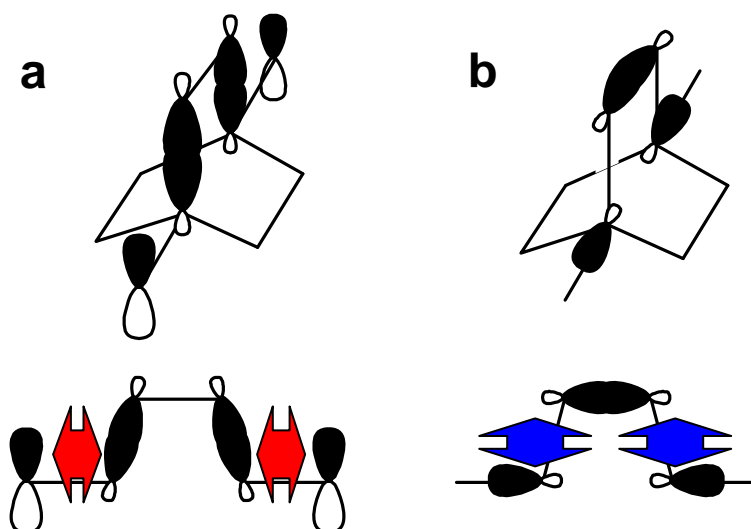


Figure 32 Application of Walton and Adcock's orbital overlap model²⁰³

We had hoped that this disparity would be overcome by the more favorable energy resonance condition resulting from the denominator of Equation 6.1 due to the communication being between two π systems.

We also undertook Natural Bond Orbital³⁶ (NBO) analysis to probe the significance of the interaction between the more distal π orbitals. By expressing the Fock matrix in the local

NBO basis, we can examine the appropriate off-diagonal elements to probe these specific microscopic interactions. Such an approach has been used to great advantage in pathways type analysis of transport in organic molecules.^{21, 33-35} In addition, direct examination of the matrix element avoids the use of a Mulliken “magic rule” type expression¹⁶ where the matrix element is assumed to be directly proportional to the orbital overlap, Equation 6.2,

$$V_{ij} = \langle \psi_i | H | \psi_j \rangle \propto S_{ij} = \langle \psi_i | \psi_j \rangle \quad (6.2)$$

where the ψ_i refer to the component wavefunctions.

In contrast to the simple analysis above, the NBO analysis shows a nearly vanishing matrix element between the alkyne and bridge π systems, Figure 31. Clearly, our application of Mulliken’s “magic rule” proportionality is shown to be an inadequate description for our system and suggests caution in the blanket application of Equation 6.2. The bridge π -system is effectively isolated from the π -systems of the chromophores. Additionally, the isolation of the π systems is corroborated by measurements of hyperfine couplings of a phosphorus centered radical of X-irradiated 9-phosphinotriptycene.²⁰⁷ The radical shows no hyperfine coupling to any part of the triptycene and only dipolar coupling to the phenyl hydrogens proximal to the phosphorus.

6.3.2 Contribution of the Bridge σ -System

If the matrix elements between the bridge π system and the chromophores are so small as to make the bridge π system effectively irrelevant, what is the origin of the dichotomy of the hyperfine couplings in Walton and Adcock’s²⁰³ results? The authors suggest the dominance of an anti-periplanar arrangement of σ -orbitals whereby the dominant communication conduit is the

σ -bond oriented parallel to the bridgehead radical orbital and the C-H bond of the opposite bridgehead, Figure 32a. The direct through-space interaction between the bridgeheads has been definitively shown to be irrelevant,⁴⁰ while this “skipped” through bond mechanism (as opposed to going through consecutive bonds) is supported by measurements of hyperfine couplings in related adamantane radicals, where the coupling constants to two geminal hydrogens would be equivalent in the case of consecutive through bond coupling, but are significantly different due to the presence of anti-periplanar overlap.²⁰⁸ Fusing the phenyl rings to the BCO changes the hybridization of this bond, removing an energetic resonance condition, and decreasing the effective mixing, consistent with McConnell’s relation, Equation 6.1. This explanation can be conveniently adapted to suit our system geometry, as shown in Figure 32b. Analogously, the p orbitals of the alkyne should be in good periplanar overlap with the σ bonds originating the bridgehead, which are in turn in good periplanar overlap with the σ bond at the opposite bridgehead, and sequentially, the p orbital at the opposite alkyne. Because this model suggests a minimal importance for the central σ orbital (3 in Table 5), a change in hybridization of this orbital would be predicted to have minimal effect on V_{eff} .



	No phenyl group	With phenyl group
ϵ_1	-269	-271
ϵ_2	-575	-603
ϵ_3	-576	-675
$F_{(1,2)}$	-33	-30
$F_{(1,3)}$	9.7	8.0
$F_{(1,4)}$	-1.5	-1.2
$F_{(1,5)}$	0.1	0.1
$F_{(2,3)}$	-119	-134
$F_{(2,4)}$	-30	-25
Direct		
$V_{\text{eff } 1,5}$	0.1	0.1
1 step		
$V_{\text{eff } 1,2,5}$	0.162	0.108
$V_{\text{eff } 1,3,5}$	0.306	0.158
$V_{\text{eff } 1,4,5}$	0.162	0.108
2 step		
$V_{\text{eff } 1,2,3,5}$	0.405	0.239
$V_{\text{eff } 1,2,4,5}$	-0.349	-0.206
$V_{\text{eff } 1,3,4,5}$	0.405	0.239
3 step		
$V_{\text{eff } 1,2,3,4,5}$	0.536	0.361
Total	1.729	1.108

Table 5 Parameters from NBO analysis. Energies given in mH. ϵ_i , $F_{(i,j)}$ $V_{\text{eff}(i,j,...)}$ refer to the numbered orbitals above. $V_{\text{eff}(i,j,...)}$ are calculated using Equation 6.1.

NBO analysis for the bonding orbitals of the bridge σ system is summarized in Table 5. The analysis captures the effect of the changing hybridization that accompanies the addition of the phenyl ring by showing a decrease in bonding orbital energy by almost 3 eV (100 mH) as

well as a shrinking of the off-diagonal Fock matrix elements between this NBO and other NBO's, consistent with higher s character. NBO analysis also captures the dominance of skipped through bond mixing over consecutive bond mixing in the antibonding orbitals (not shown), consistent with NBO analysis of BCO anions by Liang and Newton.³³ Charge transfer in our system is likely proceeding via a hole transfer mechanism because the electron acceptor is first locally excited, so we will focus on the bonding orbitals. However, mixing through the bonding orbitals shows comparable contributions from the skipped bond and consecutive bond mixing, again consistent with calculations on the cation.³³ Because of destructive interference among the pathways not involving the changing bond (NBO 3 in Table 5), the NBO analysis predicts that the majority of through bond communication involves this bond. Consequently, NBO analysis suggests significant contributions from NBO 3 to the total V_{eff} and an effect from the significant perturbation of that bond accompanying introduction of a phenyl group, and so does not support the model in Figure 32.

For clarity, we reemphasize that the multiple interactions we are currently referring to are interactions *within* a single rung of the bridge, and not between different rungs. We can suggest two possibilities for reconciling the NBO analysis and the experimental results.

One explanation simply restates that NBO analysis, though significantly informative, is ultimately qualitative in nature.³⁶ The importance of looking beyond nearest neighbors has been consistently shown,^{17, 33, 34} but the dominance of a single interaction may be overlooked by the NBO analysis. In this case, that interaction would necessarily not involve the central σ bond (NBO 3), and would preserve the above explanation.

Another explanation suggests that interference between different orbitals within the σ system (whether it be constructive or destructive) is real, but is being wiped out by electronic dephasing. Contributions from multiple spatial pathways require well defined phase relationships of the charge carrier wavefunction to be maintained at all sites along the multiple pathways. The fidelity of this phase relationship can be conveniently expressed as the off-diagonal element (coherence) of the density matrix. Fluctuations in site energies (as well as inter-site coupling) that exist at finite temperature can destroy these phase relationships^{48, 50} and spoil the legitimacy of summing pathways coherently.^{57, 135, 185} However, these fluctuations must occur on a sufficiently fast timescale to influence the additivity of the different pathways.

A convenient method of estimating this time threshold is by calculating the Landauer-Büttiker tunneling time,¹⁶⁹ a concept adapted for Donor-Bridge-Acceptor molecules by Nitzan and co-workers²⁵ and shown in Equation 6.3,

$$\tau_{\text{tun}} = \frac{\hbar N}{\Delta E} \quad (6.3)$$

where N is the number of bridge sites and ΔE is the energetic gap between the bridge and the D and A.

Conceptually, this is the time scale at which bridge fluctuations must occur in order to influence the charge carrier using the bridge. When the transfer is occurring via superexchange (large gap), fluctuations must be incredibly fast in order to influence the charge carrier. This is consistent with the charge carrier never actually occupying the bridge and being consequently decoupled from its fluctuation. On the other hand, charge transfer operating with small gaps or in the hopping regime should be responsive to relatively slow fluctuations, since the actual

occupation of the bridge makes the charge carrier more sensitive to fluctuations. With a gap of over 2 eV (as estimated from the ionization potentials of BCO, 9.5 eV,⁴² and PP, 7.2 eV²⁰⁹), the corresponding tunneling times of <2 fs would suggest that if any interference did exist, it would survive the electronic dephasing.

6.3.3 MTHF data at 300K

CS rates in MTHF show an increase over the toluene rates. This increase is consistent with the predictions of Marcus theory following the activation barrier in Table 3. In contrast to the charge separation rates in toluene, the rates measured in MTHF show a small, but experimentally reproducible difference in rates with **1** and **4** being slightly faster than **2** and **3**. While we had initially viewed this difference in rates as a consequence of the altered σ -system, a more likely explanation can be drawn from the transient absorption in spectra, Figure 29. While the spectra show only marginal differences in toluene, **1-4** show reproducible and relatively significant differences in MTHF. Since the ground state absorption shows no difference among **1-4**, and the rates measured in toluene are essentially equivalent, the changes in rates and spectra in MTHF are likely coming from changes in solvation of the ions in the radical pair.

Achieving the necessary solvent polarization is central to the Marcus theory of electron transfer,¹¹⁷ comprising the critical reaction coordinate in the original formulation of the electron transfer reaction. The first and second solvent shells provide the critical stabilization for the shifting charges.^{210, 211} The additional phenyl groups in **2-4** are located within the range of the first and second shells and so a consequent disruption of solvation seems reasonable. Such a steric disturbance of the solvent packing has previously been suggested to influence redox behavior.¹⁴⁸

The presence of the spectral shifts in MTHF but not toluene is also suggestive. Any solvation effect would be magnified in MTHF over toluene because of MTHF's higher dipole moment. However, toluene can still provide a stabilizing solvation environment via quadrupole interaction.²¹² One possibility for the difference in the spectra in the two solvents comes from the nature of the steric disturbance. The phenyl group annulated to the bridge will likely not provide a significant perturbation to the packing of the homologous toluene solvent. In contrast, the MTHF packing might be significantly altered and consequently show a bathochromic shift as bridge structure is altered. That the rate does not vary monotonically with additional phenyl groups as well as the observation that it is the two three-fold symmetric species that show the fastest rates suggest symmetry has a role maintaining optimal solvation. A similar non-monotonic trend also suggesting the importance of symmetry was seen in the relative rates of bromine abstraction at the bridgehead position of a similar series of molecules.⁸¹

6.3.4 MTHF data at 80 K

Evaluation of charge separation rates in a frozen glass serves two purposes. By reducing the population of high vibrational levels one can limit the conformational space explored by the molecule and learn about which conformations favor charge transfer. In addition, lowering the temperature may reduce the electronic dephasing rate enough to observe properties that rely on coherent summation of the charge carrier wavefunction over multiple spatially distinct parts of the molecule.^{135, 185} Despite frequently being referred to as rigid spacers, oligomeric alkynes can contort significantly at finite temperature.²¹³ Flexibility in D-B-A molecules can lead to the

electronic properties being dominated by conformations other than the equilibrium one. This scenario was seen in molecules where charge transfer is symmetry-forbidden^{45, 214} and is elegantly captured in the simulations of Jones, Carpenter, and Paddon-Row.²¹⁵

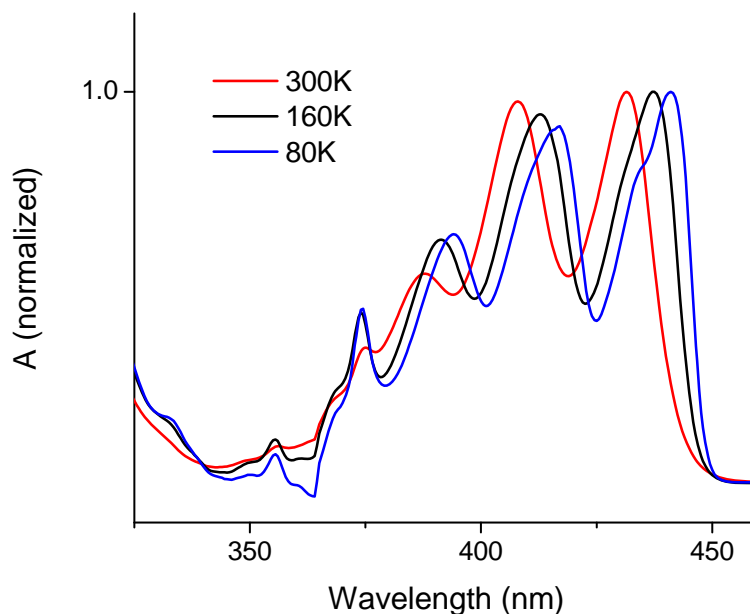


Figure 33 Steady-state UV-vis of **1** at a variety of temperatures in MTHF

The ground state absorption spectra of **1** are shown in Figure 33 at 300K, 160K and 80K. The sharpening of the features reveals two details about the system. First, though cyanoanthracene derivatives have been known to aggregate,^{129, 216} no aggregation occurs here as the absorption spectra show no evidence for the requisite exciton coupling¹¹⁸ that accompanies aggregation.²¹⁷ Second, the reduction in inhomogeneous broadening suggests that the ensemble of molecules is adopting fewer different conformations. This is consistent with depopulation of excited conformational modes before solidification. The sharpened features imply that the conformations under study in the glass are closer to the equilibrium conformation than in the solution phase.

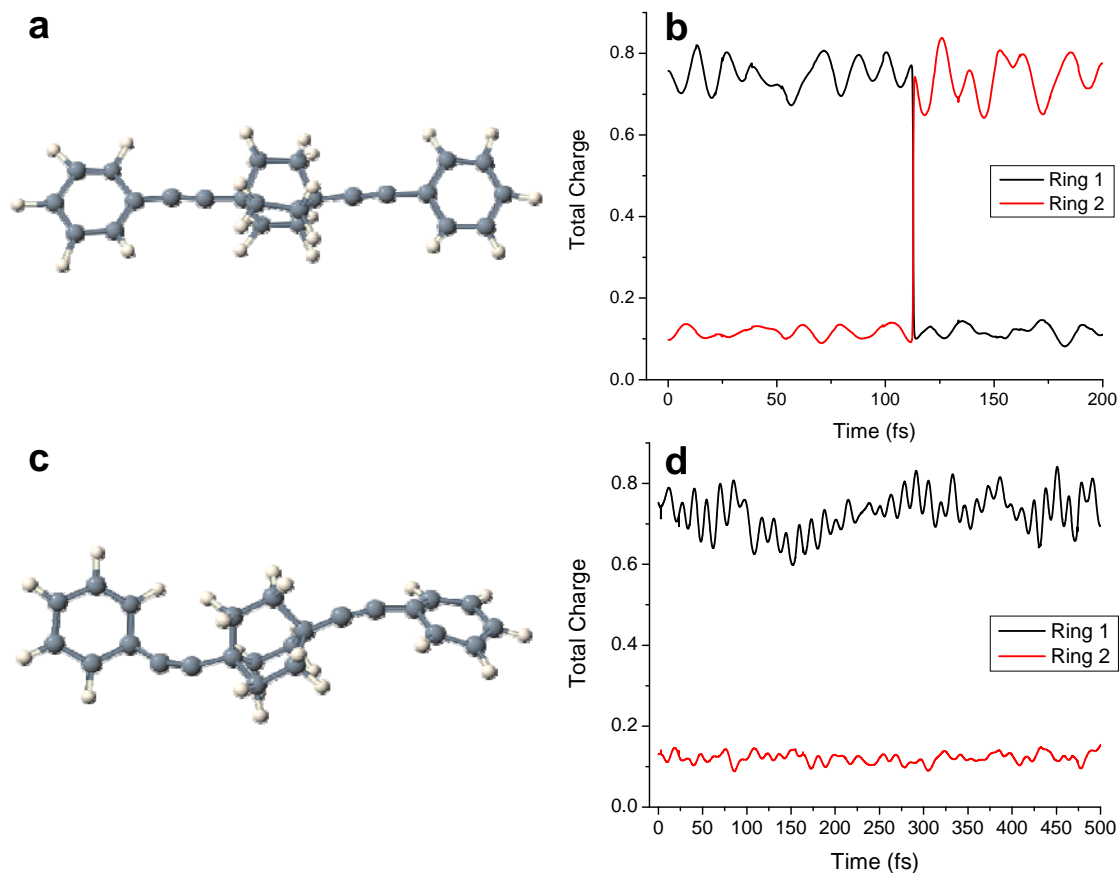


Figure 34 Charge transfer trajectories for a model of 1 at different effective temperatures. a) molecular dynamics snapshot with zero point energy (0K) in each of the modes and the trajectory b) showing charge shift. c) a molecular dynamics snapshot after equilibration at 300K with d) no charge shift in the trajectory

Molecules 1-4 all show significantly faster charge separation rates upon freezing. Such behavior is reminiscent of the bacterial photosynthetic reaction center.^{5, 52} In that case the rate acceleration was explained as higher vibrations taking the system away from the bottom of the vibronic well, the optimal position for activationless charge transfer.¹¹ However, non-vanishing activation energies, Table 3, suggest this explanation is not valid in our system. More likely, the rise in CS rate is due to a conformational gating effect,^{45, 101, 108, 214} whereby the deviations from equilibrium conformation result in a reduction of V_{eff} . These less efficient conformations are accessed more frequently at 300K than at 80K. To test this hypothesis we followed the example of Jones and coworkers²¹⁸ and performed molecular dynamics coupled with semiempirical

calculations to follow the charge transfer trajectories. Our simulated molecule is a model of **1** with a +1 charge, Figure 34. When only the zero-point energy was injected into the normal modes of the computational model system ($T=0\text{K}$), only geometries close to the equilibrium geometry were observed, Figure 34a, and a charge shift occurred within several hundred femtoseconds of the simulation, Figure 34b. In contrast, when additional energy was put into the system ($T=300\text{K}$), the geometry deviated significantly from the equilibrium position, Figure 11c, and charge shift was never observed, Figure 34d. These simulations confirm our hypothesis regarding the increased efficacy of the equilibrium conformation. An additional report detailing specific per-mode contributions is in progress.

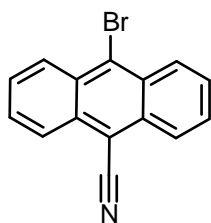
The charge separation rate of **1** is seen to be marginally faster than **2-4**, although differences among **2-4** are difficult to probe due to degradation of the sample experienced and the consequent size of the error bars. The relative steric bulk of **2-4** compared to **1** may also play a role in how the molecule interacts with the MTHF matrix. Since the trend here is loosely similar to that observed in solution and steric effects have been shown to be important, it is difficult to suggest that a lower electronic dephasing rate due to the lower temperature is a significant factor in the glass.

6.4 Conclusion

We have prepared a novel series of molecules to test the effect of additional π -pathways fused to a σ -scaffold on mediating electron transfer between two chromophores. Surprisingly, the π -pathways were shown to have no role in the electron transfer, with all important communication occurring via the σ -system. This behavior was also surprising, considering the work of Walton, Adcock, and co-workers, who saw large changes in the ability of a σ -system to

mediate electronic communication with the addition of fused π -pathways due to the changes in hybridization of the σ -bond orbitals. We were able to adapt their qualitative physical organic explanation to explain the dichotomy of our two systems. However, NBO analysis did not corroborate this rationale, either because of its own qualitative nature or because of the importance of electronic dephasing in effectively preventing the coherent addition of multiple σ -pathways. Charge separation rates in MTHF showed some differences between members of the series but were likely caused by differences in solvation. Charge separation rates increased at lower temperatures because deviations from equilibrium conformation experienced more severely at high temperatures decrease the electronic communication. This behavior was captured in molecular dynamics simulations coupled to semiempirical electronic structure calculations.

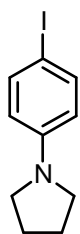
6.5 Synthesis



10-Bromo-anthracene-9-carbonitrile¹⁹¹ 500 mg (1.48 mmol) of 9,10

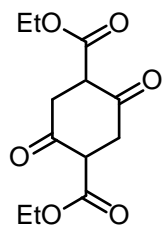
dibromoanthracene and 133 mg (1.48 mmol) of CuCN (CAUTION, keep away from water) were combined in a round bottom flask with 20 mL of DMF. The mixture was put under N₂ and refluxed for 6 hours and left to cool overnight. The DMF was distilled off under vacuum and after cooling, chloroform with a few drops of triethylamine were added. The solid was washed

thoroughly with multiple aliquots of chloroform. The combined fractions were then passed through a silica plug and dried to yield a crude solid. Column chromatography on 100 mg portions of the crude material in 1:1 hexanes:chloroform yielded the pure compound (35%). ^1H NMR (CDCl_3) δ : 8.60 (d, $J=9.4$ Hz, 2H), 8.44 (d, $J=9.4$ Hz, 2H), 7.75 (t, $J=7.6$ Hz, 2H) 7.70 (t, $J=7.6$ Hz, 2H)



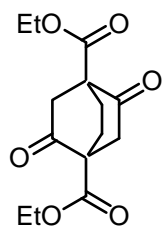
1-(4-Iodo-phenyl)-pyrrolidine¹⁹⁰ Following literature procedure, 4.38 g (20.2 mmol) of p-iodoaniline, 4.31 g (20.0 mmol) of dibromobutane and 5.16 g (39.9 mmol) of diisopropylethylamine were combined with 10 mL of benzene and heated at 50 °C for 18 hours and at reflux for 12 hours. The reaction mixture was cooled and the precipitate was filtered off and washed with 2M NaOH. The solid was then recrystallized from ethanol to yield white crystals (19%). The material could be additionally purified by dissolving in 1:1 chloroform:hexanes and passing through a silica plug (19%).

^1H NMR (CDCl_3) δ : 7.44 (d, $J=9.0$ Hz, 2H), 6.33 (d, $J=9.0$ Hz, 2H), 3.24 (t, $J=6.6$ Hz, 4H) 2.00 (t, $J=6.6$ Hz, 4H)



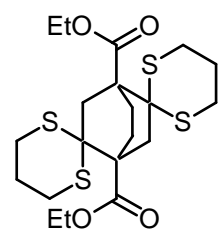
Diethyl 2,5-Dioxocyclohexane-1,4-dicarboxylate^{192, 219} The Dieckmann

condensation from diethylmalonate was enacted following literature procedures. The product was isolated in 55% yield. ¹H NMR (CDCl₃) δ: 12.19 (s, 2H), 4.23 (q, J=7.14 Hz, 4H), 3.17 (s, 4H), 1.31 (t, J=7.14 Hz, 6H) ¹³C NMR (CDCl₃) δ: 171.26, 168.38, 93.20, 60.71, 28.48, 14.19



2,5-Dioxo-bicyclo[2.2.2]octane-1,4-dicarboxylic acid diethyl ester^{192, 220} The ester

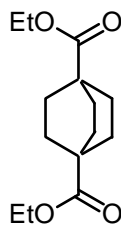
was formed from diethyl 2,5-Dioxocyclohexane-1,4-dicarboxylate via literature procedure⁹⁹ in 71% yield. ¹H NMR (CDCl₃) δ: 4.14 (q, J=7.14 Hz, 4H), 3.08 (d, J=2.6 Hz, 2H) 3.05 (d, J= 2.6 Hz, 2H), 2.73 (s, 2H), 2.69 (s, 2H), 1.29 (t, J=7.14 Hz, 6H) ¹³C NMR (CDCl₃) δ: 203.89, 168.84, 62.07, 57.49, 42.08, 24.71, 14.31



Diethyl 2,5-bisdithianebicyclo[2.2.2]octane-1,4-dicarboxylate^{99, 192} The

thiane was formed from the diketone via literature procedures⁹⁹ in 80% yield. Excess thiol could be removed without excessive lab contamination by washing with dilute aqueous KOH. ¹H

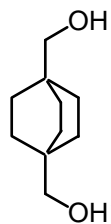
NMR (CDCl₃) δ : 4.23 (m, 4H), 3.25 (m, 1H), 3.22 (m, 1H), 3.14-3.07 (m, 4H), 2.85 (m, 1H), 2.82 (m, 1H), 2.79 (m, 1H), 2.76 (m, 1H), 2.74 (s, 1H), 2.71 (s, 1H), 2.66-2.59 (m, 2H), 2.09 (m, 2H), 1.99-1.83 (m, 4H), 1.32 (t, J=7.1 Hz, 6H) ¹³C NMR (CDCl₃) δ 172.32, 61.28, 53.59, 49.53, 43.94, 27.17, 27.12, 25.04, 23.83, 14.21



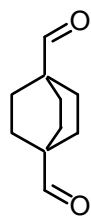
Diethyl Bicyclo[2.2.2]octane-1,4-dicarboxylate^{99, 192} 50 g of Raney nickel was measured out (while still in a water suspension) via weighing by difference. The nickel was then activated (CAUTION, dry Raney nickel is extremely flammable). The water was decanted off and replaced with absolute ethanol. The ethanol was then decanted off and replaced with fresh ethanol. This process was repeated (about 6 times) until a small aliquot of the nickel from the tip of a pipette, after drying on a paper towel, ignited. A magnet was used to keep the nickel at the bottom of a test tube during this process. The slurry in ethanol along with 400 mL of additional ethanol was then added to a round bottom flask equipped with a mechanical stirrer. 6 g of the thiane (13 mmol) was added and the system was thoroughly put under N₂. The reaction mixture was heated at incipient reflux for 3 days and then allowed to cool. The solution was decanted and fresh ethanol was added to the remaining nickel slurry. The slurry was sonicated and the solution decanted and combined with the previous fractions. The combined fractions were put through a ceelite plug and dried to yield an oil and a yellow-green solid. Chloroform was added and the solid was filtered off. The chloroform was washed with water and dried to yield the product in 98% yield. The remaining nickel slurry was quenched by slow addition of the slurry

to a large volume of bleach. $^1\text{H NMR}$ (CDCl_3) δ : 4.08 (d, $J=6.9$ Hz, 4H), 1.79 (s, 12H),

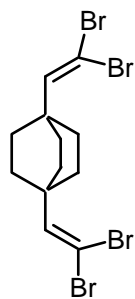
1.22(t, $J=6.9$ Hz, 6H)



Bicyclo[2.2.2]octane-1,4-dimethanol¹⁹² Following literature procedure, the diester was reduced to the diol in 89% yield. $^1\text{H NMR}$ (CDCl_3) δ : 3.27 (s, 4H), 1.42 (s, 12H)



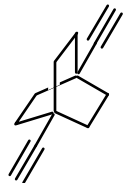
Bicyclo[2.2.2]octane-1,4-dicarboxaldehyde¹⁹² Following literature procedure, the diol was oxidized to the dialdehyde via Swern oxidation in quantitative yield and was quickly used for the next step. $^1\text{H NMR}$ (CDCl_3) δ : 9.47 (s, 2H), 1.71 (s, 12H)



1,4-Bis-(2,2-dibromo-vinyl)-bicyclo[2.2.2]octane Following a modification of a previous procedure,¹² 3.87 g (11.67 mmol) of carbon tetrabromide, 3.06 g (11.68 mmol) of triphenylphosphine, and 0.77 g (11.8 mmol) of Zn powder were combined and put under N_2 . 34 mL of dry dichloromethane was added and the mixture was left to stir for 24 hours. 488 mg (2.94 mmol) of bicyclo[2.2.2]octane-1,4-dicarboxaldehyde in 1 mL of dichloromethane was added via syringe and the mixture was allowed to stir for another 24 hours. 37 mL of hexanes was then added and the slurry was filtered through a plug of silica to yield the product (53%), which was

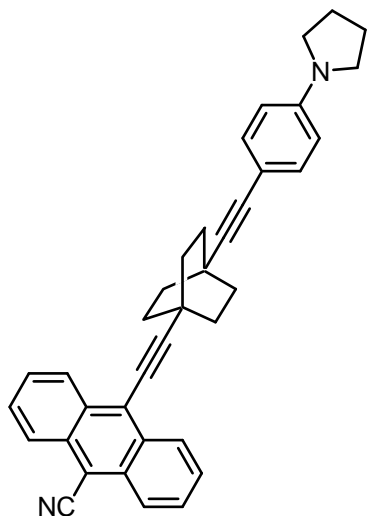
unstable and quickly used in the next step. ^1H NMR (CDCl_3) δ : 6.41 (s, 2H), 1.82 (s, 12H)

^{13}C NMR (CDCl_3) δ : 145.49, 85.65, 35.73, 29.71



1,4-bis-(ethynyl)-bicyclo[2.2.2]octane²²¹ Following a modification of a

literature procedure,¹² 740 mg (1.55 mmol) of 1,4-bis-(2,2-dibromo-vinyl)-bicyclo[2.2.2]octane was dissolved in 17 mL of dry THF under N_2 and cooled to $-78\text{ }^\circ\text{C}$. 4.52 mL of a 1.6M solution of n-butyllithium was added and the solution was allowed to stir for 1 hour while at $-78\text{ }^\circ\text{C}$ followed by 1.5 hours at room temperature. The reaction was then quenched with water. Hexanes was added to the resulting suspension and the organic layer was separated, repeatedly washed with water, and dried with sodium sulfate. Solvent was evaporated (CAUTION, the material sublimes under vacuum at elevated temperatures) and the material was purified via column chromatography (2:8 dichloromethane:hexanes) to yield the dialkyne (76%). ^1H NMR (DCM) δ : 2.08 (s, 2H), 1.77 (s, 12H) ^{13}C NMR (CDCl_3) δ : 90.95, 68.14, 31.54, 25.97

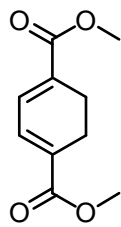


10-[4-(4-Pyrrolidin-1-yl-phenylethynyl)-bicyclo[2.2.2]oct-1-

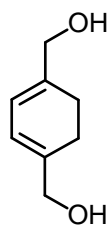
ylethynyl]-anthracene-9-carbonitrile (1) 5 mg (0.032 mmol) of (1-4-diethynyl-

bicyclo[2.2.2]octane, 5 mg (0.018 mmol) of 1-(4-Iodo-phenyl)-pyrrolidine (columned immediately before use), 5 mg (0.004 mmol) of tetrakis(triphenylphosphine)palladium and a pipette tip of CuI were combined in a round bottom flask and put under N₂. 1.5 mL of piperidine (distilled from CaH₂ and sparged with N₂) was added and the reaction was closely monitored by TLC (1:1 hexanes:chloroform). After approximately 15 minutes, the reaction mixture was poured onto diethylether and washed repeatedly with water. The organic fraction was dried (sodium sulfate) and the solvent was removed. (CAUTION, the product decomposes with heat >60°C or if put onto silica). The crude product was then combined in a round bottom with 5 mg (0.018 mmol) of 9-bromo-10-cyanoanthracene, 2 mg (0.003 mmol) of bis(triphenylphosphine)palladiumdichloride, and a pipette tip of CuI and put under N₂. 3 mL of triethylamine (distilled from CaH₂) was added and the reaction was refluxed overnight. After cooling the solvent was removed and the crude mixture was passed through a plug of silica (deactivated with triethylamine). The crude mixture (3 mg) was then purified in small portions via preparatory scale reverse phase (C18) thin layer chromatography (1:1 hexanes:dichloromethane) to obtain the product in 9% yield. The product was easily followed as the only visible yellow spot. Additional purification was accomplished with preparatory HPLC (silica column) with a 3:97 acetonitrile:chloroform eluent.

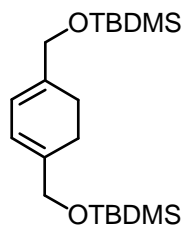
¹H NMR (CD₂Cl₂) δ: 8.58 (d, J=9.3 Hz, 2H), 8.38 (d, J=8.4 Hz, 2H), 7.73 (m, 2H), 7.65 (m, 2H), 7.18 (d, J=8.6 Hz, 2H), 6.43 (d, J=8.6 Hz, 2H), 3.25 (m, 4H), 2.11 (m, 4H), 1.98 (m, 12H)
ESI-HRMS (m/z) [M]⁺ calcd for C₃₇H₃₃N₂, 504.25655; found, 504.25663.



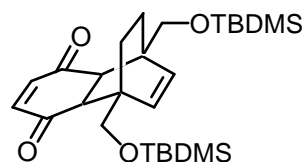
Cyclohexa-1,3-diene-1,4-dicarboxylic acid dimethyl ester¹⁹⁴ The diester was synthesized from cyclohexane 1,4-dicarboxylic acid via literature procedure in 22% yield.



(4-Hydroxymethyl-cyclohexa-1,3-dienyl)-methanol¹⁹⁵ Following literature procedures, the diester was reduced with DIBALH in 42% yield. The product was unstable and immediately used for the next step. ¹H NMR (CDCl₃) δ: 5.81 (s, 2H), 4.04 (s, 4H), 2.14 (s, 4H)

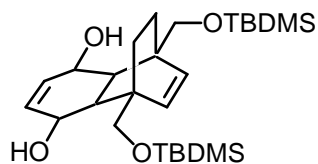


1,4-Bis-(tert-butyl-dimethyl-silyloxymethyl)-cyclohexa-1,3-diene The crude diol (1.5 mmol) was combined with 670 mg (4.5 mmol) of TBDMSCl and 612 mg (9 mmol) of imidazole in 5 mL of DMF and stirred overnight. The solvent was removed and the material was passed through a silica plug (dichloromethane). The isolated material (90%) was quickly used for the next step. ¹H NMR (CDCl₃) δ: 5.86 (s, 2H), 4.13 (s, 4H), 2.13 (s, 4H), 0.91 (s, 18H), 0.07 (s, 12H)



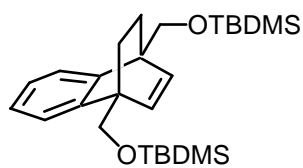
1,4,4a,8a-Tetrahydro-1,4-bis-(tert-butyl-dimethyl-silyloxymethyl)-1,4-ethanonaphthalene-5,8-dione 100 mg (0.25 mmol) of the protected diene and 270 mg

(2.5 mmol) of p-benzoquinone were refluxed in 10 mL of toluene for 24 hours. The solvent was removed and much of the excess p-benzoquinone was sublimed off. The crude reaction mixture was purified via column chromatography (8:2 hexanes: chloroform) to yield the product (83%). ^1H NMR (CDCl_3) δ : 6.52 (s, 2H), 6.09 (s, 2H), 3.78 (m, 4H), 2.93 (s, 2H), 1.59 (m, 2H), 1.34 (m, 2H), 0.89 (s, 18H), 0.07 (d, $J=6.4$ Hz, 12H) ^{13}C NMR (CDCl_3) δ : 198.85, 142.23, 133.44, 65.85, 52.71, 45.41, 29.82, 25.88, 18.35, -5.55 ESI-HRMS (m/z) $[\text{M}]^+$ calcd for $\text{C}_{26}\text{H}_{45}\text{O}_4\text{Si}_2$, 476.27781; found, 476.27773.



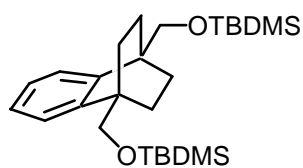
1,4,4a,8a-Tetrahydro-1,4-bis-(tert-butyl-dimethyl-silyloxymethyl

)-1,4-ethanonaphthalene-5,8-diol Following a variant of a literature procedure,²³ 3.02 g (6.33 mmol) of the dione was dissolved in 140 mL of a 1:1 mixture of methanol and DCM. 22.4 g (0.06 mmol) of cerium chloride heptahydrate was added and the mixture was cooled to 0°C. 1.44 g (0.038 mmol) of NaBH_4 was then slowly added. The mixture was then stirred for 3 hours at room temperature before being poured onto cold water. The material was extracted into dichloromethane, washed with water, brine, and dried with sodium sulfate. After the solvent was removed the resulting material (quantitative reaction yield) was used without purification for the next step. ^1H NMR (CDCl_3) δ : 6.42 (m, 2H), 6.13 (s, 2H), 4.24 (s, 2H), 3.92-3.70 (m, 4H), 2.00 (s, 2H), 1.53 (d, $J=7.3$ Hz 2H), 1.12 (d, $J=7.3$ Hz, 2H), 0.91 (s, 18H), 0.10 (s, 12H) ^{13}C NMR (CDCl_3) δ : 135.82, 131.55, 67.38, 62.67, 48.73, 42.77, 30.82, 25.85, 18.25, -5.60



1,4-bis-(tert-butyl-dimethyl-silyloxymethyl)-1,4-

ethanonaphthalene Following a variant of a previous procedure,¹⁹⁶ 3.04 g (6.033 mmol) of the diol was dissolved in 18 mL of pyridine (distilled from CaH₂) and cooled to 0°C. 4.86 g (2.9 mL) of POCl₃ was added dropwise and the solution was allowed to stir at room temperature for 3 days, after which it was refluxed for 1 hour before being cooled and poured onto ice water. The suspension was then extracted with hexanes, washed with water, 15% HCl, and more water. After drying over sodium sulfate, the material was passed through a plug of silica to yield the product in 68% yield. ¹H NMR (CDCl₃) δ: 7.23 (m, 2H), 7.10 (m, 2H), 6.39 (s, 2H), 4.34-4.21 (m, 4H), 1.62 (m, 2H), 1.37 (m, 2H), 0.94 (s, 18H), 0.16 (s, 12H) ¹³C NMR (CDCl₃) δ: 145.36, 136.31, 124.40, 120.46, 65.19, 47.61, 29.89, 25.93, 18.38, 1.01 ESI-HRMS (m/z) [M]⁺ calcd for C₂₆H₄₅O₂Si₂, 444.28798; found, 444.28867.

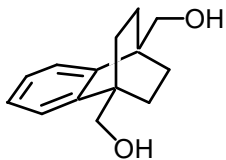


1,2,3,4-tetrahydro-1,4-bis-(tert-butyl-dimethyl-silyloxymethyl)-

1,4-ethanonaphthalene 45 mg (0.1 mmol) of 1,4-bis-(tert-butyl-dimethyl-silyloxymethyl)-1,4-ethanonaphthalene was dissolved in 26 mL of a 3:1 mixture of ethanol and benzene. 60 mg of 10% Pd/C was added and the mixture was shaken in a Parr shaker for 12 hours under approximately 45 psi of H₂. The suspension was passed through a plug of silica to give the product in 90% yield. ¹H NMR (CDCl₃) δ: 7.29 (m, 2H), 7.20 (m, 2H), 3.95 (s, 4H), 1.68 (d,

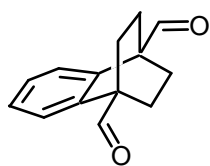
$J=7.2$ Hz, 2H), 1.31 (d, $J=7.2$ Hz, 2H) 0.92 (s, 18H), 0.11 (s, 12H) ^{13}C NMR (CDCl_3) δ :

144.09, 125.22, 121.56, 67.73, 40.25, 28.63, 25.93, 18.35, -5.49



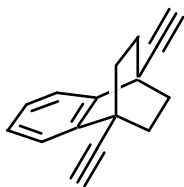
1,2,3,4-tetrahydro-1,4-bis-(hydroxymethyl)-1,4-ethanonaphthalene 41 mg

(0.09 mmol) of 1,2,3,4-tetrahydro-1,4-bis-(tert-butyl-dimethyl-silyloxymethyl)-1,4-ethanonaphthalene was dissolved in 1 mL of dry THF. 2 mL of a 1 M solution of TBAF (prepared several hours before from solid TBAF hydrate dissolved in THF and left to stand on 4Å sieves) was added and the solution was allowed to stir overnight. Diethyl ether was added the solution was washed with water. The solution was dried over sodium sulfate and evaporated to yield the product in 95% yield. ^1H NMR (CDCl_3) δ : 7.32 (m, 2H), 7.26 (m, 2H), 4.05 (s, 4H), 1.74 (d, 4H), 1.38 (d, 4H) ^{13}C NMR (CDCl_3) δ : 143.32, 125.91, 121.33, 67.66, 40.12, 28.38 EI-HRMS (m/z) $[\text{M}]^+$ calcd for $\text{C}_{14}\text{H}_{18}\text{O}_2$, 218.1302; found, 281.1309.



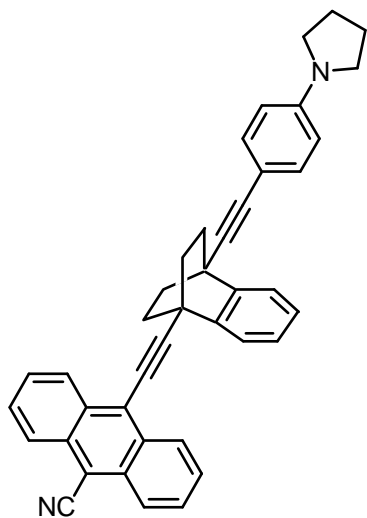
1,2,3,4-tetrahydro-1,4-ethanonaphthalene-1,4-bis-(carboxaldehyde) 50 mg

(0.23 mmol) of the diol was dissolved in 10 mL of DCM. 300 mg of pyridinium chlorochromate (PCC) was added and the mixture was stirred for 24 hours. The reaction mixture was poured onto a plug of silica and eluted with DCM. The product (73%) was clean by NMR and used without further purification for the next reaction. ^1H NMR (CDCl_3) δ : 10.22 (s, 2H), 7.30 (m, 2H), 7.24 (m, 2H), 1.91 (d, 4H), 1.76 (d, 4H) ^{13}C NMR (CDCl_3) δ : 203.77, 139.87, 126.98, 121.88, 50.05, 26.09



1,4-bis-(ethynyl)-benzobicyclo[2.2.2]octane 42 mg (0.2 mmol) of the

dialdehyde, 98 mg (0.51 mmol) of freshly columned dimethyl-1-diazo-2-oxopropylphosphonate (Bestmann's reagent, prepared by literature procedure²²²), and 110 mg (0.8 mmol) of K_2CO_3 was combined in a flask and put under N_2 . 3 mL of MeOH (distilled from CaH_2) was then added and the reaction was left to stir for 5 hours. Diethyl ether was then added and the solution was washed with water, 5% $NaHCO_3$, more water and was dried over sodium sulfate. After removal of solvent, the product (87%) was pure by NMR and was used for the next step. 1H NMR ($CDCl_3$) δ : 7.63 (m, 2H), 7.33 (m, 2H), 2.52 (s, 2H), 2.11 (d, 4H), 1.64 (d, 4H) ^{13}C NMR ($CDCl_3$) δ 139.84, 126.82, 122.52, 86.30, 72.79, 34.87, 33.08 EI-HRMS (m/z) $[M]^+$ calcd for $C_{16}H_{14}$, 206.1090; found, 206.1093.

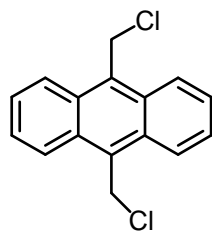


10-[4-(4-Pyrrolidin-1-yl-phenylethynyl)-benzobicyclo[2.2.2]oct-

1-ylethynyl]-anthracene-9-carbonitrile (2) 23 mg (0.11 mmol) of (1-4-diethynyl-benzobicyclo[2.2.2]octane, 16 mg (0.06 mmol) of 1-(4-Iodo-phenyl)-pyrrolidine (columned

immediately before use), 12 mg (0.004 mmol) of tetrakis(triphenylphosphine)palladium and a pipette tip of CuI were combined in a round bottom flask and put under N₂. 1.5 mL of piperidine (distilled from CaH₂ and sparged with N₂) was added and the reaction was closely monitored by TLC (1:1 hexanes:chloroform). After approximately 15 minutes, the reaction mixture was poured onto diethylether and washed repeatedly with water. The organic fraction was dried (sodium sulfate) and the solvent was removed. (CAUTION, the product decomposes with heat >60°C or if put onto silica). The crude product was then combined in a round bottom with 20 mg (mmol) of 9-bromo-10-cyanoanthracene, 2 mg of bis(triphenylphosphine)palladiumdichloride, and a pipette tip of CuI and put under N₂. 10 mL of triethylamine (distilled from CaH₂) was added and the reaction was refluxed overnight. After cooling the solvent was removed and the crude mixture was passed through a plug of silica (deactivated with triethylamine). The crude mixture (14 mg) was then purified in small portions via preparatory scale reverse phase (C18) thin layer chromatography (1:1 hexanes:dichloromethane) to obtain the product in 5% yield. Additional purification was accomplished with preparatory HPLC (silica column) with a 3:97 acetonitrile:chloroform eluent.

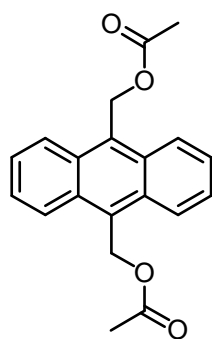
¹H NMR (CD₂Cl₂) δ: 8.74 (d, J=10.1 Hz, 2H), 8.44 (d, J=9.4 Hz, 2H), 7.81 (d, J=6.8 Hz, 1H), 7.76 (m, 2H+1H), 7.70 (m, 2H), 7.36 (m, 2H+2H), 6.51 (d, J=9.2 Hz, 2H), 3.29 (m, 4H), 2.47 (m, 2H), 2.31 (m, 2H), 1.99 (m, 4H+2H), 1.80 (m, 2H) ESI-HRMS (m/z) [M]⁺ calcd for C₄₁H₃₂N₂, 552.25655; found, 552.25673.



9,10-Bis-chloromethyl-anthracene¹⁹⁸ The product was prepared from

anthracene via literature procedures in 50% yield and recrystallized from toluene. ¹H NMR

(CDCl₃) δ: 8.39 (m, 4H), 7.66 (m, 4H), 5.62 (s, 4H)

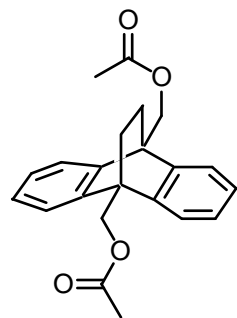


9,10-bis(acetoxymethyl)-anthracene¹⁹⁹ The product was prepared from 9,10

bis-chloromethylanthracene via literature procedure in 78% yield and recrystallized from

benzene. ¹H NMR (CDCl₃) δ: 8.4 (m, 4H), 7.6 (m, 4H), 6.16 (s, 4H), 2.10 (s, 6H) ¹³C NMR

(CDCl₃) δ: 171.16, 130.69, 128.64, 126.32, 124.61, 58.73, 20.94

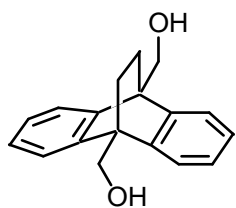


9,10-bis(acetoxymethyl)-9,10-ethanoanthracene²²³ The product was prepared

following variant²⁰¹ of literature procedures. The reactions was performed in a glass-lined high

pressure reactor (150 ml) equipped with stirring bar. The reactor was charged with 2 g of the anthracene derivative and 10 ml of dry toluene inside a nitrogen filled glove box. The reactor was then removed from the box and pressurized with 1100 psi of ethane (polymerization grade, MG industries) and immersed in a preheated oil bath at 190 C for 96 h. After completion of the reaction the solvent was removed under reduced pressure and the obtained white solid was dried under high vacuum. The material was pure by NMR and isolated in quantitative yield.

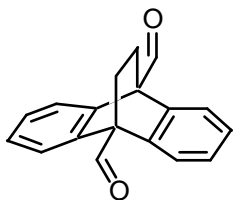
^1H NMR (CDCl_3) δ : 7.26 (m, 4H), 7.17 (m, 4H), 5.14 (s, 4H), 2.18 (s, 6H), 1.75 (s, 4H) ^{13}C NMR (CDCl_3) δ : 171.32, 142.94, 125.75, 121.29, 65.10, 45.03, 29.75, 21.02



9,10-bis(hydroxymethyl)-9,10-ethanoanthracene²²³ Following literature

procedures, a mixture of 1 g (2.9 mmol), 0.7 g KOH, 7 mL EtOH, and 0.7 mL water was refluxed under N_2 for 20 hours. After cooling, the solvent was removed under reduced pressure. The solid was suspended in DCM and 10% HCl was added the suspension was shaken vigorously. The organic part was washed with more acid, then water, then brine and dried over sodium sulfate. The solvent was then removed under reduced pressure to yield the product in 93% yield.

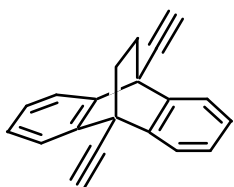
^1H NMR (CDCl_3) δ : 7.44 (m, 4H), 7.18 (m, 4H), 4.74 (d, $J=5.2$ Hz, 4H), 1.82 (t, $J=5.2$ Hz, 2H), 1.71 (s, 4H) ^{13}C NMR (CDCl_3) δ : 143.72, 125.65, 121.50, 64.19, 40.69, 29.72



9,10-ethanoanthracene-9,10-carbaldehyde 0.39 g (1.5 mmol) of the

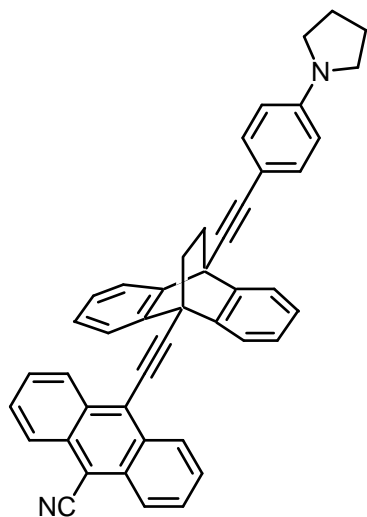
diol and 2 g (9.3 mmol) of pyridinium chlorochromate (PCC) were combined in 30 mL of DCM and stirred for 24 hours. The reaction mixture was poured onto a plug of silica and eluted with DCM. The product (56%) was clean by NMR and used without further purification for the next reaction

NMR (CDCl₃) δ : 10.74 (s, 2H), 7.25 (m, 4H), 7.08 (m, 4H), 1.80 (s, 4H) ¹³C NMR (CDCl₃) δ : 202.64, 140.51, 126.38, 121.74, 55.75, 26.96



9,10-bis(ethynyl)-9,10-ethanoanthracene 26 mg (0.1 mmol) of the

dialdehyde, 50 mg (0.26 mmol) of freshly columned dimethyl-1-diazo-2-oxopropylphosphonate (Bestmann's reagent, prepared by literature procedure²²²), and 55 mg (0.4 mmol) of K₂CO₃ was combined in a flask and put under N₂. 3 mL of MeOH (distilled from CaH₂) was then added and the reaction was left to stir for 5 hours. Diethyl ether was then added and the solution was washed with water, 5% NaHCO₃, more water and was dried over sodium sulfate. After removal of solvent, the product (92%) was pure by NMR and was used for the next step. NMR (CDCl₃) δ : 7.79 (m, 4H), 7.31 (m, 4H), 3.00 (s, 2H), 2.09 (m, 4H) ¹³C NMR (CDCl₃) δ : 140.53, 126.42, 122.14, 82.00, 77.14, 43.60, 34.91 EI-HRMS (m/z) [M]⁺ calcd for C₂₀H₁₄, 254.1090; found, 254.1097.



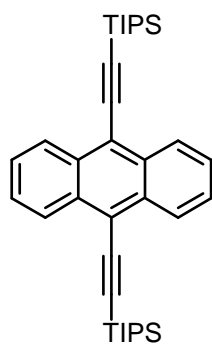
10-[4-(4-Pyrrolidin-1-yl-phenylethynyl)-

dibenzobicyclo[2.2.2]oct-1-ylethynyl]-anthracene-9-carbonitrile (3) 8 mg (0.03 mmol) of (9-10-diethynyl-benzobicyclo[2.2.2]octane, 5 mg (0.02 mmol) of 1-(4-Iodo-phenyl)-pyrrolidine (columned immediately before use), 5 mg (0.004 mmol) of tetrakis(triphenylphosphine)palladium and a pipette tip of CuI were combined in a round bottom flask and put under N₂. 0.5 mL of piperidine (distilled from CaH₂ and sparged with N₂) was added and the reaction was closely monitored by TLC (1:1 hexanes:chloroform). After approximately 15 minutes, the reaction mixture was poured onto diethylether and washed repeatedly with water. The organic fraction was dried (sodium sulfate) and the solvent was removed. (CAUTION, the product decomposes with heat >60°C or if put onto silica). The crude product was then combined in a round bottom with 5 mg (0.018 mmol) of 9-bromo-10-cyanoanthracene, 3 mg (0.004 mmol) of bis(triphenylphosphine)palladiumdichloride, and a pipette tip of CuI and put under N₂. 5 mL of triethylamine (distilled from CaH₂) was added and the reaction was refluxed overnight. After cooling the solvent was removed and the crude mixture was passed through a plug of silica (deactivated with triethylamine). The crude mixture (4 mg) was then purified in small portions via preparatory scale reverse phase (C18) thin layer

chromatography (1:1 hexanes:dichloromethane) to obtain the product in 7% yield.

Additional purification was accomplished with preparatory HPLC (silica column) with a 3:97 acetonitrile:chloroform eluent.

^1H NMR (CD_2Cl_2) δ : 8.90 (d, $J=8.6$ Hz, 2H), 8.50 (d, $J=8.6$ Hz, 2H), 7.91 (d, 2H), 7.86 (d, 2H), 7.81 (m, 2H), 7.76 (m, 2H), 7.54 (d, $J=8.8$ Hz, 2H), 7.33-7.26 (m, 4H), 6.58 (d, $J=9.0$ Hz, 2H), 3.33 (m, 4H), 2.40 (m, 2H), 2.19 (m, 2H), 2.03 (m, 4H) ES-HRMS (performed with a Q-TOF Ultima mass spectrometer at the University of Illinois at Urbana-Champaign) (m/z) $[\text{M}+\text{H}]^+$ calcd for $\text{C}_{45}\text{H}_{33}\text{N}_2$, 601.2644; found, 601.2641.

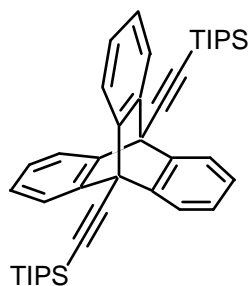


9,10-Bis-[(triisopropylsilyl)-ethynyl]-anthracene 1 g (2.98 mmol) of 9,10

dibromoanthracene, 1.17 g (6.4 mmol) of TIPSacetylene, 83 mg bis(triphenylphosphine)palladiumdichloride, and 46 mg CuI were combined and put under a N_2 atmosphere. 42 mL of diethylamine (distilled from KOH) was added and the solution was put at reflux overnight. After cooling, the solids were filtered off and the product was purified by column chromatography in hexanes. The product was further purified by recrystallization from benzene. A total of 848 mg (52%) was isolated.

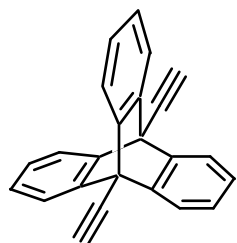
^1H NMR (CDCl_3) δ : 8.64 (m, 4H), 7.61 (m, 4H), 1.28 (m [overlap of doublet and septet], 42H)

^{13}C NMR (CDCl_3) δ : 132.41, 127.25, 126.84, 118.77, 104.79, 103.29, 18.91, 11.58



9,10-Bis[(triisopropylsilyl)ethynyl]tritycene¹⁹³ 500 mg (0.925 mmol) of

9,10-Bis-[(triisopropylsilyl)-ethynyl]-anthracene was put in a round bottom flask under N₂ along with several grams of 3Å molecules sieves. 35 mL of dioxane (distilled from sodium metal and degassed) was added, followed by 0.8 mL (0.7 g, 6 mmol) of isoamyl nitrite. The mixture was then heated to reflux. 809 mg (0.925 mmol) of anthranilic acid (recrystallized from water, dried thoroughly) in 20 mL of dry dioxane was then added, slowly, dropwise. The reaction was allowed to reflux for several hours after addition was complete. After removal of solvent, the crude reaction mixture was purified via column chromatography in hexanes to afford the product (28%). ¹H NMR (CDCl₃) δ: 7.69 (m, 6H), 7.01 (m, 6H), 1.20 (m [overlap of doublet and septet], 42H) EI-HRMS (m/z) [M]⁺ calcd for C₄₂H₅₄Si₂, 614.3759; found, 614.3757.

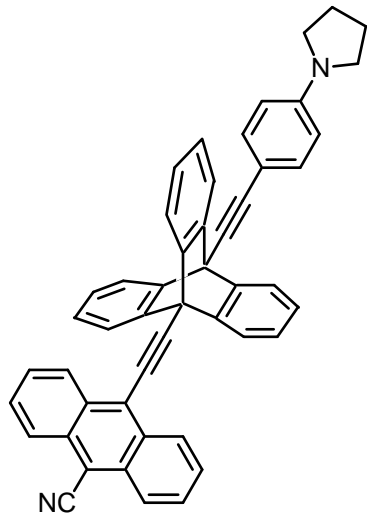


9,10-Diethynyltritycene¹⁹³ 150 mg (0.244 mmol) of 9,10-

Bis[(triisopropylsilyl)ethynyl]tritycene was dissolved in 10 mL of THF and cooled to 0 °C. 0.6 mL of 1M TBAF was slowly added and the reaction was monitored by TLC. After consumption of starting material, the reaction mixture was washed with water and dried with sodium sulfate.

Column chromatography (hexanes) afforded the product in 73% yield. $^1\text{H NMR}$ (CDCl_3) δ :

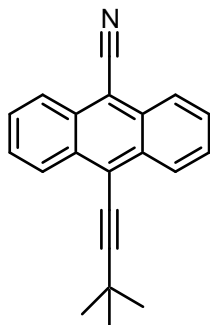
7.77 (m, 6H), 7.11 (m, 6H), 3.30 (s, 2H)



10-[9-(4-Pyrrolidin-1-yl-phenylethynyl)-tritypcenyl-10-

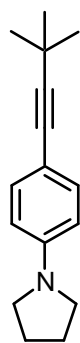
ylethynyl]-anthracene-9-carbonitrile (4) 10 mg (0.033 mmol) of 9,10-diethynyltritypcene, 5 mg (0.032 mmol) of 9-dibromo-10-cyanoanthracene, 4 mg (0.006 mmol) of bis(triphenylphosphine)palladiumdichloride and a pipette tip of CuI were combined and put under N_2 . 4 mL of triethylamine (distilled from KOH) was added and the reaction was refluxed overnight. After cooling, the solvent was removed and the crude mixture was partially purified via column chromatography (chloroform). The enriched material was combined with 15 mg (0.054 mmol) of 1-(4-Iodo-phenyl)-pyrrolidine, 6 mg (0.005 mmol) of tetrakis(triphenylphosphine)palladium, and 1 mg of CuI and put under N_2 . Piperidine (distilled from CaH_2 and sparged with N_2) was added the reaction was stirred at room temperature for 30 minutes with close monitoring via TLC. The reaction was poured onto chloroform and washed repeatedly with water. After drying over sodium sulfate, the solvent was removed and the crude product purified in small portions via preparatory reverse phase (C18) thin layer chromatography (1:1 hexanes:dichloromethane) for a total yield of 15%. $^1\text{H NMR}$ (CD_2Cl_2) δ : 9.06 (d, 2H), 8.55

(d, 2H), 8.01 (m, 3H), 7.93 (m, 3H), 7.87-7.78 (m, 4H), 7.69 (d, 2H), 7.20 (m, 6H), 6.64 (d, 2H), 3.36 (m, 4H), 2.05 (m, 4H) ESI-HRMS (m/z) [M]⁺ calcd for C₄₉H₃₂N₂, 648.25655; found, 648.25718.

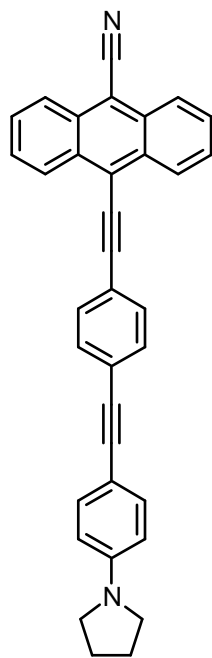


10-(3,3-Dimethylbut-1-ynyl)-anthracene-9-carbonitrile (5) 18 mg (0.06

mmol) of 9-bromo-10-cyanoanthracene, 61 mg (0.74 mmol) of 3,3 dimethyl-1-butyne, 4 mg (0.006 mmol) of Pd(PPh₃)₂Cl₂, and <1 mg of CuI were combined in a flask. 3 mL of TEA (distilled from CaH₂) was added and the mixture was refluxed for 24 hours. The solvent was removed under reduced pressure and the crude material was purified via column chromatography (1:1 hexanes:chloroform). The pure material was isolated in 94% yield. ¹H NMR (CDCl₃) δ: 8.57 (d, J=8.4 Hz, 2H), 8.40 (d, J=8.4 Hz, 2H), 7.71 (t, J=8.5 Hz, 2H), 7.64 (t, J=8.5 Hz, 2H), 1.56 (s, 9H) ¹³C NMR (CDCl₃) δ: 132.68, 131.38, 128.86, 127.65, 126.94, 125.62, 125.20, 117.37, 115.08, 104.87, 75.34, 31.06, 29.09 ESI-HRMS (m/z) [M]⁺ calcd for C₂₁H₁₇N, 283.1361; found, 283.13646.



1-[4-(3,3-Dimethyl-but-1-ynyl)-phenyl]-pyrrolidine (6) 15 mg (0.055 mmol) of 1-(4-Iodo-phenyl)-pyrrolidine, 85 mg (1.04 mmol) of 3,3 dimethyl-1-butyne, 8 mg (0.007 mmol) Pd(PPh₃)₄ and < 1 mg of CuI were combined in a flask. 1 mL of piperidine (distilled from CaH₂ and sparged with N₂) was added and the mixture was allowed to stir at room temperature for 30 minutes, at which point no starting material could be seen by TLC. The mixture was poured onto ether and washed several times with water and dried over sodium sulfate. The solvent was removed and the crude solid was purified via column chromatography (1:1 hexanes:chloroform) to yield the pure product (40%). ¹H NMR (CDCl₃) δ: 7.24 (d, J=8.7 Hz, 2H), 6.44 (d, J=8.7 Hz, 2H), 3.27 (m, 4H), 1.99 (m, 4H), 1.30 (s, 9H)



10-[4-(4-Pyrrolidin-1-yl-phenylethynyl)-phenylethynyl]-anthracene-9-

carbonitrile (7) 15 mg (0.053 mmol) of 9-bromo-10-cyanoanthracene, 100 mg (0.79 mmol) 1,4-diethynylbenzene, 4 mg (0.006 mmol) of $\text{Pd}(\text{PPh}_3)_2\text{Cl}_2$, and <1 mg of CuI were combined in a flask. 5 mL of TEA (distilled from CaH_2) was added and the mixture was refluxed for 24 hours. The solvent was removed under reduced pressure and the crude material was partially purified via column chromatography (7:3 hexanes:chloroform). To the still crude material was added 25 mg of 1-(4-Iodo-phenyl)-pyrrolidine (0.09 mmol), 4 mg (0.003 mmol) of $\text{Pd}(\text{PPh}_3)_4$ and < 1 mg of CuI. The mixture was put under N_2 . 2 mL of piperidine (distilled from CaH_2 and sparged with N_2) was added and the mixture was allowed to stir for 30 minutes. The reaction mixture was poured onto diethylether and washed several times with water and dried over sodium sulfate. After the solvent was removed under reduced pressure, the crude product was redissolved in chloroform and adsorbed onto silica. Slow elution with a 4:6 chloroform:hexanes mixture afforded the pure product (9% over two steps). ^1H NMR (CDCl_3) δ : 8.73 (d, $J=8.1$ Hz, 2H), 8.47

(d, J=8.1 Hz, 2H), 7.79-7.69 (m, 6H), 7.59 (d, J=8.0 Hz, 2H), 7.43 (d, J=8.4 Hz, 2H), 6.53 (d, J=8.4 Hz, 2H), 3.34 (m, 4H), 2.04 (m, 4H)

6.6 Sample Calculations

6.6.1 Reorganization and Activation Energies.

ΔG_{CS}

The energy of the ion pair, ΔG_{IP} was calculated using Weller's¹³ expression

$$\Delta G_{IP} = E_{ox} - E_{red} - \frac{e^2}{r_{DA}\epsilon_s} + e^2 \left(\frac{1}{2r_D} + \frac{1}{2r_A} \right) \left(\frac{1}{\epsilon_s} - \frac{1}{\epsilon_{sp}} \right)$$

	E_{ox}	E_{red}	r_{DA}	ϵ_s	ϵ_{sp}	r_D	r_A
MTHF	.74	-1.27	16.4Å	6.97	37.5	5Å	5Å
Toluene	.74	-1.27	16.4Å	2.38	37.5	5Å	5Å

$\Delta G_{CS} = E^* - \Delta G_{IP}$, where E^* is the excited state energy of CA, which was estimated from the onset of absorption to be 2.79 eV (445 nm)

λ_I

Ion geometries and single points were calculated using unrestricted B3LYP with the 6-31G* basis set.

		In Hartrees	in eV
Caanion in neutr geom:		-865.226	-23361.1
Canion in anion geom:		-865.229	-23361.2
	delta	0.003471	0.093728
PPcation in neutr geom:		-676.824	-18274.3
PPcation in cation geom:		-676.829	-18274.4
	delta	0.00417	0.112596
	total lambda inner		0.206325

λ_O

The solvent component of the reorganization energy was calculated using Marcus's expression employing a dielectric continuum.¹¹⁷

$$\lambda_O = e^2 \left(\frac{1}{2r_D} + \frac{1}{2r_A} - \frac{1}{r_{DA}} \right) \left(\frac{1}{\epsilon_o} - \frac{1}{\epsilon_s} \right)$$

All parameters are in the table above except ϵ_0 , which is 2.24 for toluene and 1.98 for MTHF.

ΔG_{CS}^\ddagger

The activation energy was calculated using the classical Marcus expression¹¹⁷

$$\Delta G^{\ddagger} = \frac{(\Delta G + \lambda)^2}{4\lambda}$$

6.6.2 Overlaps

GTO refers to a radial function with $R(r) = e^{-0.4814r^2}$

EXP refers to a radial function with $R(r) = e^{-1.5r}$

Angular function for p component: $\frac{1}{2} \frac{\sqrt{3} \cos(\theta)}{\sqrt{\pi}}$

Angular function for s component: $\frac{1}{2\sqrt{\pi}}$

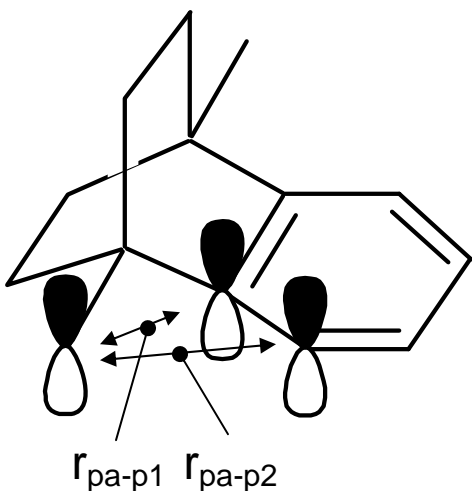
All angular and radial functions were converted to Cartesian (x,y,z) coordinates before integrals were performed. The radial independent variable, r , is in Å. All integrals were performed using Maple 8.0.

$$S_{12} = \frac{\iiint_{x,y,z} \psi_1 \psi_2 dx dy dz}{\sqrt{\iiint_{x,y,z} \psi_1 \psi_1 dx dy dz} \sqrt{\iiint_{x,y,z} \psi_2 \psi_2 dx dy dz}} = \frac{S_{12}}{N}$$

N (GTO) = 0.4690

N (EXP) = 0.0741

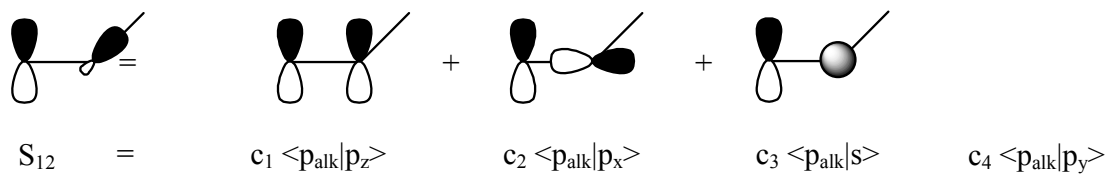
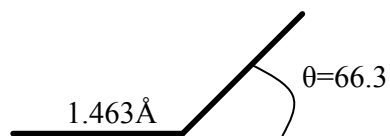
Between alkyne p orbital and bridge π system



$$r_{pa-p1} = 2.503 \text{ \AA} \quad s_{12}(\text{GTO}) = 0.0510 \quad s_{12}(\text{EXP}) = 0.008245$$

$$r_{pa-p2} = 2.954 \text{ \AA} \quad s_{12}(\text{GTO}) = 0.0237 \quad s_{12}(\text{EXP}) = 0.004788$$

Between alkyne p orbital and bridge σ system



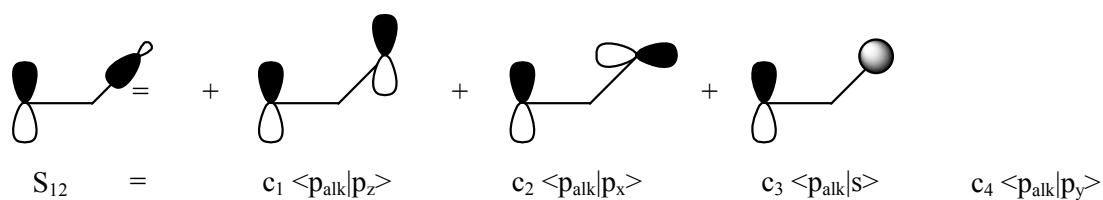
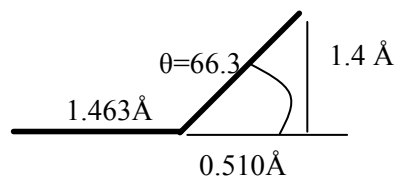
$$c_1 = 0.816 \quad \langle p_{alk} | p_z \rangle (\text{GTO}) = 0.2019 \quad \langle p_{alk} | p_z \rangle (\text{EXP}) = 0.02636$$

$$c_2 = 0.289 \quad \langle p_{alk} | p_x \rangle (\text{GTO}) = 0 \quad \langle p_{alk} | p_x \rangle (\text{EXP}) = 0$$

$$c_3 = 0.5 \quad \langle p_{alk} | s \rangle (\text{GTO}) = 0 \quad \langle p_{alk} | s \rangle (\text{EXP}) = 0$$

$$c_4 = 0$$

$$s_{12}(\text{GTO}) = 0.16475 \quad s_{12}(\text{EXP}) = 0.02151$$



$c_1 = 0.289$	$\langle p_{\text{alk}} p_z \rangle (\text{GTO}) = 0.01228$	$\langle p_{\text{alk}} p_z \rangle (\text{EXP}) = 0.00061$
$c_2 = 0.816$	$\langle p_{\text{alk}} p_x \rangle (\text{GTO}) = 0.09353$	$\langle p_{\text{alk}} p_x \rangle (\text{EXP}) = 0.01129$
$c_3 = 0.5$	$\langle p_{\text{alk}} s \rangle (\text{GTO}) = 0.07150$	$\langle p_{\text{alk}} s \rangle (\text{EXP}) = 0.00995$
$c_4 = 0$		

$$s_{12}(\text{GTO}) = 0.0728 \quad s_{12}(\text{EXP}) = 0.00873$$

Acknowledgments: Joshua Vura-Weis (computational studies and femtosecond transient absorption), Amy Vega (nanosecond transient absorption), Sachin Borkar and Ayusman Sen (high pressure autoclave reactions), Masanori Imura and Barry Carpenter (helpful conversations)

Chapter 7 Conclusion

We take a few paragraphs to describe candidly what we believe to be the most important contributions of this thesis.

The use of fluorene oligomers in Chapters 2 and 3 as a model system for studying distance dependence has offered an incredibly *simple* model for analysis. It is structurally well defined and has components of well defined oxidation potential, unlike many DNA systems. Its static oxidation potentials eliminate the complication of previous studies on conjugated materials. It allows study in the most interesting regime, the range of small activation barriers and fast long distance charge transfer. That it can be so well described by simple rate analysis suggests that our efforts in designing and synthesizing such a material were well worth it.

The conclusions of Chapters 4 and 5 regarding the *illegitimacy* of summing up contributions of multiple pathways in conditions where electronic dephasing is fast is perhaps the most important and least surprising conclusion in this thesis. That phase relationships become destroyed when coupling to an environment is one of the essential transitions that bridge the quantum mechanical world and the classical one. However, a number of reports in the recent literature have suggested that coherent summation of multiple pathways is important in large flexible biomolecules. While these claims may be true depending on the rate of electronic dephasing, the issue of dephasing needs to be addressed explicitly for these systems. Hopefully the work presented in these chapters will stimulate that particular discussion.

Finally, while the data presented on the bicyclo[2.2.2]octane systems suggest, ultimately, that the system did not behave as was designed, it has allowed a fascinating window into the internal mechanism of electronic communication of the bicyclo[2.2.2]octane molecule. That the NBO analysis still cannot capture the experimental behavior suggests the existence of some

fundamental incorrect assumption and we are still trying to figure out what that assumption is. However, finding that assumption may reveal something new about how electronic communication is mediated in these simple systems, which was of course the hope all along.

Chapter 8 Experimental and Computational Methods

8.1 Purification and Characterization

Proton nuclear magnetic resonance spectra were recorded on a Mercury 400 or INOVA 500 NMR spectrometer using TMS as an internal standard. Commercially available reagents were purchased from Sigma-Aldrich Co. or Farchan Laboratories and used without further purification unless otherwise noted. All solvents used for spectroscopy were spectrophotometric grade. Column chromatography was performed using Sorbent Technologies (Atlanta, GA) silica gel. C18 Reverse Phase prepTLC plates were also obtained from Sorbent. Analytical HPLC was performed with a Hewlett-Packard 1100 instrument. Preparatory HPLC was performed using a Dynamaxx Macro HPLC column on a Waters Prep LC 2000 system. Laser desorption mass spectra were obtained with a PE Voyager DE-Pro MALDI-TOF Mass Spectrometer. All high resolution mass spectrometry was done at Northwestern University unless otherwise noted, with an Agilent 6210 (ESI) or a ThermoFinnigan Magnetic Sector Mat 900 XL (EI) instrument.

8.2 Steady State Absorption Spectroscopy

Steady-state absorption and fluorescence measurements were performed, on a Shimadzu (UV-1601) spectrophotometer. Critical wavelength regions were always maintained at an absorbance of less than 1.0. Variable temperature studies were conducted using a Janis VNF-100 cryostat with a Cryo-con 32B temperature controller and a home built quartz sample holder with a 1.6 mm (1/16th inch) pathlength. Absorbance was maintained between 0.5 and 0.7 at 416 nm.

8.3 Cyclic Voltammetry

Electrochemical measurements were performed using a CH Instruments Model 660A electrochemical workstation. For measurements in butyronitrile, acetonitrile, and methylene chloride the electrolyte was 0.1 M tetra-*n*-butylammonium perchlorate. A 1.0 mm diameter platinum disk electrode, platinum wire counter electrode, and Ag/Ag_xO reference electrode were employed. The ferrocene/ferrocenium couple was used as an internal reference for all measurements. Microelectrode techniques with a 10 μm Pt working microelectrode were used to obtain oxidation potentials for the fluorene oligomers in toluene at 40°C containing 0.1 M tetra-*n*-hexylammonium perchlorate⁷³.

8.4 Femtosecond Transient Absorption Spectroscopy

A Spectra-Physics Millennum V frequency-doubled CW Nd:YVO₄ laser was used to pump a Coherent MIRA Ti:sapphire oscillator. The 110 fs, 828-nm pulses from the oscillator were stretched to ~200 ps using a four-pass, reflective, single-grating pulse stretcher and were used to seed a homemade regenerative amplifier, which includes a Medox two-step Pockels cell and driver. The amplifier was pumped at a 2 kHz repetition rate by a Quantronix 527DP frequency-doubled Nd:YLF laser (4.1 mJ/pulse). The amplified Ti:sapphire pulse (0.5 mJ/pulse) was recompressed to approximately 120 fs by a four-pass, reflective, single grating compressor. The pulse energy after compression was 320 μJ/pulse. Two 5% reflective beam splitters were placed in the output path to generate two 828-nm beams for white light generation. The remaining 828-nm light was frequency doubled by using a 1-mm-type I LBO crystal to give 414-nm 120-fs, 75-μJ pulses.⁵⁹ The 828-nm light from the first 5% beam splitter was passed through a waveplate-polarizer pair to control its intensity, and a few microjoules were focused into a 1-

mm sapphire disk to generate white light continuum pulses. All reflective optics were used both to focus the 828-nm pulse into the sapphire and recollimate the white light output, thus limiting the chirp on the white light pulse to <200 fs from 450 to 750 nm. The 828-nm light from the second 5% beam splitter was used to create a second white light continuum by focusing the 828-nm pulse into a 2-mm sapphire disk, using a 100 mm focal length (f.l.) lens. This white light was used to seed the first stage of a two-stage optical parametric amplifier, which has been described previously.²²⁴ The first stage contains a Type II BBO crystal, which was pumped with about 20 μJ of 414-nm light focused into the crystal with a 300 mm f.l. lens. After removal the IR idler beam and residual 414-nm pump light, the first stage produced transform-limited pulses having ~ 1.0 $\mu\text{J}/\text{pulse}$ from 460 to 750 nm. This light was then focused into the Type I BBO of the second stage of the OPA with a 75 mm f.l. lens. The second stage amplifies the first stage light upon overlap with the remaining 55 $\mu\text{J}/\text{pulse}$ of 414 nm pump light. The polarization of the pump and probe beams were offset by 54.7° (magic angle) before reaching the sample. Time resolution was provided by spatially shifting the path length of the pump beam. The instrument was outfitted with a CCD array detector (Ocean Optics PC2000) for simultaneous collection of spectral and kinetic data.²²⁵ Final powers measured immediately before the sample were 1.0-1.2 $\mu\text{J}/\text{pulse}$. Room temperature samples were maintained at an absorbance of 0.5-0.7 at the excitation wavelength in a 2 mm cuvette. Kinetic analyses were performed at several wavelengths using a Levenberg-Marquardt nonlinear least squares fit to a general sum-of-exponentials function with an added Gaussian (0.3 ps i.r.f.) to account for the finite instrument response. Low temperature studies were performed with a Janis cryostat as described above.

8.5 Nanosecond Transient Absorption Spectroscopy and Magnetic Field

Effects

All samples were subjected to four or five freeze-pump-thaw degassing cycles and kept in an airtight cuvette for the duration of the experiment. The samples were excited with 5 ns, 0.5 - 2 mJ laser pulses focused to a 5 mm diameter spot. The pulses were produced using the frequency-tripled output of a Continuum 8000 Nd-YAG laser to pump a Continuum Panther OPO. The probe light was generated using a xenon flashlamp (EG&G Electro-Optics FX-200) and detected using a photomultiplier tube (Hamamatsu R928) after dispersion by a monochromator with high voltage applied to only 4 dynodes. The total instrument response time is 7 ns and is determined primarily by the laser pulse duration. Between 50 and 100 shots were averaged per kinetic trace with a LeCroy 9384 digital oscilloscope and sent to a microcomputer, which calculated the ΔA . Kinetic analyses were performed using a nonlinear least squares fit to a general sum-of-exponentials using the Levenberg-Marquardt algorithm accounting for the presence of the finite instrument response. Samples were maintained at an absorbance of 0.5-0.7 at the excitation wavelength in a 10 mm cuvette

For experiments measuring magnetic field effects, the sample holder or was placed between the poles of a Walker Scientific HV-4W electromagnet powered by a Walker Magnion HS-735 power supply. The field strength was measured by a Lakeshore 450 gaussmeter with a Hall effect probe. Both the electromagnet and the gaussmeter were interfaced with the data collection computer, allowing measurement and control of the magnetic field to 1×10^{-5} T during data acquisition. Due to the length of the sample runs (> 3 hr) a small amount of sample degradation was observed, resulting in a variation in the triplet yield/radical pair

population/recombination rate at zero field, $A(B=0)$, over the course of the experiments. To compensate for this, the magnetic field was reset to $B = 0$ mT every three kinetic traces and $A(B=0)$ was plotted and fit with a polynomial or series of polynomials. These functions were used to calculate the relative yield/population/rate as a function of applied field strength:

$$\frac{T}{T_0} = \frac{\Delta A(B)}{\Delta A(B = 0)}$$

The results presented are an average of three or more experiments conducted on separate days with freshly prepared samples in spectrophotometric or freshly distilled ACS grade solvent.

8.6 Time Resolved Fluorescence

Time-resolved fluorescence data were collected using a home-built cavity-dumped Ti:sapphire oscillator²²⁶ coupled to a streak camera detection system (Hamamatsu C4334 Streakscope). The produced 24- μ J laser pulses at 791 nm with an 825-kHz repetition rate and \sim 30-fs pulse-duration. The laser pulses were frequency doubled in a nonlinear crystal (0.3 mm BBO) to produce 395 nm excitation pulses that were attenuated with a half-wave plate and polarizer to 60-600 pJ/pulse before the sample. Synchronization between the laser pulse train and the streak camera was provided by the acousto-optic cavity dumper (NEOS N13389, N64389-SYN) and a photodiode-discriminator combination that detected the intracavity repetition rate of the laser (82 MHz). The illumination and collection optics were in a standard 90° geometry with the polarization of the excitation pulses and the detected fluorescence controlled by broadband polarizers.²²⁷ The samples were prepared in glass cuvettes, and the optical density at the 400 nm excitation wavelength was typically 0.020-0.035. The instrument response function was 25 ps for our chosen window.

8.7 Computation

All numeric and symbolic manipulations were undertaken using Maple 8.0

In Chapter 2, all geometry optimizations and molecular orbital calculations were done using the semi-empirical AM1 model. The semi-empirical AM1 method was implemented in HyperChem (Hypercube, Inc., 1115 NW 4th Street, Gainesville, Florida 32601, USA).

In Chapter 6, all geometry optimizations and single point calculations were performed using the B3LYP functional with the 6-31G* basis set with Gaussian 98 (Frisch, M. J.; Trucks, G. W.; Schlegel, H. B.; Scuseria, G. E.; Robb, M. A.; Cheeseman, J. R.; Zakrzewski, V. G.; J. A. Montgomery, J.; Stratmann, R. E.; Burant, J. C.; Dapprich, S.; Millam, J. M.; Daniels, A. D.; Kudin, K. N.; Strain, M. C.; Farkas, O.; Tomasi, J.; Barone, V.; Cossi, M.; Cammi, R.; Mennucci, B.; Pomelli, C.; Adamo, C.; Clifford, S.; Ochterski, J.; Petersson, G. A.; Ayala, P. Y.; Cui, Q.; Morokuma, K.; Malick, D. K.; Rabuck, A. D.; Raghavachari, K.; Foresman, J. B.; Cioslowski, J.; Ortiz, J. V.; Baboul, A. G.; Stefanov, B. B.; Liu, G.; Liashenko, A.; Piskorz, P.; Komaromi, I.; Gomperts, R.; Martin, R. L.; Fox, D. J.; Keith, T.; Al-Laham, M. A.; Peng, C. Y.; Nanayakkara, A.; Gonzalez, C.; Challacombe, M.; Gill, P. M. W.; Johnson, B.; Chen, W.; Wong, M. W.; Andres, J. L.; Gonzalez, C.; Head-Gordon, M.; Replogle, E. S.; Pople, J. A. Gaussian 98, Revision A.7; Gaussian, Inc.: Pittsburgh, 1998). NBO analysis was performed using the NBO 3.1 add-on with the B3LYP functional and 6-31G basis set. Molecular dynamics were performed with MOPAC 2007, employing electronic structure calculations at the AM1/CI level with a 3 electron 2 orbital (HOMO, HOMO-1) active space.

References

1. Sun, S.-S.; Sariciftci, N. S., *Organic Photovoltaics: Mechanisms, Materials, and Devices*. CRC Press: Boca Raton, 2005.
2. In *Basic Research Needs for Solar Energy Utilization*, Report of the Basic Energy Sciences Workshop on Solar Energy Utilization, 2005; 2005.
3. Cuniberti, G.; Fagas, G.; Richter, K., *Introducing Molecular Electronics*. Springer Verlag: Berlin, 2005; Vol. 680.
4. Wasielewski, M. R., *Chem. Rev.* **1992**, 92, (3), 435.
5. Hoff, A. J.; Deisenhofer, J., *Phys. Rep.* **1997**, 287, (1-2), 2.
6. Kuki, A.; Wolynes, P. G., *Science* **1987**, 236, (4809), 1647.
7. Marcus, R. A., *Annu. Rev. Phys. Chem.* **1964**, 15, 155.
8. Closs, G. L.; Miller, J. R., *Science* **1988**, 240, (4851), 440.
9. Wasielewski, M. R.; Niemczyk, M. P.; Svec, W. A.; Pewitt, E. B., *J. Am. Chem. Soc.* **1985**, 107, (19), 5562.
10. Finckh, P.; Heitele, H.; Michel-Beyerle, M. E., *Chem. Phys.* **1989**, 138, (1), 1.
11. Bixon, M.; Jortner, J., *J. Phys. Chem.* **1986**, 90, (16), 3795.
12. Kilsa, K.; Kajanus, J.; Macpherson, A. N.; Martensson, J.; Albinsson, B., *J. Am. Chem. Soc.* **2001**, 123, (13), 3069.
13. Staerk, H.; Kuhnle, W.; Treichel, R.; Weller, A., *Chem Phys Lett* **1985**, 118, (1), 19.

14. Kestner, N. R.; Logan, J.; Jortner, J., *J. Phys. Chem.* **1974**, 78, (21), 2148.
15. Nitzan, A., *Chemical Dynamics in Condensed Phases: Relaxation, Transfer, and Reactions in Condensed Molecular Systems*. Oxford University Press: New York, 2006.
16. Mulliken, R. S., *J. Phys. Chem.* **1952**, 56, 295.
17. Paddon-Row, M. N.; Jordan, K. D., *Modern Models of Bonding and Delocalization*. VCH, Weinheim: New York, 1988; Vol. 6.
18. Anderson, P. W., *Phys. Rev.* **1950**, 79, (2), 350.
19. Anderson, P. W., *Phys. Rev.* **1959**, 115, (1), 2.
20. McConnell, H. M., *J. Chem. Phys.* **1961**, 35, 508.
21. Paddon-Row, M. N., *Advances in Physical Organic Chemistry, Vol 38* **2003**, 38, 1.
22. Felts, A. K.; Pollard, W. T.; Friesner, R. A., *J. Phys. Chem.* **1995**, 99, (9), 2929.
23. Berlin, Y. A.; Grozema, F. C.; Seibbeles, L. D. A.; Ratner, M. A., *J. Phys. Chem.* **2007**, submitted.
24. Bixon, M.; Jortner, J., *J. Chem. Phys.* **1997**, 107, (13), 5154.
25. Nitzan, A.; Jortner, J.; Wilkie, J.; Burin, A. L.; Ratner, M. A., *J. Phys. Chem. B* **2000**, 104, (24), 5661.
26. Davis, W. B.; Wasielewski, M. R.; Ratner, M. A.; Mujica, V.; Nitzan, A., *J. Phys. Chem. A* **1997**, 101, (35), 6158.
27. Baer, R.; Neuhauser, D., *J. Am. Chem. Soc.* **2002**, 124, (16), 4200.

28. Lopez-Castillo, J. M.; Filali-Mouhim, A.; Plante, I. L.; Jay-Gerin, J. P., *J. Phys. Chem.* **1995**, 99, (18), 6864.
29. Ratner, M. A., *J. Phys. Chem.* **1990**, 94, (12), 4877.
30. Walter, D.; Neuhauser, D.; Baer, R., *Chem. Phys.* **2004**, 299, (1), 139.
31. Yaliraki, S. N.; Ratner, M. A., *J. Chem. Phys.* **1998**, 109, (12), 5036.
32. Sautet, P.; Joachim, C., *Chem. Phys. Lett.* **1988**, 153, (6), 511.
33. Liang, C. X.; Newton, M. D., *J. Phys. Chem.* **1992**, 96, (7), 2855.
34. Naleway, C. A.; Curtiss, L. A.; Miller, J. R., *J. Phys. Chem.* **1991**, 95, (22), 8434.
35. Paddon-Row, M. N.; Shephard, M. J., *J. Am. Chem. Soc.* **1997**, 119, (23), 5355.
36. Reed, A. E.; Curtiss, L. A.; Weinhold, F., *Chem. Rev.* **1988**, 88, (6), 899.
37. Balabin, I. A.; Onuchic, J. N., *Science* **2000**, 290, (5489), 114.
38. Kawatsu, T.; Kakitani, T.; Yamato, T., *J. Phys. Chem. B* **2002**, 106, (43), 11356.
39. Prytkova, T. R.; Kurnikov, I. V.; Beratan, D. N., *Science* **2007**, 315, (5812), 622.
40. Hoffman, R., *Acc. Chem. Res.* **1970**, 4, (1), 1.
41. Verhoeven, J. W.; Pasman, P., *Tetrahedron* **1981**, 37, (5), 943.
42. Bischof, P.; Hashmall, J. A.; Heilbronner, E.; Hornung, V., *Tetrahedron Lett.* **1969**, (46), 4025.
43. Heilbronner, E.; Muszkat, K. A., *J. Am. Chem. Soc.* **1970**, 92, (12), 3818.
44. Patoux, C.; Coudret, C.; Launay, J. P.; Joachim, C.; Gourdon, A., *Inorg. Chem.* **1997**, 36, (22), 5037.

45. Zeng, Y.; Zimmt, M. B., *J. Am. Chem. Soc.* **1991**, 113, (13), 5107.
46. Leggett, A. J.; Chakravarty, S.; Dorsey, A. T.; Fisher, M. P. A.; Garg, A.; Zwerger, W., *Rev. Mod. Phys.* **1987**, 59, (1), 1.
47. Nitzan, A., *Annu. Rev. Phys. Chem.* **2001**, 52, 681.
48. Onuchic, J. N.; Wolynes, P. G., *J. Phys. Chem.* **1988**, 92, (23), 6495.
49. Reichman, D.; Silbey, R. J.; Suarez, A., *J. Chem. Phys.* **1996**, 105, (23), 10500.
50. Skinner, J. L.; Hsu, D., *J. Phys. Chem.* **1986**, 90, (21), 4931.
51. Toutounji, M.; Small, G. J.; Mukamel, S., *J. Chem. Phys.* **1999**, 110, (2), 1017.
52. Lee, H.; Cheng, Y. C.; Fleming, G. R., *Science* **2007**, 316, (5830), 1462.
53. Myers, A. B., *Annu. Rev. Phys. Chem.* **1998**, 49, 267.
54. Reinot, T.; Kim, W. H.; Hayes, J. M.; Small, G. J., *J. Chem. Phys.* **1997**, 106, (14), 6205.
55. Davis, W. B.; Svec, W. A.; Ratner, M. A.; Wasielewski, M. R., *Nature* **1998**, 396, 60.
56. Weiss, E. A.; Ahrens, M. J.; Sinks, L. E.; Gusev, A. V.; Ratner, M. A.; Wasielewski, M. R., *J. Am. Chem. Soc.* **2004**, 126, 5577.
57. Skourtis, S. S.; Waldeck, D. H.; Beratan, D. N., *J. Phys. Chem. B* **2004**, 108, (40), 15511.
58. Davis, W. B.; Ratner, M. A.; Wasielewski, M. R., *Chem. Phys.* **2002**, 281, 333.
59. Weiss, E. A.; Sinks, L. E.; Lukas, A. S.; Chernick, E. T.; Ratner, M. A.; Wasielewski, M. R., *J. Phys. Chem. B* **2004**, 108, (29), 10309.
60. Kramers, H. A., *Physica* **1934**, 1, 182.
61. Yamashita, J.; Kondo, J., *Phys. Rev.* **1958**, 109, (3), 730.

62. Kobori, Y.; Sekiguchi, S.; Akiyama, K.; Tero-Kubota, S., *J. Phys. Chem. A* **1999**, 103, (28), 5416.
63. Paddon-Row, M. N.; Shephard, M. J., *J. Phys. Chem. A* **2002**, 106, (12), 2935.
64. Volk, M.; Haberle, T.; Feick, R.; Ogrodnik, A.; Michel-Beyerle, M. E., *J. Phys. Chem.* **1993**, 97, (38), 9831.
65. Steiner, U. E.; Ulrich, T., *Chem. Rev.* **1989**, 89, 51.
66. Schulten, K.; Staerk, H.; Weller, A.; Werner, H.; Nickel, B., *Z. Phys. Chem. NF* **1976**, 101, 371.
67. Sakaguchi, Y.; Hayashi, H., *J. Phys. Chem. A* **1997**, 101, 549.
68. Werner, U.; Kuhnle, W.; Staerk, H., *J. Phys. Chem.* **1993**, 97, 9280.
69. Tadjikov, B.; Smirnov, S., *Phys. Chem. Chem. Phys.* **2001**, 3, (2), 204.
70. Tsentalovich, Y. P.; Morozova, O., B.; Avdievich, N. I.; Ananchenko, G. S.; Yurkovskaya, A. V.; Ball, J. D.; Forbes, M., D.E., *J. Phys. Chem. A* **1997**, 101, (47), 8809.
71. Shultz, D. A.; Fico, R. M.; Lee, H.; Kampf, J. W.; Kirschbaum, K.; Pinkerton, A. A.; Boyle, P. D., *J. Am. Chem. Soc.* **2003**, 125, 15426.
72. Kanibolotsky, A., L.; Berridge, R.; Skabara, P. J.; Perepichka, I. F.; Bradley, D. D. C.; Koeberg, M., *J. Am. Chem. Soc.* **2004**, 126, 13695.
73. Geng, L.; Ewing, A. G.; Jernigan, J. C.; Murray, R. W., *Anal. Chem.* **1986**, 58, (4), 852.
74. Rault-Berthelot, J.; Simonet, J., *J. Electroanal. Chem.* **1985**, 182, 187.
75. Rault-Berthelot, J.; Cariou, M.; Tahri-Hassani, J., *J. Electroanal. Chem.* **1996**, 402, 203.

76. Daub, J.; Engl, R.; Kurzawa, J.; Miller, S. E.; Schneider, S.; Stockmann, A.; Wasielewski, M. R., *J. Phys. Chem. A* **2001**, 105, 5655.
77. Rybtchinski, B.; Sinks, L. E.; Wasielewski, M. R., *J. Phys. Chem. A* **2004**, 108, (37), 7497.
78. van der Boom, T.; Hayes, R. T.; Zhao, Y.; Bushard, P. J.; Weiss, E. A.; Wasielewski, M. R., *J. Am. Chem. Soc.* **2002**, 124, 9582.
79. Anemian, R.; Mulatier, J.-C.; Andraud, C.; Stephan, O.; Vial, J.-C., *J. Chem. Soc., Chem. Commun.* **2002**, 1608.
80. Klaerner, G.; Miller, R. D., *Macromolecules* **1998**, 31, 2007.
81. Tabushi, I.; Yoshida, Z.; Aoyama, Y., *Bull. Chem. Soc. Jpn.* **1974**, 47, (12), 3079.
82. Sartor, V.; Boone, E.; Schuster, G. B., *J. Phys. Chem. B* **2001**, 105, (45), 11057.
83. Pourtois, G.; Beljonne, D.; Cornil, J.; Ratner, M. A.; Bredas, J. L., *J. Amer. Chem. Soc.* **2002**, 124, (16), 4436.
84. Hasharoni, K.; Levanon, H.; Greenfield, S. R.; Gosztola, D. J.; Svec, W. A.; Wasielewski, M. R., *J. Am. Chem. Soc.* **1995**, 117, (30), 8055.
85. Helms, A.; Heller, D.; McLendon, G., *J. Amer. Chem. Soc.* **1992**, 114, 6227.
86. Paddon-Row, M. N., *Acc. Chem. Res.* **1994**, 27, 18.
87. Perng, B. C.; Newton, M. D.; Raineri, F. O.; Friedman, H. L., *J. Chem. Phys.* **1996**, 104, (18), 7153.

88. Perng, B. C.; Newton, M. D.; Raineri, F. O.; Friedman, H. L., *J. Chem. Phys.* **1996**, 104, (18), 7177.
89. Nishinaga, T.; Inoue, R.; Matsuura, A.; Komatsu, K., *Org. Lett.* **2002**, 4, (23), 4117.
90. Carreira, L. A.; Towns, T. G., *J. Mol. Struct.* **1977**, 41, (1), 1.
91. Nitzan, A.; Ratner, M. A., *Science* **2003**, 300, (5624), 1384.
92. Karzazi, Y.; Crispin, X.; Kwon, O.; Bredas, J. L.; Cornil, J., *Chem. Phys. Lett.* **2004**, 387, (4-6), 502.
93. Nelsen, S. F.; Ismagilov, R. F.; Teki, Y., *J. Am. Chem. Soc.* **1998**, 120, (9), 2200.
94. Kobori, Y.; Yago, T.; Akiyama, K.; Tero-Kubota, S.; Sato, H.; Hirata, F.; Norris, J. R., *J. Phys. Chem. B* **2004**, 108, (29), 10226.
95. Jortner, J.; Bixon, M., *Electron Transfer - From Isolated Molecules to Biomolecules*. Wiley: New York, 1999; Vol. 106.
96. Fukuzumi, S., *Functional Organic Materials* **2007**, 465.
97. Shirota, Y.; Kageyama, H., *Chem. Rev.* **2007**, 107, (4), 953.
98. Wasielewski, M. R., *J. Org. Chem.* **2006**, 71, (14), 5051.
99. Vongersdorff, J.; Kirste, B.; Niethammer, D.; Harrer, W.; Kurreck, H., *Magn. Reson. Chem.* **1988**, 26, (5), 416.
100. Leland, B. A.; Joran, A. D.; Felker, P. M.; Hopfield, J. J.; Zewail, A. H.; Dervan, P. B., *J. Phys. Chem.* **1985**, 89, (26), 5571.

101. Goldsmith, R. H.; Sinks, L. E.; Kelley, R. F.; Betzen, L. J.; Liu, W. H.; Weiss, E. A.; Ratner, M. A.; Wasielewski, M. R., *Proc. Natl. Acad. Sci. U. S. A.* **2005**, 102, (10), 3540.
102. Helms, A.; Heiler, D.; Mclendon, G., *J. Am. Chem. Soc.* **1992**, 114, (15), 6227.
103. Dance, Z. E. X.; Mi, Q. X.; McCamant, D. W.; Ahrens, M. J.; Ratner, M. A.; Wasielewski, M. R., *J. Phys. Chem. B* **2006**, 110, (50), 25163.
104. *Long-Range Charge Transfer in DNA, I and II.* Springer: Heidelberg, 2004; Vol. 236,237.
105. Bixon, M.; Jortner, J., *Chem. Phys.* **2002**, 281, (2-3), 393.
106. Segal, D.; Nitzan, A.; Davis, W. B.; Wasielewski, M. R.; Ratner, M. A., *J. Phys. Chem. B* **2000**, 104, (16), 3817.
107. Giese, B.; Amaudrut, J.; Kohler, A. K.; Spormann, M.; Wessely, S., *Nature* **2001**, 412, (6844), 318.
108. Davis, W. B.; Ratner, M. A.; Wasielewski, M. R., *J. Am. Chem. Soc.* **2001**, 123, (32), 7877.
109. Hapiot, P.; Lagrost, C.; Le Floch, F.; Raoult, E.; Rault-Berthelot, J., *Chem. Mater.* **2005**, 17, (8), 2003.
110. Hughes, G.; Bryce, M. R., *J. Mater. Chem.* **2005**, 15, (1), 94.
111. Montes, V. A.; Perez-Bolivar, C.; Agarwal, N.; Shinar, J.; Anzenbacher, P., *J. Am. Chem. Soc.* **2006**, 128, (38), 12436.
112. Takeda, N.; Asaoka, S.; Miller, J. R., *J. Am. Chem. Soc.* **2006**, 128, (50), 16073.

113. Fratiloiu, S.; Fonseca, S. M.; Grozema, F. C.; Burrows, H. D.; Costa, M. L.; Charas, A.; Morgado, J.; Siebbeles, L. D. A., *J. Phys. Chem. C* **2007**, 111, (15), 5812.
114. Prins, P.; Grozema, F. C.; Galbrecht, F.; Scherf, U.; Siebbeles, L. D. A., *J. Phys. Chem. C* **2007**, 111, (29), 11104.
115. Stevens, M. A.; Silva, C.; Russell, D. M.; Friend, R. H., *Phys. Rev. B* **2001**, 63, (16), 165213.
116. Westerling, M.; Aarnio, H.; Osterbacka, R.; Stubb, H.; King, S. M.; Monkman, A. P.; Andersson, M. R.; Jespersen, K.; Kesti, T.; Yartsev, A.; Sundstrom, V., *Phys. Rev. B* **2007**, 75, (22).
117. Marcus, R. A.; Sutin, N., *Biochim. Biophys. Acta* **1985**, 811, (3), 265.
118. Kasha, M.; Rawls, H. R.; El-Bayyoubi, M. A., *Pure Appl. Chem.* **1965**, 11, 371.
119. Rybtchinski, B.; Sinks, L. E.; Wasielewski, M. R., *J. Am. Chem. Soc.* **2004**, 126, (39), 12268.
120. Cui, C. Z.; Cho, S. J.; Kim, K. S.; Baehr, C.; Jung, J. C., *J. Chem. Phys.* **1997**, 107, (23), 10201.
121. Pan, D. H.; Phillips, D. L., *J. Phys. Chem. A* **1999**, 103, (24), 4737.
122. Endredi, H.; Billes, F.; Tosa, M.; Majdik, C.; Irimie, F. D., *Spectrochim. Acta A Molec. Biomolec. Spec.* **2006**, 63, (2), 349.
123. Bixon, M.; Jortner, J., *J. Am. Chem. Soc.* **2001**, 123, (50), 12556.
124. Nakatani, K.; Dohno, C.; Saito, I., *J. Am. Chem. Soc.* **2000**, 122, (24), 5893.

125. Nadeau, J. G.; Crothers, D. M., *Proc. Natl. Acad. Sci. U. S. A.* **1989**, 86, (8), 2622.
126. Takada, T.; Kawai, K.; Fujitsuka, M.; Majima, T., *Proc. Natl. Acad. Sci. U. S. A.* **2004**, 101, (39), 14002.
127. Lewis, F. D.; Zhu, H. H.; Daublain, P.; Cohen, B.; Wasielewski, M. R., *Angew. Chem., Int. Ed. Engl.* **2006**, 45, (47), 7982.
128. Xiao, X. Y.; Xu, B. Q.; Tao, N. J., *Nano. Lett.* **2004**, 4, (2), 267.
129. Elangovan, A.; Kao, K. M.; Yang, S. W.; Chen, Y. L.; Ho, T. I.; Su, Y. L. O., *J. Org. Chem.* **2005**, 70, (11), 4460.
130. Braga, M.; Larsson, S., *Chem. Phys. Lett.* **1993**, 213, (3-4), 217.
131. Magoga, M.; Joachim, C., *Phys. Rev. B* **1999**, 59, (24), 16011.
132. Blum, A. S.; Kushmerick, J. G.; Pollack, S. K.; Yang, J. C.; Moore, M.; Naciri, J.; Shashidhar, R.; Ratna, B. R., *J. Phys. Chem. B* **2004**, 108, (47), 18124.
133. Kushmerick, J. G.; Naciri, J.; Yang, J. C.; Shashidhar, R., *Nano. Lett.* **2003**, 3, (7), 897.
134. Caldeira, A. O.; Leggett, A. J., *Phys. Rev. A* **1985**, 31, (2), 1059.
135. Goldsmith, R. H.; Wasielewski, M. R.; Ratner, M. A., *J. Phys. Chem. B* **2006**, 110, (41), 20258.
136. Segal, D.; Nitzan, A., *Chem. Phys.* **2001**, 268, (1-3), 315.
137. Xu, B. Q.; Zhang, P. M.; Li, X. L.; Tao, N. J., *Nano. Lett.* **2004**, 4, (6), 1105.
138. Ratner, M. A.; Ondrechen, M. J., *Mol. Phys.* **1976**, 32, (5), 1233.
139. Bixon, M.; Jortner, J., *Adv. Chem. Phys.* **1999**, 106, 35.

140. Kalyanaraman, C.; Evans, D. G., *Nano. Lett.* **2002**, 2, (5), 437.
141. Redfield, A. G., *IBM J. Res. Dev.* **1957**, 1, (1), 19.
142. Sension, R. J., *Nature* **2007**, 446, (7137), 740.
143. Jackson, B.; Silbey, R., *Chem. Phys. Lett.* **1983**, 99, (4), 331.
144. Vohringer, P.; Arnett, D. C.; Westervelt, R. A.; Feldstein, M. J.; Scherer, N. F., *J. Chem. Phys.* **1995**, 102, (10), 4027.
145. Bell, R. J.; Dean, P., *Discuss. Farad. Soc.* **1970**, 50, 55.
146. Elicker, T. S.; Evans, D. G., *J. Phys. Chem. A.* **1999**, 103, (47), 9423.
147. Evensky, D. A.; Scalettar, R. T.; Wolynes, P. G., *J. Phys. Chem.* **1990**, 94, (3), 1149.
148. Meier, M.; Sun, J.; Wishart, J. F.; vanEldik, R., *Inorg. Chem.* **1996**, 35, (6), 1564.
149. Kirkwood, J. C.; Scheurer, C.; Chernyak, V.; Mukamel, S., *J. Chem. Phys.* **2001**, 114, (5), 2419.
150. Volkovich, R.; Peskin, U., *J. Chem. Phys.* **2006**, 125, (24), 244505.
151. Ollivier, H.; Poulin, D.; Zurek, W. H., *Phys. Rev. A* **2005**, 72, (4), 42113.
152. Curry, W. B.; Grabe, M. D.; Kurnikov, I. V.; Skourtis, S. S.; Beratan, D. N.; Regan, J. J.; Aquino, A. J. A.; Beroza, P.; Onuchic, J. N., *J. Bioenerg. Biomembr.* **1995**, 27, (3), 285.
153. Datta, S., *Electric Transport in Mesoscopic Systems*. Cambridge University Press: Cambridge, UK, 1995.
154. Webb, R. A.; Washburn, S.; Umbach, C. P.; Laibowitz, R. B., *Phys. Rev. Lett.* **1985**, 54, (25), 2696.

155. Cardamone, D. M.; Stafford, C. A.; Mazumdar, S., *Nano. Lett.* **2006**, 6, (11), 2422.
156. Duchemin, I.; Joachim, C., *Chem. Phys. Lett.* **2005**, 406, (1-3), 167.
157. Hod, O.; Rabani, E.; Baer, R., *Acc. Chem. Res.* **2006**, 39, (2), 109.
158. Galperin, M.; Ratner, M. A.; Nitzan, A., *J. Chem. Phys.* **2004**, 121, (23), 11965.
159. Marvaud, V.; Launay, J. P.; Joachim, C., *Chem. Phys.* **1993**, 177, (1), 23.
160. Regan, J. J.; Risser, S. M.; Beratan, D. N.; Onuchic, J. N., *J. Phys. Chem.* **1993**, 97, (50), 13083.
161. Schatz, G. C.; Ratner, M. A., *Quantum Mechanics in Chemistry*. Dover Publications: Mineola, New York, 2002.
162. Bloembergen, N.; Purcell, E. M.; Pound, R. V., *Phys. Rev.* **1948**, 73, (7), 679.
163. Weitz, D. A.; Garoff, S.; Gersten, J. I.; Nitzan, A., *J. Chem. Phys.* **1983**, 78, (9), 5324.
164. Segal, D.; Nitzan, A.; Ratner, M.; Davis, W. B., *J. Phys. Chem. B* **2000**, 104, (13), 2790.
165. Joachim, C.; Ratner, M. A., *Nanotechnology* **2004**, 15, (8), 1065.
166. Slichter, C. P., *Principles of Magnetic Resonance*. Springer-Verlag: New York, 1990.
167. Bovey, F. A., *Nuclear Magnetic Resonance Spectroscopy*. Academic Press, Inc.: New York, 1988.
168. Imry, Y., *Introduction to Mesoscopic Physics*. Oxford University Press, Inc.: Cary, NC, USA, 1997.
169. Buttiker, M.; Landauer, R., *Phys. Rev. Lett.* **1982**, 49, (23), 1739.
170. Kennedy, S. P.; Garro, N.; Phillips, R. T., *Phys. Rev. Lett.* **2001**, 86, (18), 4148.

171. Milota, F.; Sperling, J.; Szocs, V.; Tortschanoff, A.; Kauffmann, H. F., *J. Chem. Phys.* **2004**, 120, (20), 9870.
172. Cherepy, N. J.; Shreve, A. P.; Moore, L. J.; Boxer, S. G.; Mathies, R. A., *J. Phys. Chem. B* **1997**, 101, (16), 3250.
173. Bandopadhyay, S.; Dutta-Roy, B.; Mani, H. S., *Amer. J. Phys.* **2004**, 72, (12), 1501.
174. Fano, U., *Phys. Rev.* **1961**, 1, (6), 1866.
175. Salem, L., *The Molecular Orbital Theory of Conjugated Systems*. W. A. Benjamin, Inc.: New York, 1966.
176. Paddon-Row, M. N., *Acc. Chem. Res.* **1982**, 15, (8), 245.
177. Lockard, J. V.; Zink, J. I.; Trieber, D. A.; Konradsson, A. E.; Weaver, M. N.; Nelsen, S. F., *J. Phys. Chem. A* **2005**, 109, (6), 1205.
178. Sautet, P.; Bocquet, M. L., *Phys. Rev. B* **1996**, 53, (8), 4910.
179. Staab, H. A.; Binnig, F., *Tetrahedron Lett.* **1964**, (7-8), 319.
180. Irgartinger, H.; Leiserow, L.; Schmidt, M. J., *Chem. Ber.* **1970**, 103, (4), 1132.
181. Oevering, H.; Paddon-Row, M. N.; Heppener, M.; Oliver, A. M.; Cotsaris, E.; Verhoeven, J. W.; Hush, N. S., *J. Am. Chem. Soc.* **1987**, 109, (11), 3258.
182. Schwab, P. F. H.; Levin, M. D.; Michl, J., *Chem. Rev.* **1999**, 99, (7), 1863.
183. Zimmerman, H. E.; McKelvey, R. D., *J. Am. Chem. Soc.* **1971**, 93, (15), 3638.
184. Pettersson, K.; Wiberg, J.; Ljungdahl, T.; Martensson, J.; Albinsson, B., *J. Phys. Chem. A* **2006**, 110, (1), 319.

185. Goldsmith, R. H.; Wasielewski, M. R.; Ratner, M. A., *J. Am. Chem. Soc.* **2007**, 129, (43), 3066.
186. Voegtle, F.; Frank, M.; Nieger, M.; Belser, P.; von Zelewsky, A.; Balzani, V.; Barigelletti, F.; De Cola, L.; Flamigni, L., *Angew. Chem., Int. Ed. Engl.* **1993**, 32, (11), 1643.
187. Beyeler, A.; Belser, P., *Coord. Chem. Rev.* **2002**, 230, (1-2), 29.
188. Adcock, W.; Trout, N. A., *Chem. Rev.* **1999**, 99, (5), 1415.
189. Stock, L. M., *J. Chem. Educ.* **1972**, 49, (6), 400.
190. Effenberger, F.; Agster, W.; Fischer, P.; Jogun, K. H.; Stezowski, J. J.; Daltrozzo, E.; Kollmannsberger-von Nell, G., *J. Org. Chem.* **1983**, 48, (24), 4649.
191. de Montigny, F.; Argouarch, G.; Lapinte, C., *Synthesis* **2006**, (2), 293.
192. Kumar, K.; Wang, S. S.; Sukenik, C. N., *J. Org. Chem.* **1984**, 49, (4), 665.
193. Caskey, D. C.; Wang, B.; Zheng, X. L.; Michl, J., *Collect. Czech. Chem. Commun.* **2005**, 70, (11), 1970.
194. Chapman, N. B.; Sotheeswaran, S.; Toyne, K. J., *J. Org. Chem.* **1970**, 35, (4), 917.
195. Chu, Y. J.; Lynch, V.; Iverson, B. L., *Tetrahedron* **2006**, 62, (23), 5536.
196. Schmid, G. H.; Rabai, J., *Synthesis* **1988**, (4), 332.
197. Roth, G. J.; Liepold, B.; Muller, S. G.; Bestmann, H. J., *Synthesis* **2004**, (1), 59.
198. Miller, M. W.; Amidon, R. W.; Tawney, P. O., *J. Am. Chem. Soc.* **1955**, 77, (10), 2845.
199. Badger, G. M.; Cook, J. W., *J. Chem. Soc.* **1939**, 802.
200. Chapman, N. B.; Sotheesw.S; Toyne, K. J., *Chem. Comm.* **1965**, (11), 214.

201. Thomas, C. L. 1946.
202. Godinez, C. E.; Zepeda, G.; Garcia-Garibay, M. A., *J. Am. Chem. Soc.* **2002**, 124, (17), 4701.
203. Binmore, G. T.; Walton, J. C.; Adcock, W.; Clark, C. I.; Krstic, A. R., *Magn. Reson. Chem.* **1995**, 33, S53.
204. Cieplak, A. S., *J. Am. Chem. Soc.* **1981**, 103, (15), 4540.
205. Tomoda, S., *Chem. Rev.* **1999**, 99, (5), 1243.
206. DeKock, R. L.; Gray, H. B., *Chemical Structure and Bonding*. University Science Books: Sausalito, CA, 1989.
207. Ramakrishnan, G.; Jouaiti, A.; Geoffroy, M.; Bernardinelli, G., *J. Phys. Chem.* **1996**, 100, (26), 10861.
208. Krusic, P. J.; Schleyer, P. V.; Rettig, T. A., *J. Am. Chem. Soc.* **1972**, 94, (3), 995.
209. Rozeboom, M. D.; Houk, K. N.; Searles, S.; Seyedrezai, S. E., *J. Am. Chem. Soc.* **1982**, 104, (12), 3448.
210. Barthel, E. R.; Martini, I. B.; Schwartz, B. J., *J. Phys. Chem. B* **2001**, 105, (49), 12230.
211. Kuharski, R. A.; Bader, J. S.; Chandler, D.; Sprik, M.; Klein, M. L.; Impey, R. W., *J. Chem. Phys.* **1988**, 89, (5), 3248.
212. Read, I.; Napper, A.; Zimmt, M. B.; Waldeck, D. H., *J. Phys. Chem. A* **2000**, 104, (41), 9385.
213. Kelly, T. R., *Acc. Chem. Res.* **2001**, 34, (6), 514.

214. Balzani, V.; Barigelletti, F.; Belser, P.; Bernhard, S.; DeCola, L.; Flamigni, L., *J. Phys. Chem.* **1996**, 100, (42), 16786.
215. Jones, G. A.; Paddon-Row, M. N.; Carpenter, B. K.; Piotrowiak, P., *J. Phys. Chem. A.* **2002**, 106, (19), 5011.
216. Morsi, S. E.; Carr, D.; El-Bayoumi, M. A., *Chem. Phys. Lett.* **1978**, 58, (4), 571.
217. Acharya, S.; Bhattacharjee, D.; Talapatra, G. B., *Chem. Phys. Lett.* **2002**, 352, (5-6), 429.
218. Jones, G. A.; Carpenter, B. K.; Paddon-Row, M. N., *J. Am. Chem. Soc.* **1998**, 120, (22), 5499.
219. Wood, G.; Woo, E. P., *Can. J. Chem.* **1968**, 46, (23), 3713.
220. Holtz, H. D.; Stock, L. M., *J. Am. Chem. Soc.* **1964**, 86, (23), 5183.
221. Honegger, E.; Heilbronner, E.; Hess, N.; Martin, H. D., *Chem. Ber.* **1987**, 120, (2), 187.
222. Pietruszka, J.; Witt, A., *Synthesis* **2006**, (24), 4266.
223. Klanderman, B. H.; Faber, J. W. H., *J. Polym. Sci., Part A: Polym. Chem.* **1968**, 6, (11PA), 2955.
224. Greenfield, S. R.; Wasielewski, M. R., *Opt. Lett.* **1995**, 20, 1394.
225. Giaimo, J. M.; Gusev, A. V.; Wasielewski, M. R., *J. Am. Chem. Soc.* **2002**, 124, 8530.
226. Pshenichnikov, M. S.; de Boerij, W. P.; Wiersma, D. A., *Opt. Lett.* **1994**, 19, 572.
227. Lakowicz, J. R., *Principles of Fluorescence Spectroscopy*. Kluwer: Dordrecht, 1999.
228. The semi-empirical AM1 method was implemented in HyperChem (Hypercube, Inc., 1115 NW 4th Street, Gainesville, Florida 32601, USA)

229. Frisch, M. J.; Trucks, G. W.; Schlegel, H. B.; Scuseria, G. E.; Robb, M. A.; Cheeseman, J. R.; Zakrzewski, V. G.; J. A. Montgomery, J.; Stratmann, R. E.; Burant, J. C.; Dapprich, S.; Millam, J. M.; Daniels, A. D.; Kudin, K. N.; Strain, M. C.; Farkas, O.; Tomasi, J.; Barone, V.; Cossi, M.; Cammi, R.; Mennucci, B.; Pomelli, C.; Adamo, C.; Clifford, S.; Ochterski, J.; Petersson, G. A.; Ayala, P. Y.; Cui, Q.; Morokuma, K.; Malick, D. K.; Rabuck, A. D.; Raghavachari, K.; Foresman, J. B.; Cioslowski, J.; Ortiz, J. V.; Baboul, A. G.; Stefanov, B. B.; Liu, G.; Liashenko, A.; Piskorz, P.; Komaromi, I.; Gomperts, R.; Martin, R. L.; Fox, D. J.; Keith, T.; Al-Laham, M. A.; Peng, C. Y.; Nanayakkara, A.; Gonzalez, C.; Challacombe, M.; Gill, P. M. W.; Johnson, B.; Chen, W.; Wong, M. W.; Andres, J. L.; Gonzalez, C.; Head-Gordon, M.; Replogle, E. S.; Pople, J. A. *Gaussian 98, Revision A.7*; Gaussian, Inc.: Pittsburgh, 1998
230. Asselberghs, I.; Clays, K.; Persoons, A.; McDonagh, A. M.; Ward, M. D.; McCleverty, J. A., *Chem. Phys. Lett.* **2003**, 368, (3-4), 408.
231. Coe, B. J.; Harris, J. A.; Jones, L. A.; Brunshwig, B. S.; Song, K.; Clays, K.; Garin, J.; Orduna, J.; Coles, S. J.; Hursthouse, M. B., *J. Am. Chem. Soc.* **2005**, 127, (13), 4845.
232. Monk, P. M. S.; Mortimer, R. J.; Rosseinsky, D. R., *Electrochromism: Fundamentals and Applications*. VCH: Weinheim, 1995.
233. Schwendeman, I.; Hwang, J.; Welsh, D. M.; Tanner, D. B.; Reynolds, J. R., *Advanced Materials* **2001**, 13, (9), 634.
234. Bergstedt, T. S.; Hauser, B. T.; Schanze, K. S., *J. Am. Chem. Soc.* **1994**, 116, (18), 8380.
235. Schanze, K. S.; Bergstedt, T. S.; Hauser, B. T., *Advanced Materials* **1996**, 8, (6), 531.
236. Schanze, K. S.; Bergstedt, T. S.; Hauser, B. T.; Cavalaheiro, C. S. P., *Langmuir* **2000**, 16, (2), 795.
237. Tian, S.; Armstrong, N. R.; Knoll, W., *Langmuir* **2005**.
238. Kwong, V. H.; Mossman, M. A.; Whitehead, L. A., *Appl. Opt.* **2002**, 41, (16), 3343.
239. Saleh, B. E. A.; Teich, M. C., *Fundamentals of Photonics*. Wiley: New York, 1991.

240. Tourillon, G., Polythiophene and Its Derivatives. In *Handbook of Conducting Polymers*, Skotheim, T. E., Ed. Marcel Dekker, Inc: New York, 1986; Vol. 1, pp 293.
241. Mardalen, J.; Samuelsen, E. J.; Gautun, O. R.; Carlsen, P. H. J., *Makromolekulare Chemie-Macromolecular Chemistry and Physics* **1993**, 194, (9), 2483.
242. Plieth, W. J.; Zerbino, J.; Lahmann, C.; Kossmehl, G., *J. Electroanal. Chem.* **1989**, 274, (1-2), 213.
243. Bailey, R. C.; Hupp, J. T., *J. Am. Chem. Soc.* **2002**, 124, (23), 6767.
244. Meerholz, K.; Heinze, J., *Electrochim. Acta* **1996**, 41, (11-12), 1839.
245. Boyd, R. W., *Nonlinear Optics*. Academic Press: New York, 2003.

Appendix A

Fast Redox Switchable Diffraction Gratings

Redox processes have proven to be an extremely convenient tool for modulation of a diverse number of device and materials properties. Redox switchability has been cleverly incorporated to allow control over a number of optical properties, including hyperpolarizability,^{230, 231} and both the real and imaginary components of the refractive index, allowing construction of materials with variable absorption²³² (electrochromic materials), variable reflectivity,²³³ and tunable optical diffraction gratings.²³⁴⁻²³⁷ Because they require mass transport, redox processes are ill-suited for the type of ultra-fast signal manipulation needed for optical communication and data processing. However, for applications such as image display and processing that need only be considered fast on the human time scale, a timescale of tens of ms, redox processes offer an excellent approach to exert control over a system because of their frequent robustness and reversibility.

The diffraction efficiency of optical diffraction gratings has been controlled via redox processes in the past,²³⁴⁻²³⁷ although the time scale of the optical change was on the order of hundreds of seconds²³⁵ and the periodicity was static. Other efforts have produced optical diffraction gratings with variable periodicity, but required potentials in excess of 45V.²³⁸ Redox processes with relatively fast responses have been used to modulate the imaginary part of the refractive index.¹⁹² However, modulation of the real part of the refractive index is less common, and is often accomplished via electrooptic materials that require applied fields in excess of a kV to yield a Δn of a tenth.²³⁹ In this communication we report control over the real component of the refractive index with a millisecond response time and requiring potentials less than 1.5V. We use this control to build a variable periodicity phase diffraction grating.

Individually addressable ITO interdigitated microband electrodes (IAIME's) on glass were obtained from Abtech Scientific. Electrodes were 5 μm wide and spaced 5 μm apart. Thiophene was anodically polymerized on ITO following the method of Tourillon²⁴⁰. While other groups have reported the need for significantly elevated potentials for the electropolymerization of thiophene on ITO²⁴¹, we found that a slightly elevated potential (1.9V vs. Ag/Ag^+ , pseudoreference) was required for the first oxidation wave, and that the deposition cycle proceeded satisfactorily at the more traditional 1.7V for subsequent cycles. The deposition was confirmed by AFM and optical microscopy, with the electrical quality of the film evident in

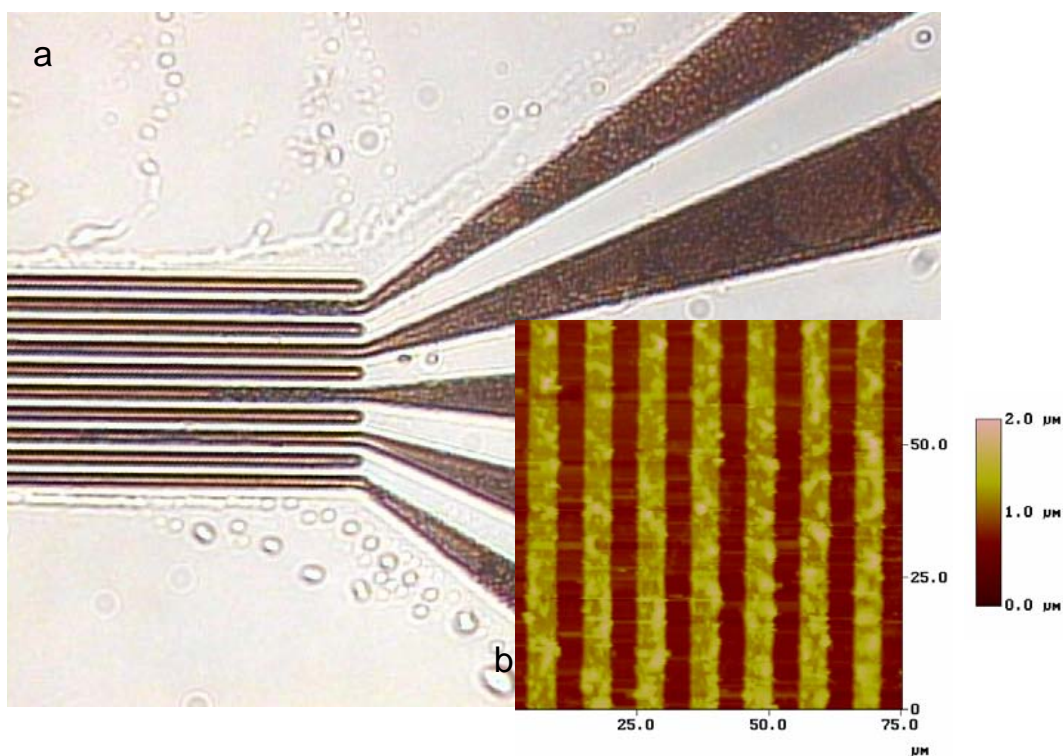


Figure 35 a) Optical microscope image of IAIME with deposited thiophene. B) AFM image of the same film.

its orange color, as seen in Figure 35. Two deposition cycles typically yielded film thickness of several hundred nanometers. An optically transparent cell was constructed around the ITO/glass plate using a glass slide and rubber (Viaton) washer, defining a cell of approximately 0.2 mL. Platinum and silver wires were inserted through the washer to serve, respectively, as the counter and reference electrodes to enable potentiostating of the redox process. The cell was filled with a 0.1M tetrabutylammonium perchlorate acetonitrile solution, with care taken to remove large air bubbles. A linearly polarized 17 mW HeNe laser was then directed through the cell, perpendicular to the ITO plate. Diffraction spots were clearly visible as a result of the periodicity of the electrodes and deposited polythiophene. This “off,” or “neutral” pattern can be seen in Figure 36a. Upon oxidation of every other electrode (or all the electrodes originating from one side of the interdigitated array), an “on,” or “oxidized” pattern was observed, where new spots are visible at the mid points between the spots in the “off” pattern, as seen in Figure 36b. The observation of diffraction spots at half the distance from the principle spot is consistent with the doubling of the period of the array. Spot intensity was quantitatively recorded by binning the signal from a commercial CCD camera, with the results shown in Figure 37. Subtraction of the “reduced pattern” from the “oxidized pattern” makes the formation of the “oxidized spots” highly conspicuous, while the concomitant loss of intensity of the “reduced spots” is also easily seen.

The doubling of the period of the diffraction grating implies that oxidation has altered the optical properties of the films, specifically the complex index of refraction. Plieth et al.²⁴² have

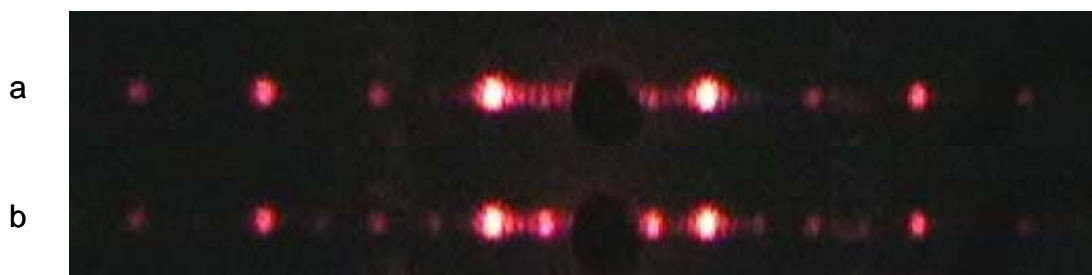


Figure 36 a) Diffraction pattern of the “off” or neutral state. b) Diffraction pattern of the “on” or oxidized state. The spot corresponding to the undiffracted beam was removed

characterized the complex refractive index of both the reduced and oxidized forms of index do change. However, Δk upon oxidation is negligible in the vicinity of the 633 nm emission from the HeNe laser. This is consistent with both electrochemical forms of polythiophene having only weak absorption in the red. An oxidatively caused opaqueness would also result in the alteration of the diffraction grating periodicity and is the mechanism of amplitude gratings.²⁴³ However, absorption of the incident light would be wasteful, and, fortuitously, is not occurring here. In contrast, Δn is nearly -0.3 upon oxidation. Such a large change in the real component of the refractive index accounts for the change in the observed interference pattern and defines the system as a phase grating.²⁴³

Step voltammetry combined with measurements of the strength of the new diffraction spots shows that the onset of the optical change coincides with the thin film oxidation and allows determination of the speed of the transformation. By examining the signal intensity of the brightest spot of the “oxidized pattern” as a function of time after the potential step, we

measure a switching time, as seen in Figure 38. In successfully fabricated devices, a potential step to 1.3 V can be repeated for over one hundred cycles without visible loss of device

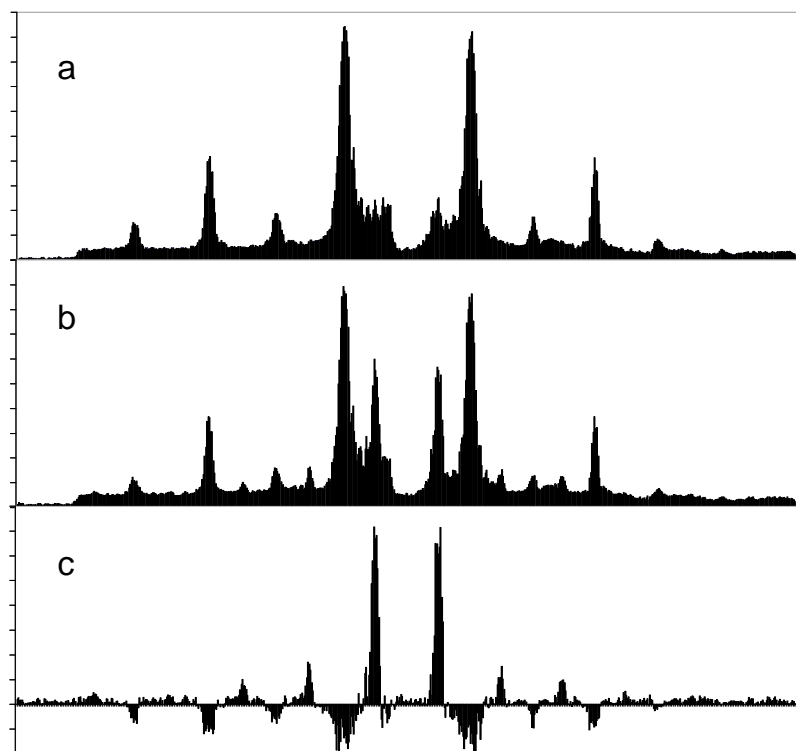


Figure 37 Binned diffraction of the a) “off” and b) “on” states along with the c) difference pattern. Negative peaks indicate loss of intensity from the original diffraction spots

functionality. Lower potentials yield slower switching speeds. Higher potentials result in faster switching speeds, but cause a loss of device functionality. The timescale of the transition, on the order of milliseconds, is noteworthy because it is significantly faster than previously reported redox active optical structures and is sufficiently fast on the human time scale to be used for the control of optical devices.

The oxidation process demonstrates first order reaction kinetics, saturating as the neutral species is consumed, and can be satisfactorily fit with an exponential with a time constant of 500 ms, as shown in Figure 38. The reduction, or un-doping process cannot be fit well by an

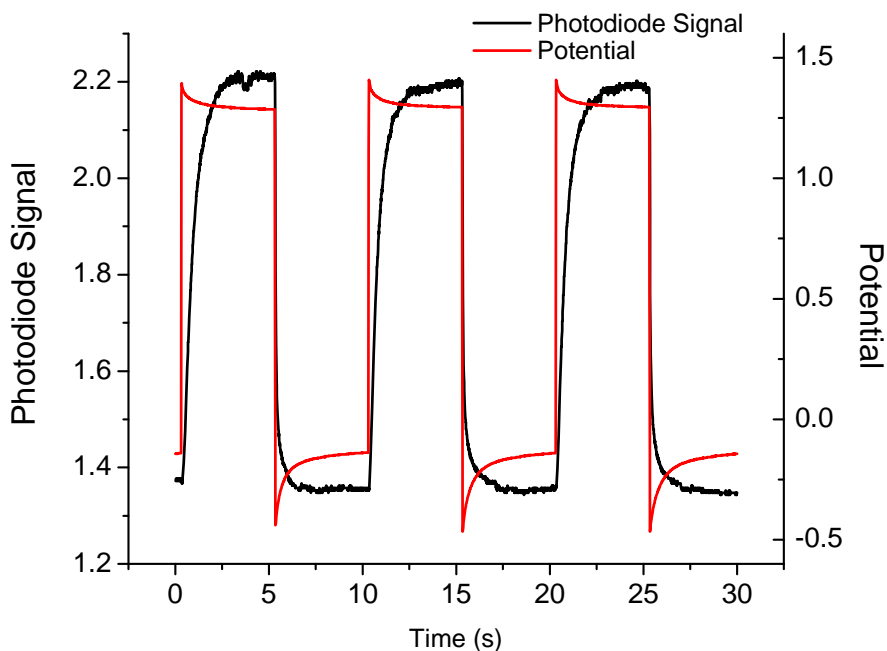


Figure 38 Time resolved response of the device determined from monitoring the (2,0) spot in the “on” pattern. Notice that the fall time is essentially limited by the response of the potentiostat

exponential, likely because the process is distorted because of the instrument response of the potentiostat. The t_{90-10} for the transition is 0.3 ms. The increased speed of the “off” transition is conspicuous in Figure 38. Hysteresis in the doping and un-doping of poly thiophene has been observed previously, and likely stems from reorganization of positive charge carriers into more delocalized species that are then more easily reduced in the cathodic wave.²⁴⁴ Ultimately, the completion of both processes is limited by mass transfer of the counter-ion through the film.

Conjugated polymers would seem to be excellent materials for redox switchable optical devices. Their typically low redox potentials, a result of their extended π systems, allow facile switching between “on” and “off” states. The large Δn upon oxidation is also a result of the extended conjugation. High quality polythiophene has a typical polaron length of 4 thiophene

subunits²⁴⁰. Consequently, oxidation will result in a significant and spatially large reduction of electron density, and thus polarizability. The real part of the refractive index, n can be related to the microscopic polarizability, α , using the Lorentz model²⁴⁵

$$n = \sqrt{1 + 4\pi N\alpha} \quad (\text{A.1})$$

where N is the number of oscillating electrons per unit volume. Therefore, as the oxidation proceeds, the size of the polaron allows a significant $\Delta\alpha$, while the relatively small size of the oxidizable area means that the polaron density, and thus N , will be quite high. The result is a large macroscopic reduction of n . The drawback of conjugated polymers is their typically large absorption in the visible region. The absorption of polythiophene at 633 nm remains essentially unchanged upon oxidation,²⁴² but the use of an optically transparent conjugated polymer, such as PEDOT, would be better suited for a device that required an optical window that covered the whole visible spectrum.

In summary we have demonstrated redox control over the real part of the refractive index and created a variable periodicity phase diffraction grating. The switching speed and robustness of the system make it an encouraging prototype system for redox switchable optical devices based on modulating the real part of the refractive index. Future work will look at alternative polymers, including PEDOT, to obtain larger optical windows and faster switching speeds, and at other applications employing the redox switchable paradigm.

Acknowledgements: Masanori Iimura, Brooks Jones

Curriculum Vitae

Randall H. Goldsmith

r-goldsmith@northwestern.edu

Current PhD candidate at **Northwestern University, Department of Chemistry and Center for Nanofabrication and Molecular Self-Assembly**,
Materials Chemistry concentration, 2007 projected graduation

Education: **B.A. Chemistry cum laude Cornell University (2002)**
B.A. Biology Cornell University (2002)

Awards:

Dan David Prize Scholarship in Materials Science (2006)
as selected by George Whitesides, Robert Langer, and C.N.R. Rao
Link Energy Foundation Graduate Fellowship (2005)
Donald E. Smith Award for Excellence in Advanced Teaching (2004)
Honorable Mention, Link Energy Foundation Graduate Fellowship (2004)
Honorable Mention, National Science Foundation Graduate Fellowship (2002)

Publications:

Goldsmith, R.H.; DeLeon, O; Finkelstein-Shapiro, D.; Rater, M.A.; Wasielewski, M.R. "Temperature Dependence of Charge Separation Through Fluorene Oligomers: An Ideal System for Studying Charge Transfer Mechanisms" **article in preparation**

Solomon, G.C.; Andrews, D.Q.; Goldsmith, R.H.; Hansen, T.; Wasielewski, M.R.; Van Duyne, R.P.; Ratner, M.A. "Quantum interference in acyclic systems: the unexpected conductance of cross-conjugated molecules" **article in preparation**

Goldsmith, R.H.; Vura-Weiss, J.A., Vega, A.M., Borkar, S., Sen, A., Ratner, M.A., Wasielewski, M.R. "Never underestimate your sigma system: Charge transfer through benzo-annulated bicyclo[2.2.2]octanes and triptycene," **article in preparation**

Goldsmith, R. H.; Iimura, M.; Jones, B. A.; Wasielewski, M. R., "Fast redox-switchable diffraction gratings" **article and invention disclosure in preparation**

Goldsmith, R. H.; Wasielewski, M. R.; Ratner, M. A., "Electron transfer in multiply bridged donor-acceptor molecules: Dephasing and quantum coherence", *J. Am. Chem. Soc.* **2007**, *129*, 3066.

Kelley, R. F.; Goldsmith, R. H.; Wasielewski, M. R., "Energy transfer within self-assembled Chlorophyll squares", *J. Am. Chem. Soc.* **2007**, *129*(20); 6384. – highlighted in *Science*

Goldsmith, R. H.; Wasielewski, M. R.; Ratner, M. A., "Electron transfer in multiply bridged donor-acceptor molecules: Dephasing and quantum coherence", *J. Phys. Chem. B* **2006**, *110*, 20258.

Weiss, E. A.; Katz, G.; Goldsmith, R. H.; Wasielewski, M. R.; Ratner, M. A.; Kosloff, R.; Nitzan, A., "Electron transfer mechanism and the locality of the system-bath interaction: A comparison of local, semilocal, and pure dephasing models", *J. Chem. Phys.* **2006**, *124*, 1.

Goldsmith, R. H.; Sinks, L. E.; Kelley, R. F.; Betzen, L. J.; Liu, W. H.; Weiss, E. A.; Ratner, M. A.; Wasielewski, M. R., "Wire-like charge transport at near constant bridge energy through fluorene oligomers", *Proc. Natl. Acad. Sci. U. S. A.* **2005**, *102*, 3540.

Neves, H. P.; Goldsmith, R. H.; Degolyer, A. W.; Shmidt, J. J.; Montemagno, C. D., "Fabrication of a Nano-Needle Array", *Proceedings of the 11th International Conference on Solid State Sensors and Actuators, Munich, Germany*, **2001**.

Posters Presented at:

ACS winter national meeting, 2007

Gordon research conference: Electronic Donor Acceptor Interactions, 2006

Workshop on molecular electronics (Prague), 2006

Gordon research conference: Electronic Donor Acceptor Interactions, 2004

Laboratory and Teaching Experience:

a. **Joint Student with Professor Mark A. Ratner and Professor Michael R. Wasielewski in the Northwestern University department of chemistry**; 8/2002 to present

Investigation of distance effects in electron transfer in Donor-Bridge-Acceptor (DBA) molecules; investigation of scaling laws for electron transfer in DBA systems with multiple spatial pathways; manipulation of real part of index of refraction in thiophene films via redox chemistry

b. Wasielewski Group Safety Officer; 9/2003 to present

c. Head Teaching Assistant for Chem 101 (general chemistry) and Teaching Assistant for Chem 342 (physical chemistry lab) at Northwestern University; 8/2002 to 6/2004

d. Undergraduate Research with **Professor D. Tyler McQuade** in the **Cornell University** department of chemistry; 8/2001-5/2002 – synthesis of conjugated oligomer liquid crystals for chemical sensors

e. Summer Intern with **Dr. Frank Houlihan** at **Bell Laboratories** in Murray Hill, NJ for Agere Systems; 6/2001-8/2001 – synthesis of polymers for planar waveguides, synthesis of metal complexes for rare earth atom signal amplification in fiber optics

f. Undergraduate Research with **Professor Carlo Montemagno** at the **Cornell Nanofabrication Facility**; 8/1999-6/2001 – photolithographic production of arrays of silicon nitride nanoneedles for drug delivery

g. Teaching Assistant for BioBM333: Principles of Biochemistry; Proteins, Metabolism, and Molecular Biology; 6/2000-8/2000

h. NASA/New York Space Grant Summer Intern with Professor Paul Goldsmith in the Cornell University Astronomy Department; 6/1999-8/1999 – analysis of data from the Submillimeter Wavelength Astronomy Satellite to generate maps of column density of molecular clouds